

Swansea University  
School of Physical Sciences

Submitted to the University of Wales in fulfilment of the requirements for the  
Degree of Doctor of Philosophy

# **Development of an Antihydrogen Trapping Apparatus.**

by

**Matthew James Jenkins**

Supervisor: Prof. M. Charlton

2008



# Abstract

This thesis details the development and commissioning of the ALPHA antihydrogen trapping apparatus. It discusses the history of antimatter physics that led to and enabled the design of the apparatus. It discusses the importance of anti-hydrogen trapping in testing one of the basic assumptions of the Standard Model of particle physics (that of CPT invariance). It goes on to discuss the design and construction of the apparatus. Finally, it presents results that demonstrate antihydrogen formation in the new magnetic field configurations that together constitute a magnetic minimum trap for neutral antihydrogen. This is an important preliminary result for any antihydrogen trapping apparatus, and confirms that the ALPHA apparatus does present a potential route towards laser spectroscopy of antihydrogen.



---

# Contents

---

<b>Contents</b>	<b>i</b>
<b>List of Figures</b>	<b>iv</b>
<b>List of Symbols and Abbreviations</b>	<b>xiii</b>
<b>1 Introduction</b>	<b>1</b>
1.1 A Brief Overview of Antimatter Physics . . . . .	1
1.2 This Thesis . . . . .	5
<b>2 Apparatus and Aims</b>	<b>7</b>
2.1 The ALPHA Collaboration . . . . .	7
2.2 CPT Invariance . . . . .	8
2.3 The AD . . . . .	9
2.4 The Positron Accumulator Apparatus . . . . .	12
2.4.1 Positron Beam Production . . . . .	12
2.4.2 Accumulation . . . . .	16
2.4.3 Transfer . . . . .	20
2.4.4 Positron Detectors . . . . .	20
2.5 The Antiproton Apparatus . . . . .	21
2.5.1 ATHENA's Antihydrogen Detector . . . . .	22
2.5.2 Antihydrogen Production Mechanisms . . . . .	25
2.5.3 Trapping Antihydrogen . . . . .	27
2.5.4 ALPHA Magnet Design . . . . .	29
2.5.5 ALPHA Trap Configuration . . . . .	35
2.5.6 Control System . . . . .	45
2.5.7 Detection and Data Acquisition . . . . .	49
2.5.8 Standard mixing . . . . .	56

<b>3 Antiparticle Catching and Transfer and Antihydrogen Formation in the 2+1 T Solenoidal Field Configuration</b>	<b>59</b>
3.1 Positrons . . . . .	59
3.2 Antiproton Catching . . . . .	60
3.2.1 Beam Steering . . . . .	60
3.2.2 HV delay . . . . .	63
3.2.3 Rotatable Degrader . . . . .	65
3.2.4 Catching Voltage and Solenoidal Field Strengths . . . . .	66
3.3 Antiproton Cooling . . . . .	67
3.4 Electron Kicking . . . . .	70
3.5 Antiproton Stacking . . . . .	72
3.6 Antiproton Transfer . . . . .	74
3.7 Antihydrogen Production at Reduced Field . . . . .	76
<b>4 Antiparticle Storage and Mixing in an Octupole Field</b>	<b>81</b>
4.1 Positron Storage . . . . .	84
4.2 Antiproton Storage . . . . .	85
4.3 Antihydrogen Formation in the Octupole Field . . . . .	86
4.4 A First Attempt to Trap Antihydrogen . . . . .	89
<b>5 Conclusions and Prospects</b>	<b>93</b>
<b>Bibliography</b>	<b>99</b>
<b>Appendices</b>	<b>107</b>
<b>A The High Voltage System</b>	<b>109</b>

---

# Acknowledgements

---

The development of the ALPHA apparatus was the work of many people. I consider myself extremely fortunate to have had the opportunity to work on such an interesting and exciting experiment, and with such an intelligent and talented group of people. I would like to thank ...

My supervisor Mike Charlton, for giving me the opportunity to work on such an interesting and exciting experiment, and especially for his patience and invaluable assistance during the completion of this thesis.

The technical coordinator of the ALPHA experiment Paul Bowe, whose tireless guidance at CERN taught me much and helped me make a meaningful contribution to the experiment.

Jeff, Lars and Niels for a great deal of assistance, not only with work, but also with dealing with the world outside the lab.

Dirk, Joel, Richard, James, Steve, Alex, Gorm, Will, Daniel, Makoto, Ryo and the rest of the ALPHA collaboration.

The EPSRC for funding my participation in the experiment.

I would also like to thank my future wife Gemma Coleman for her unceasing encouragement and support.

Finally I would like to thank my sister Victoria, my mother Hilary, and in particular my father Richard Jenkins, to whom I dedicate this thesis, for 32 years of advice, support and generally helping me get to where I am today.

---

# List of Figures

---

1.1	Photo: Carl D. Anderson [1]. Anderson's cloud chamber picture demonstrating the existence of the positron. A particle enters the picture from below and passes through a layer of lead. The curvature and length of the track above the lead can be used to determine the momentum and the sign of the charge of the particle. . . . .	3
1.2	Experiment PS210. Schematical top view of the detector apparatus (figure reproduced from [2]). Sc: Trigger and time-of-flight scintillators, Si: Silicon counters, D: Delay wire chambers, NaI: six-fold NaI-calorimeter, H: scintillating fibre hodoscope, B: magnetic dipole field. . . . .	4
2.1	The Proton Synchrotron (PS) complex pre-1997. The AA and AC have since been converted into the AD (see text for further details). . . . .	10
2.2	A typical AD cycle during the 2006 run. . . . .	11
2.3	A schematic overview of the positron apparatus (see text for details). . . . .	13
2.4	Schematic of the positron accumulator trap electrodes and potentials. The nitrogen buffer gas pressure in each stage is shown and the electrodes are numbered E1 to E7: E4 was six-way segmented for application of the rotating wall and E7 was the gate electrode. . . . .	18
2.5	The effect of the rotating wall on the number of accumulated positrons. Filled circles are data for rotating wall ON, empty circles for rotating wall OFF. These data were taken with the ATHENA apparatus, with a positron source of approximately 40 mCi (i.e. around twice that of the source in the ALPHA apparatus). Figure taken from [3]. . . . .	19
2.6	A schematic view of the ATHENA detector (figure from [4]). Reconstructed paths of annihilation products from an antihydrogen annihilation are shown. Also indicated is the opening angle, $\theta_{\gamma\gamma}$ , for photons produced during positron annihilation. . . . .	23

2.7	Reconstructed antiproton events for (a) cold mixing and (b) hot mixing (positrons are heated with RF noise before mixing in order to suppress antihydrogen formation). Figure from [4]. . . . .	24
2.8	Positron annihilation events versus opening angle. For cold mixing a peak is clearly visible at $\cos\theta_{\gamma\gamma} = -1$ . Figure from [4]. . . . .	25
2.9	Energy levels of hydrogen in the 1S state in an external magnetic field. For antihydrogen the spin labels and magnetic moments are reversed (figure from [5]). . . . . .	27
2.10	A typical Ioffe-Pritchard trap configuration. Red arrows show the direction of current in quadrupole and mirror coils. Penning trap electrodes are also shown as a visual aid. . . . .	28
2.11	Critical current, $I_c$ , at various magnetic fields for the wire used to construct the ALPHA multipole magnet. All data points were taken using wire with a copper/superconductor ratio of 0.9:1 in a seven stranded cable bundle that was manufactured by Supercon [6]. The points marked “Berkeley” and “Our design” used 0.33 mm wire, the remaining points used a very similar 0.303 mm wire. The two “Original” data sets were taken at the Brookhaven National Laboratory (where the ALPHA magnets were constructed), while the “Manufacturer” data set was taken by Supercon. These three sets were taken with short wire samples and set likely upper bounds on the performance of the wire when incorporated into a magnet. The “Berkeley” point comes from measurements of a prototype magnet at U.C.Berkeley, and is very close to the short sample performance when adjusted for the increased radius. The “Our design” point is located at ALPHA’s intended operation point. Figure from [7]. . . . .	30
2.12	Radial field dependence for $s = 2-5$ (quadrupole through decapole) normalised to unity at the electrode wall radius. The significance of the horizontal line is explained in the text. Figure from [7]. . .	31
2.13	The top picture is an axial view of a cross section in the middle of the magnet system indicating the azimuthal angles for the planes for (a), (b) and (c). These three plots show the total field for a number of different radii as a function of $z$ . The radius for subsequent solid lines differs by 1 mm: (a) -22.5°; (b) 0°; and (c) 22.5°(see text). The bottom picture shows the schematic magnet assembly. Fig from [7]. . . . .	34
2.14	Magnetic field on axis for the magnet assembly including the 1 T background field from the large-diameter external solenoid. Fig from [7]. . . . .	35

2.15 Schematic representation of the ALPHA antiproton apparatus. See text for details. . . . .	36
2.16 Magnetic field in the main ALPHA solenoid. Included are the total field (on the left axis) and the field homogenous to 1% (on the right axis). The field from the ATHENA apparatus is included for comparison. . . . .	37
2.17 Measured divergence of the magnetic axis from the mechanical axis of the main ALPHA solenoid. . . . .	38
2.18 Schematic overview of the system of electrodes used in the ALPHA apparatus in 2006. Also shown are the positions of the internal (catching) solenoid and the centres of the neutral trap mirror coils. . . . .	43
2.19 Thin electrodes used in the mixing trap region. See text for description. . . . .	44
2.20 Enlarged view of a section of a thin electrode. The red area highlights a spherical indentation which is a seat for one of the ruby balls used to separate and electrically isolate electrodes. The green area highlights one of the channels used for the wires that hold the trap together and away from the vacuum wall. The light-blue area highlights one of the channels used for the strip-lines that make the electrical connections to the electrodes. See text for details. . . . .	45
2.21 Schematic overview of the various control elements involved in running the ALPHA apparatus. See text for details. . . . .	46
2.22 The PXI system used as the ALPHA sequencer. This picture was taken during system development. Modules shown (left to right) are; RT controller, FPGA module, 2xAO module, see text for details. . . . .	47
2.23 Schematic representation of the segmented silicon beam counter. The five sectors (or pads) are shown and labelled. . . . .	50
2.24 The Faraday Cup during construction. The final degrading foil can be seen in the centre of the cylindrical section of the electrode. Ceramic pieces used to electrically isolate the electrode from the mount are also visible. . . . .	51
2.25 Schematic overview of the ALPHA data acquisition system. . . . .	53
2.26 An example of a histogram produced by the MIDAS web interface. This histogram shows 3 variables; the helium level in the transport dewar (read once every 10 minutes), and the temperature reading from two cernox sensors in the cryostat. . . . .	55
2.27 An example of the online status display generated by the ALPHA-ROOT program. Beam counter response plus several other status values can be seen. An image such as this one is generated (and updated as information arrives) for each AD antiproton ejection. . . . .	55

2.28 An example of a histogram generated during offline analysis using the ALPHAROOT program. This histogram shows the APD event rate (i.e. the rate of signals that appear in more than one APD coincidentally) from the “start of mixing” trigger to the “end of mixing” trigger. . . . .	56
2.29 Schematic depiction of antiproton transfer from one electrode to an adjacent electrode. Arrows represent increasing (or decreasing) applied voltage. . . . .	57
2.30 Schematic depiction, with commentary, of the mixing phase of a “standard mixing” sequence. . . . .	58
3.1 The AD extraction beamline into the ALPHA apparatus. Individual elements are described in the text. . . . .	61
3.2 Scan of horizontal dipole current for magnet DHZ35 during run number 931 (22/10/06). The ordinate represents the external scintillator counts during the ‘hot-dump’ integration period. Uncertainties are comprised of counting statistics only (one standard deviation). . . . .	63
3.3 Optimisation of the delay in applying HV for antiproton trapping. Uncertainties are comprised of counting statistics (one standard deviation). . . . .	64
3.4 Degrading curve (see text for details). Uncertainties in the ordinate represent counting statistics only (one standard deviation). Uncertainties in the abscissa derive from the mechanical error in the rotation setting ( $\pm 2.5^\circ$ ) and thus are at a minimum when the foil is orthogonal to the beam (i.e. at its minimum thickness, in this case $18 \mu\text{m}$ ). The data point at 0 thickness was acquired with the degrader foil completely removed from the beam path. . . . .	65
3.5 Effect of varying applied high voltage on the number of caught antiprotons. . . . .	66
3.6 Effect of varying applied solenoidal field on the number of caught antiprotons. . . . .	67
3.7 Schematic overview, with commentary, of a typical catch, cool and dump sequence. . . . .	69
3.8 Cooling curve (values taken from runs 1111-1119). Hot and Cold dumps are shown, as well as their total (Hot+Cold). Uncertainties represent counting statistics (one standard deviation). The exponential fit of the hot dump data has a time constant of 14.7 ( $\pm 0.7$ ) seconds. . . . .	70
3.9 Effect of antiproton stacking on the number of antiprotons available for mixing. . . . .	73



3.14 Annihilation events, as measured by the APDs, as a function of time after the start of mixing, for standard mixing (black) and hot-mixing (red). The time bins are 1 s long. The data are for 10 mixing cycles, normalized to one cycle. The inset is a plot of the first 5 s of the same data, re-binned into 200 ms bins to illustrate the rise time of the antihydrogen production. The uncertainties reflect counting statistics only (1 standard deviation). Figure from [9]. . . . .	80
4.1 Net magnetic field from the octupole and main solenoid. The vectors on the left represent the directions of the axially invariant field from these coils. The surface is created by following the field lines from a radially centred circular locus; the lines shown within the surface are field lines. . . . .	82
4.2 The normalised critical radius as a function of the octupole strength $B_w$ and orbit length $L$ . The alternate axes shown at the top isolate the dependance on each parameter while holding the other fixed at a typical value. Figure from [10]. . . . .	83
4.3 The ratio of the number of positrons stored in the octupole field to the number stored without the field is plotted versus holding time. Values were measured with the Faraday Cup and two CsI detectors. Error bars (typically $\pm 10\%$ ) are omitted for clarity. Figure from [11]. . . . .	85
4.4 The ratio of the number of antiprotons stored in the octupole field to the number stored without the field is plotted versus holding time. Error bars are standard deviations for one set of measurements. Figure from [11]. . . . .	86
4.5 Antiproton survival during mixing in the octupole field. The ordinate represents the sum of the left and right dumps after mixing, normalised to the signal from HPD2, the abscissa represents the current in the octupole during mixing. The different data points in each series represent data collected during different runs, the variation seen is a symptom of unstable electron loading conditions. . . . .	87
4.6 Positron cooling of antiprotons in the presence of the octupole field. Histograms show left and right well dumps for mixing cycles with positrons (run 2255 - black line) and without (run 2271 - red line). Plots show external scintillator (PMT) response over time (in seconds) during the dump integration window. The octupole was operating at a current of 700 A in each case. See text for details. . . . .	88

4.7 Mixing in the presence of the octupole field. The first 12 s of mixing for two different measurement cycles are shown, one with positrons (run 2255 - black line) and one without (run 2271 - red line). Plots show internal scintillator (APD) response over time (in seconds), beginning at the start of mixing. The octupole was operating at a current of 700 A in each case. The inset plot shows the first 0.04 s of the run 2271 data, it illustrates the large loss contained within the first time bin of the main plot (run 2255 has a similar though slightly reduced loss). . . . . 89

4.8 Evidence for antihydrogen formation in the presence of the octupole field. Antiproton annihilation event rate is plotted over time (in seconds) during mixing as measured by the internal scintillators (APDs). The black line represents the normalised sum of 5 cold mixing results over 4 runs, the red line represents the normalised sum of 5 hot mixing results over 4 runs. The large peak at around 27 seconds is the result of the high energy collision of protons with the iridium target at AD injection. The shower of particles created in this collision causes a response in every scintillator in the AD hall. In later years a system was implemented to remove this feature from acquired data by inhibiting the injection phase of the AD cycle. 90

5.1 Schematic representation of the MCP and phosphor screen. Particles entering the MCP on the left produce a shower of electrons (shown in red) which exit the right of the MCP and are accelerated towards the phosphor screen. . . . . 94

5.2 Two typical images acquired with the MCP/phosphor screen assembly. These images were generated by passing a circular electron plasma through the octupole, with the octupole off and on. Apertures (discussed in the text) form the image boundaries and limit the image to one quadrant of the octupole field map. The distortion evident in the right-hand image corresponds to one flute of the magnetic surface shown in figure 4.1. . . . . 95

5.3 Schematic diagram of the ALPHA apparatus that shows the position of the MCP/phosphor assembly, and also the positions of the apertures apparent in the generated images (see text for details). The graph below the schematic plots the axial magnetic field. Figure from [12]. . . . . 96

5.4 Antiproton and electron images showing the effects of the rotating wall, and the resulting radial profiles. Figure from [12]. . . . . 97

A.1 Oscilloscope traces illustrating the charging characteristics during the fast high voltage switching. Figures A: and B: are taken from the same data acquisition cycle and show the initial fast voltage drop (5.12 kV in 124 ns). Figure C: is taken from a different data acquisition cycle (before several stages of optimisation), but illustrates the voltage transients typical during the approximately 50 ms after the initial drop (discussed in the text). . . . .	111
A.2 Oscilloscope trace showing the discharging of HVB. This trace was taken during the 2007 beam time, but using an identical system to that used in 2006. . . . .	111
A.3 Schematic representation of the control and timing system for the fast high voltage switching. See text for details. . . . .	113



---

# List of Symbols and Abbreviations

---

Abbreviation	Description	Definition
pbar ( $\bar{p}$ )	Antiproton	2
LEAR	Low Energy Antiproton Ring	3
CERN	European Organisation for Nuclear Research	3
CPT	Charge, Parity and Time reversal	5
AD	Antiproton Decelerator	5
PS	Proton Synchrotron	10
UHV	Ultra High Vacuum	39
G10	A high strength glass-epoxy laminate with low thermal conduction	33
OVC	Outer Vacuum Chamber	39
VCL	Vapour-Cooled Lead	39
HV	High Voltage	42
Kapton	A polyimide film suitable for use in high vacuum and low temperature environments	44
PXI	PCI eXtensions for Instrumentation	45
FPGA	Field Programmable Gate Array	47
DAQ	Data Acquisition (system)	49
HPD	Hybrid Photodiode	50
PMT	Photo-Multiplier Tube	51
APD	Avalanche Photodiode	52
VME	Versa Module Eurocard bus	53
ADC	Analogue to Digital Converter	53
MIDAS	Maximum Integration Data Acquisition System	54
MCP	Microchannel Plate	94
NIM	Nuclear Instrumentation Module	112

---



# Chapter 1

---

## Introduction

---

### 1.1 A Brief Overview of Antimatter Physics

In 1900, in order to derive a formula for the observed frequency dependence of the energy emitted by a black body, Max Planck proposed that electromagnetic energy could only be released in discrete quantised packets. This was followed in 1905 when Albert Einstein explained the photoelectric effect (electrons emitted from a material after absorption of electromagnetic energy e.g. x-rays or visible light) by suggesting that electromagnetic radiation consists of a finite number of energy quanta that are localised at points in space [13]. In 1913 Niels Bohr used quantisation to describe the spectral lines of the hydrogen atom. By the mid-1920's Erwin Schrödinger and Werner Heisenberg had developed these ideas into the new field of Quantum Mechanics and Schrödinger had provided a wave equation solution to describe the hydrogen atom.

1905 was also the year that Albert Einstein presented the world with his theory of Special Relativity [14]. With it he explained the relationship between space and time, and matter and energy. The new Quantum Theory however was not relativistic, since it was formulated in Euclidean space using Cartesian tensors (i.e it was invariant under Galilean transformations). In 1928 Paul Dirac proposed an equation which gave a relativistic solution to the wavefunction for an electron (it was invariant under the Lorentz group of transformations) [15, 16]. The equation had four solutions, predicting the spin up and down states of the electron and also spin up and down states for an electron with negative energy, or anti-electron. Dirac proposed that the vacuum is filled with a “sea” of negative-energy electrons, the Dirac sea. Any real electrons would therefore have to sit on top of the sea, having positive energy. A “hole” in the sea would have a positive charge and energy. At first

he thought that this was the proton and calculated an annihilation cross section for the electron and proton [17]. This didn't fit the theory well. Hermann Weyl pointed out that the hole should have the same mass as the electron, and Oppenheimer demonstrated that Dirac's proposed electron/proton annihilation cross section would lead to "a mean life time for ordinary matter of the order of  $10^{-10}$  seconds." [18]. Dirac later suggested that both electrons and protons had an antiparticle which was identical to the particle but with opposite charge. The currently accepted group of theories known as the Standard Model (a quantum field theory which describes three of the four known fundamental interactions of elementary particles) now suggests that every particle has an antiparticle in which the sign of every additive quantum number is reversed (for example charge and magnetic moment but not mass). For particles whose additive quantum numbers are all zero the particle may be its own antiparticle, for example the photon.

In 1932 Carl Anderson was investigating cosmic rays in a cloud chamber in Millikan's lab in CalTech. Cosmic rays (discovered by Victor Hess in 1912 for which he received a Nobel prize in Physics in 1936) are high energy particles which enter the Earth's atmosphere from above. They can collide with molecules in the atmosphere (such as oxygen or nitrogen) and produce showers of lighter particles. A cloud chamber contains a supersaturated water or alcohol vapour. When an energetic particle passes through the cloud chamber it ionises the vapour along its path and precipitates condensation, so the path of the particle is traced by the mist that forms behind it. If a magnetic field is applied then positively and negatively charged particles will curve in opposite directions. Anderson found unexpected tracks which he correctly interpreted as coming from a particle with the same mass as an electron but with opposite charge (see figure 1.1). He called this particle a positron ( $e^+$ ) and deduced that it was the anti-electron predicted by Dirac [1]. For this discovery Anderson shared the 1936 Nobel prize in Physics.

The next antiparticle to be discovered was the antiproton (sometimes referred to as  $\bar{p}$  or  $p\bar{p}$ ) some 23 years later. Creation of antiparticles via pair production requires an energy equal to the sum of the rest masses of the two particles. Or for electron/positron production an energy of  $2 \times (511 \text{ keV}) = 1.02 \text{ MeV}$ . For proton/antiproton production the energy required is  $2 \times (938 \text{ MeV}) = 1.876 \text{ GeV}$ . A photon with this energy could spontaneously trigger pair production. In the case of a high energy particle collision a great deal of energy is carried away by the products of the collision so the antiproton production energy threshold is much higher (a little over 5 GeV). Cosmic rays this energetic are extremely rare. A machine named the Bevatron (**b**illions of **e**lectron **v**olts **s**ynchro**t**ron) was built at Lawrence Berkeley Laboratory in order to search for the antiproton. It began operation in 1954 and was

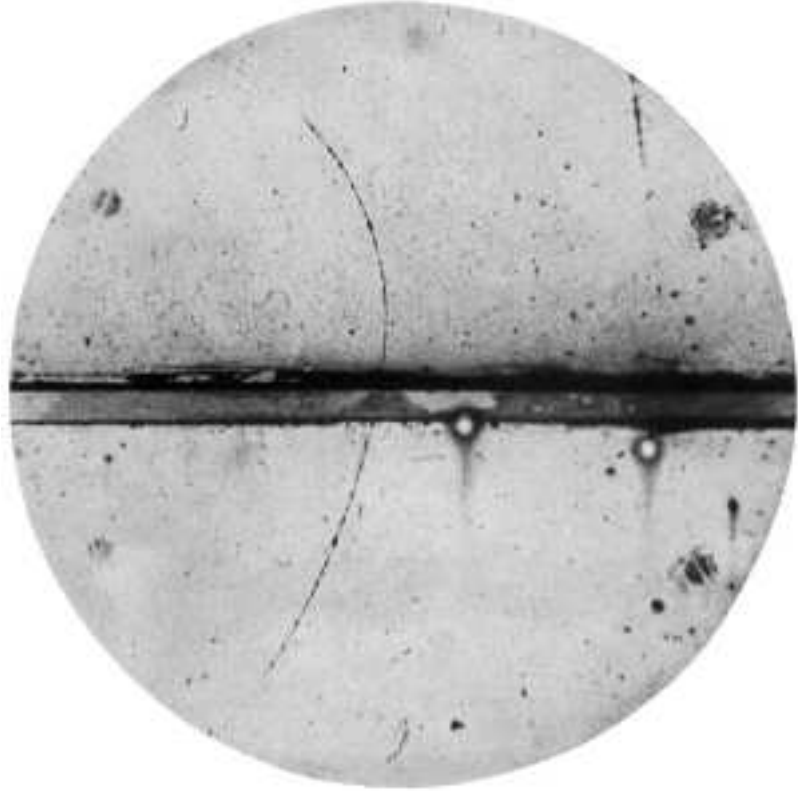


Figure 1.1: Photo: Carl D. Anderson [1]. Anderson’s cloud chamber picture demonstrating the existence of the positron. A particle enters the picture from below and passes through a layer of lead. The curvature and length of the track above the lead can be used to determine the momentum and the sign of the charge of the particle.

capable of accelerating protons to an energy of 6.2 GeV. In 1955 a team led by Emilio Segré and Owen Chamberlain, working at the Bevatron, discovered the antiproton [19], for which they won the Nobel prize in Physics in 1959. A year later a team led by Bruce Cork discovered the antineutron [20].

The discovery of other antiparticles followed. The next big challenge became the production of an antiatom, the simplest being antihydrogen, a bound state of an antiproton and a positron. In 1995 the PS210 group, working at the Low Energy Antiproton Ring (LEAR) at the European Centre for Nuclear Research (CERN), was the first to produce atoms of antihydrogen [2]. A beam of high energy antiprotons was passed through a jet of xenon gas. When a high energy antiproton passes near a xenon nucleus there is a chance it can convert some of its own energy into the production of an electron and a positron. There is an even smaller chance that the positron will be created with a velocity similar to the antiproton and the two will join to create an

antihydrogen atom. The neutral antihydrogen atom would no longer be confined and would leave the storage ring and pass into the detector apparatus (figure 1.2).

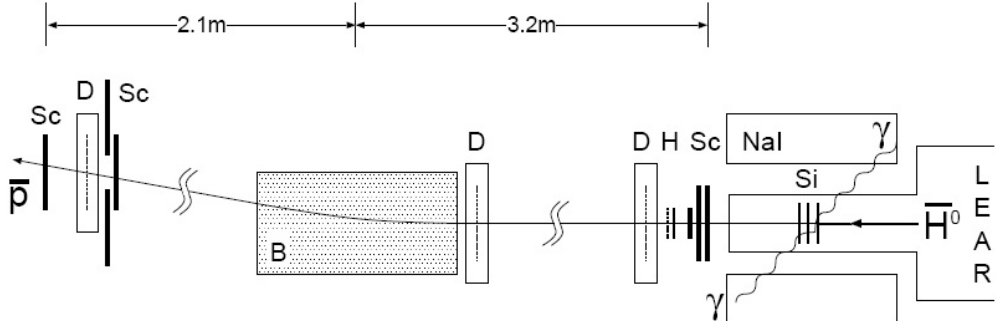


Figure 1.2: Experiment PS210. Schematic top view of the detector apparatus (figure reproduced from [2]). Sc: Trigger and time-of-flight scintillators, Si: Silicon counters, D: Delay wire chambers, NaI: six-fold NaI-calorimeter, H: scintillating fibre hodoscope, B: magnetic dipole field.

The  $e^+$  were stripped from the  $\bar{p}$  in the first silicon counter, and would annihilate in the second. The two counters were used to measure the kinetic energy of the  $e^+$  and the energy loss of the  $\bar{p}$ . The third silicon counter would further measure energy loss of the  $\bar{p}$ . Photons produced in the annihilation of the positron would be detected in the segmented NaI detector. The other scintillators would measure the velocity of the charged particle passing through the apparatus and the delay line wire chambers would measure its deflection. If all detectors produced results consistent with a coincident positron and antiproton then an antihydrogen atom had been observed. Typically  $1.7 \times 10^{10}$   $\bar{p}$  would be loaded into LEAR. They would have a lifetime during the experiment of around 3 minutes and LEAR would be re-filled around every 12 minutes. With this set-up 9 antihydrogen atoms were observed over the course of 3 weeks.

In 1997 the E862 experiment at the Fermilab antiproton accumulator used a similar method [21] and observed 99 antihydrogen atoms over a period of several months. They used a hydrogen gas jet target, the antihydrogen produced was ionised in a thin carbon foil and the moving constituents were steered into separate detector systems.

While these methods demonstrated the existence of antihydrogen, they were not well suited to further antimatter experimentation. In both cases the probability of an antiproton creating an antihydrogen atom was very low so only very small quantities were produced. Also the antihydrogen atoms were produced at a very high energy making it extremely difficult to manipulate

them for further study.

Antihydrogen with low kinetic energy (cold antihydrogen) is very attractive for experimental analysis. Hydrogen is the simplest and most abundant element in the cosmos and a great deal is understood about its structure and behaviour. This means that comparisons between the properties of hydrogen and antihydrogen could potentially be made to a very high precision. This gives the possibility of making the highest precision direct test of CPT-symmetry to date (see section 2.2 for a discussion of CPT theory).

LEAR completed its experimental programme in 1996 and was closed. However, during its operation new techniques for cooling and storing antiprotons were developed (discussed in section 2.3), and there was still a lot of interest in experimenting with antiprotons. A new facility called the Antiproton Decelerator (AD) was created at CERN in order to support experiments with ultra-low energy antiprotons and cold antihydrogen. The AD began delivering antiprotons to experiments in 2000.

Two experiments at the AD (ATHENA and ATRAP) attempted to produce large numbers of cold antihydrogen. In both cases antiprotons from the AD were caught in a trap consisting of combined electric and magnetic fields (known as a Penning trap). The antiprotons were decelerated further through collisions with a trapped electron plasma and then mixed with positrons to form cold antihydrogen. In 2002 the ATHENA collaboration announced the production and detection of 50000 cold antihydrogen atoms [4]. Shortly afterwards ATRAP published similar results [22, 23]. ATHENA finished taking data in 2004 but several of the institutions involved (including Swansea University) formed a new collaboration (ALPHA) that continues to work towards trapping and spectroscopy of antihydrogen at the AD. ATRAP also continues to work at the AD.

## 1.2 This Thesis

This thesis is an account of the design of the new ALPHA apparatus and its commissioning during the 2006 antiproton beam time. It discusses the results achieved so far which demonstrate that the new techniques required for antihydrogen trapping can be successfully implemented. Chapter 2 deals with the apparatus with emphasis on the new magnet configuration necessary in order to attempt to trap antihydrogen. Chapter 3 demonstrates antihydrogen production in the new solenoidal magnetic field configuration. Chapter 4 discusses the first results obtained during antiparticle manipulations in the magnetic fields of the neutral trap, it includes an account of an initial antihydrogen trapping attempt.

My involvement in the work presented in this thesis is diverse. I arrived at CERN in the last couple of weeks of operation of the ATHENA collaboration. I assisted in the last data collection of that apparatus and was then involved in its decommissioning and the recovery and reconditioning of many of its parts (including vacuum equipment, electrical cables and a variety of electronic instruments). This process gave me a good understanding of the wide range of systems involved in running a complicated experiment such as ATHENA and enabled me to contribute effectively to the design and construction of the ALPHA apparatus from the outset. I was involved with all areas of the new apparatus including cryogenic systems, vacuum systems, electrical systems (both power supply and data/control signals) and also installation of the radioactive source in the positron apparatus (described in section 2.4).

I was heavily involved in the design of the inner “catching” solenoid and the precise positioning of the various magnets in the ALPHA apparatus (described in section 2.5.4). I created a simulation to investigate the solenoidal fields associated with these magnets (the main solenoid, inner solenoid and 2 mirror coils) whereby the relative positions (as well as other parameters such as inner solenoid length, current density and number of turns of conductor) could be varied quickly and easily. I then used this tool to demonstrate the effect of varying these parameters and finalise the design of the inner solenoid and mirror coils. I also designed and built the high voltage system for the antiproton catching electrodes (described in section 2.5.5 and appendix A).

Once the apparatus was operational I took part in all of the data collection and experimental sequence design tasks associated with running the experiment. I also assisted with analysis both online (e.g. making plots as a parameter such as degrader angle was varied so that the optimum position could be found - as in section 3.2.3) and offline (e.g. analysing detector data after a run was completed), and in several cases collected and performed preliminary analysis of data for figures in published ALPHA papers. During operation small malfunctions were common (especially early in the life of the system), so my intimate knowledge of the entire apparatus (due to my early involvement) was invaluable at this time in making quick and efficient diagnosis and repair of minor faults. In 2007 I was also given the responsibility of “run coordinator” and was (jointly) responsible for the day to day operation and experimental direction of the apparatus during those shifts. I also helped tutor new PhD students in the operation of the apparatus.

Discussion of physics results and experimental direction was a continual process at CERN. All collaboration members participated and frequent discourse at CERN, as well as weekly online meetings, ensured rapid dissemination and testing of ideas and theories. I was an active part of this process, both at the discussion stage and in implementing new experimental sequences.

## Chapter 2

---

# Apparatus and Aims

---

### 2.1 The ALPHA Collaboration

In 2002 the ATHENA collaboration\* was the first team to produce large numbers of cold antihydrogen [4]. They went on to introduce lasers into their apparatus in order to study laser-induced recombination of antihydrogen [24], as well as further studying antihydrogen production mechanisms [25, 8, 26] and temperature dependence [27]. ATHENA completed its experimental work in 2004.

The ALPHA collaboration was formed in 2005. Several of the institutions from ATHENA (Århus, RIKEN, Rio, Swansea and Tokyo) were joined by several new institutions (Auburn University (USA), University of Berkeley (USA), University of Calgary (Canada), University of Liverpool (UK), University of Manitoba (Canada) and TRIUMF (Canada)). The new collaboration took much of the apparatus and expertise from the ATHENA experiment and aimed to continue the work of ATHENA by introducing a magnetic minimum trap to confine the neutral antihydrogen, and then, later, lasers for spectroscopic comparison of hydrogen and antihydrogen. The ultimate aim of the collaboration is a direct test of CPT invariance through comparison of the line-spectra of hydrogen and antihydrogen.

---

\*University of Århus, Denmark, University of Brescia, Italy, CERN, Switzerland, University of Genoa, Italy, University of Pavia, Italy, RIKEN, Japan, Federal University of Rio de Janeiro, Brazil, University of Wales Swansea, UK, University of Tokyo, Japan, University of Zurich, Switzerland, INFN, Italy.

## 2.2 CPT Invariance

The Standard Model for particle physics suggests that the laws of physics remain invariant under certain transformations. CPT invariance is a theorem (based in local quantum field theory) that says that the combined operations of charge conjugation (C) where every particle is replaced with its antiparticle, parity reversal (P) where every spatial coordinate has its sign reversed, and time reversal (T) where the flow of time is reversed, leave the laws of physics unchanged. In other words the evolution of a process is identical under those conditions. One of the consequences of this is that matter and antimatter should have the same mass, lifetime etc. but with opposite internal quantum numbers (and hence opposite charge, magnetic moment). Any violation of CPT invariance would have profound implications for the Standard Model and many other currently accepted physical theories.

Violations of C, P, CP and T symmetries have all been demonstrated. C-symmetry is violated by the chirality (or handedness) of neutrinos and antineutrinos. In 1956, T.D. Lee and C.N. Yang suggested that non-conservation of parity could account for the observed difference in the decay modes of the so called tau and theta mesons (which otherwise appeared identical). They suggested several possible experiments to test this hypothesis [28]. In 1957 a team led by Chien-Shiung Wu successfully completed one of these experiments. They observed a large asymmetry in the angular distribution of beta decay from a Cobalt-60 source, thus demonstrating that P-symmetry is violated by weak nuclear interactions [29]. In 1964 James Cronin, Val Fitch and their team studied the decay of the  $K_2^0$  meson in helium gas and found a pronounced forward peak in the angular distribution of the decayed  $K^0$  mass. They concluded that this was due to a 2 pion decay mode which implied a violation of CP symmetry [30]. If CPT invariance holds then any violation of CP symmetry implies a corresponding violation of T symmetry so this result can also be taken as a demonstration of T symmetry violation. They received the Nobel prize in Physics for this discovery in 1980. Most theories that attempt to explain the difference in the amount of matter and antimatter observed in the Universe rely on CP violation.

Experiments have been devised to test CPT symmetry. In 1999 G. Gabrielse et al. performed the highest precision direct test of CPT [31]. They deduced the charge to mass ratio of the proton and antiproton by observing the cyclotron frequencies of a  $\bar{p}$  and an  $H^-$  ion in a Penning trap. Using a  $H^-$  ion allowed the group to simultaneously trap a single particle of each species using the same potentials. The cyclotron frequency of the two species differed by around  $10^5$  Hz, so the particles could be selectively excited by applying an oscillating voltage of the correct frequency to a sectored electrode. This

would drive one of the particles to a large radius so measurements could be made of the other without interference. The particles could be swapped by allowing the previously excited particle to cool and exciting the other. This method removed a considerable systematic uncertainty as, in order to use a proton, the trap would need to be emptied, have its potentials reversed, and then be reloaded between each measurement. It allowed them to achieve a test of CPT to an accuracy of  $10^{-11}$ . In 1990 R. Carosi and co-workers made an indirect test of CPT invariance by observing the  $K^0$  meson decay system and estimated an upper limit for CPT violation in the mass, claiming an accuracy of  $10^{-18}$  [32].

As mentioned previously, the ALPHA collaboration aims to make a direct test of the CPT theorem through comparisons of the line-spectra of hydrogen and antihydrogen. The frequency of the 1S-2S transition in hydrogen has been measured with an accuracy of around  $10^{-14}$  [33]. The process involves the simultaneous absorption of two counter-propagating photons, thus cancelling out the 1st order Doppler shift caused by the motion of the atom. The 1S-2S transition has also been studied using magnetically trapped hydrogen [34], although so far only to an accuracy of around  $10^{-12}$ . It is reasonable to assume that similar accuracy could be achieved with spectroscopy of antihydrogen, thus providing a direct test of CPT of equivalent precision.

It should be noted that it has been pointed out that certain types of CPT violations would only show up very weakly in the 1S-2S transition [35]. Another transition that could be studied is that due to hyperfine splitting of the ground state. It has been found to be sensitive to CPT violating effects and measured for hydrogen to an accuracy of around  $10^{-12}$  [36]. The ASACUSA group (also at CERN) are currently considering experiments in this direction [37].

## 2.3 The AD

Until the end of 1996 four different machines (illustrated in figure 2.1) were used to collect, cool and decelerate antiprotons for experimental use in a variety of particle, nuclear and atomic physics experiments. The latter included new techniques such as radio frequency quadrupole (RFQ) deceleration of antiprotons [38], antiproton cooling through impact on thin ‘degrading’ foils (developed by the PS200T collaboration and discussed in section 2.5.5), and antiproton cooling on electrons and trapping as developed by the TRAP [39, 40] and PS200T [41, 42] collaborations. The antiprotons were produced by the collision of 26 GeV/c protons on an iridium production target in the Antiproton Collector (AC). They were collected and pre-cooled at 3.5 GeV/c and then transferred to the Antiproton Accumulator (AA) for accumulation and further

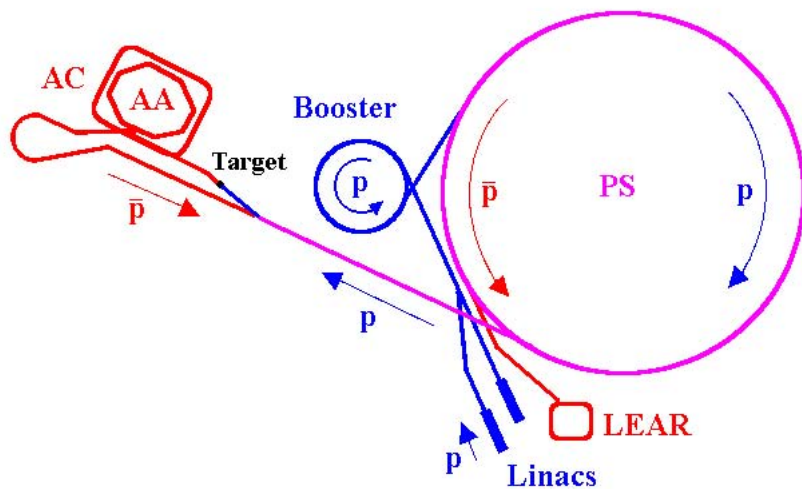


Figure 2.1: The Proton Synchrotron (PS) complex pre-1997. The AA and AC have since been converted into the AD (see text for further details).

cooling. A bunch would be sent from the AA to the Proton Synchrotron (PS) where it would be decelerated from 3.5 to 0.6 GeV/c. It would then be extracted to LEAR where alternating cooling and deceleration would reduce the beam energy further. Antiprotons would then be extracted to the experiments at around 100 MeV/c, or a kinetic energy of  $\sim 5.3$  MeV.

In 1997 the AC was converted into the Antiproton Decelerator. This one machine can perform all the functions of the four machines previously used, albeit with a much reduced duty factor. Indeed the purpose of the AD was to support the ultra-low energy  $\bar{p}$  and antihydrogen projects only, which had previously been a minor part of the LEAR programme. The AA has been decommissioned and LEAR has been converted into the Low Energy Ion Ring (LEIR) to accumulate ions for injection into the Large Hadron Collider (LHC) when it begins operation in 2008. The PS, of course, still supplies high energy protons to the AD as well as other experiments at CERN.

The AD cycle from injection (when the protons hit the target) to ejection (where antiprotons are extracted to an experiment) takes around 80 seconds. Approximately  $3 \times 10^7$  antiprotons are delivered to experiments with a kinetic energy of 5.3 MeV in a bunch of length around 200 ns.

The cycle (illustrated in figure 2.2) involves several alternating stages of cooling and deceleration. The antiprotons created at injection have a large spread in energy and position. Bunch rotation (via an applied rotating RF potential) reduces the momentum spread of the incoming particles. A technique called stochastic cooling is then used to reduce the emittance (a function of the size and momentum spread) of the beam. Stochastic cooling was in-

vented in the 1970's by Simon van der Meer at CERN (for which he received a Nobel prize in 1984). The particle bunch passes a pickup at one side of the decelerator ring and the signal generated is passed, via a shorter route than the particles traverse, to RF generators at the other side of the ring. There a corrective "kick" is applied which tends to force particles towards the average momentum of the bunch, thereby reducing the momentum spread. During the deceleration phases the beam emittance increases (known as adiabatic blow up) so additional cooling stages are required. After the second deceleration phase (when the particle bunch has a momentum of around 300 MeV/c) stochastic cooling is no longer effective, so a different cooling technique known as electron cooling is used. The bunch passes through a cold, dense beam of electrons where Coulomb interactions transfer energy from the antiprotons to the electrons. A third deceleration phase reduces the momentum of the bunch to 100 MeV/c before a final cooling phase and ejection to an experiment.

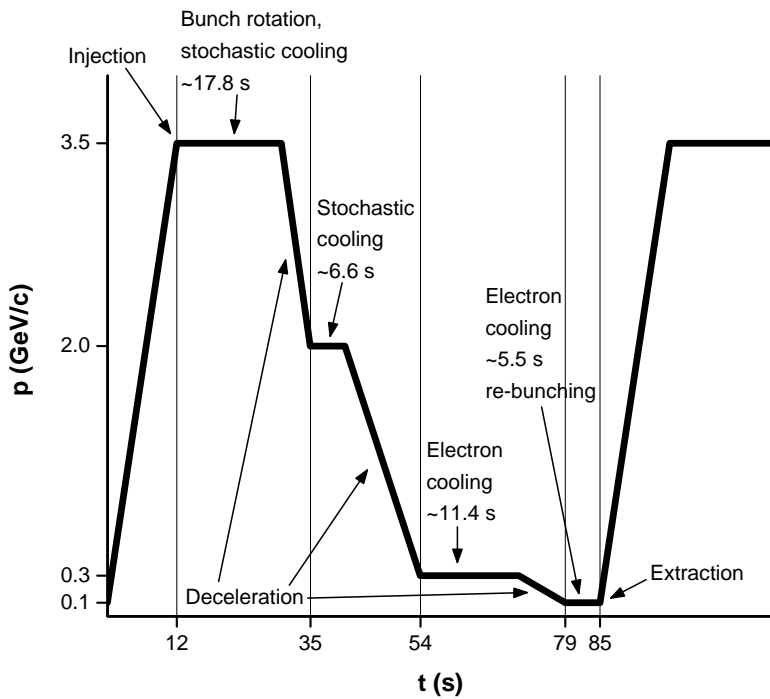


Figure 2.2: A typical AD cycle during the 2006 run.

During the 2006 beam time 4 experiments received  $\bar{p}$  from the AD:

#### AD2 - ATRAP

Antihydrogen TRAP experiment. Developed from the TRAP collaboration that pioneered many techniques used currently in the study of antiprotons.

They use similar methods of antihydrogen production to ALPHA and also aim to perform precision spectroscopic measurements.

#### AD3 - ASACUSA

Atomic Spectroscopy And Collisions Using Slow Antiprotons. This collaboration uses antiprotons to form exotic ‘atomcules’ where an electron in a helium atom is replaced by an antiproton to form antiprotonic helium. They then use lasers to probe the hyperfine structure of these atomcules and also investigate their interaction with other matter to reveal properties of antiprotons to a high precision (for example determining antiproton mass [43], most recently to a precision of  $10^{-9}$  [44]).

#### AD4 - ACE

The smallest of the experiments at the AD using the least beamtime and without a permanent experimental area in the AD hall. Current particle beam therapy commonly uses protons to destroy tumour cells inside a patient. The ACE experiment directly compares the effectiveness of cell irradiation using protons and antiprotons.

#### AD5 - ALPHA

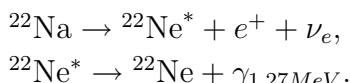
The ALPHA experiment is where the work described in this thesis took place. Its aims and methods are the focus of the rest of this thesis.

## 2.4 The Positron Accumulator Apparatus

The apparatus used to provide positrons for the ALPHA experiment (shown in figure 2.3) is the same one that was used by the ATHENA collaboration. It is based on a design developed by the Surko group at the University of California, San Diego [45, 46]. Positron beam production, accumulation and transfer into the antihydrogen apparatus will be discussed below.

### 2.4.1 Positron Beam Production

The positrons are produced in the  $\beta^+$  decay of  $^{22}\text{Na}$  into  $^{22}\text{Ne}$  via the following mechanism:



A  $^{22}\text{Na}$  source (with an activity of 700 MBq in August of 2006) was sealed in a capsule with a 5 micron thick titanium foil window on one side, through which positrons were emitted. The positrons were emitted from the source with a kinetic energy of between 0 and 0.54 MeV and an average energy of just under 0.2 MeV.

The source capsule was held on an elkonite (a tungsten-copper alloy) holder mounted at the end of a 5 K cold head. The holder was split into two pieces

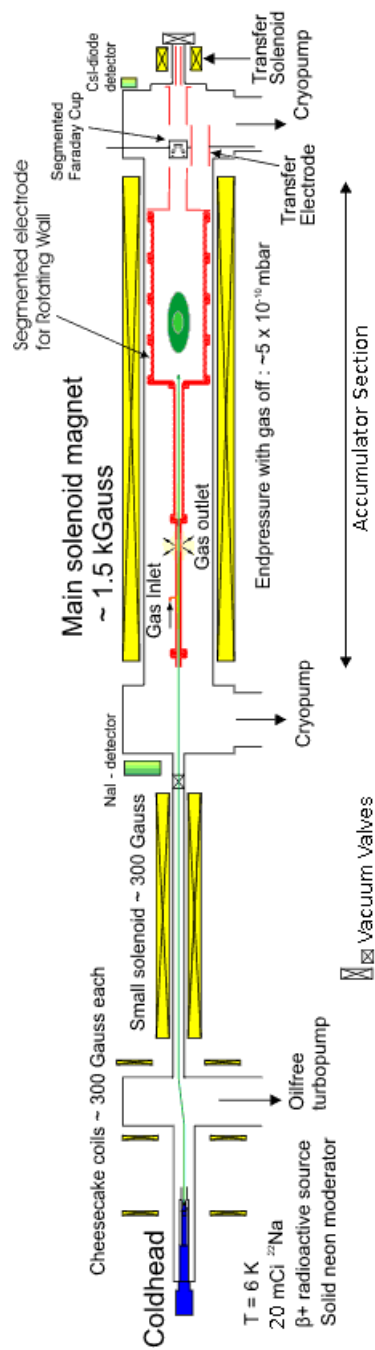


Figure 2.3: A schematic overview of the positron apparatus (see text for details).

separated by a sapphire disk so that the source section was electrically (but not thermally) isolated from the rest of the cold head. This allowed the source to be biased. A copper cone was attached to the front end of the holder in order to improve the beam intensity [47]. The cold head was cooled by closed cycle helium compression to a temperature of 5 K. This was to allow a solid neon layer (known as a moderator) to be deposited over the source window.

The purpose of the moderator is to utilise the fact that a small fraction of the positrons incident on a material may reach thermal, or near thermal, energies and be re-emitted into vacuum with reduced kinetic energy. In the case of a metal, a small electric dipole is produced at the surface due to 'leakage' of the electronic charge distribution into the vacuum. This dipole is equal and opposite for electrons and positrons and, together with the bulk chemical potential of the material, results in a positive work function<sup>†</sup> for electrons and, if the dipole is large enough, a negative one for positrons. If the work function is negative then positrons which returned to the surface would be spontaneously ejected from it. In the case of an insulator where the work function for a positron is positive, if the band gap of the solid is large (e.g.  $\sim 21$  eV for solid neon) then the slowing down of the positron to thermal energies is inefficient. This leads to a longer mean free path for the positron inside the solid so it may reach the surface with sufficient residual kinetic energy to be emitted.

These effects can be exploited to produce a low energy positron beam with a small energy spread. The technique was suggested by Madansky and Rasetti [48] in 1950, and was first achieved by Cherry [49] in 1958 using a chromium coated substrate which produced positrons with energies less than 10 eV at an efficiency<sup>‡</sup> of  $\sim 10^{-8}$ . Other advances followed but the most efficient moderators were found to be solid rare gases [50] developed in the 1980's and 90's and achieving efficiencies of around 1% [47].

In the ALPHA apparatus other processes are employed to maximise the efficiency of the moderator. One such process is annealing, where the temperature of the neon is raised to just below the sublimation point and then reduced again. It improves efficiency by removing imperfections in the crystal structure of the neon. Another is a technique known as field assisted moderation developed by Merrison and Jørgensen and co-workers [51, 52]. A layer

---

<sup>†</sup>The work function of a material is the minimum energy required to move an electron (or positron) from the bulk of a solid to a point just outside the surface, or in other words from the Fermi energy level into vacuum.

<sup>‡</sup>The efficiency of a moderator is given by the formula  $\varepsilon = \frac{\text{slow beam intensity}}{\text{source activity} \times x}$  where  $x$  is the branching ratio (or branching fraction, the probability of a radionuclide undergoing a particular decay mode) for  $\beta^+$  decay of the given source. For example, for  $^{22}\text{Na}$  the  $\beta^+$  branching ratio is  $\sim 0.9$ , the competing process in this case being electron capture (where a nuclear proton captures an inner shell electron producing a neutron and a neutrino).

of nitrogen is allowed to form over the surface of the neon. Secondary electrons produced through the positron bombardment are caught by the nitrogen molecules in this layer giving it a negative charge. This charge helps to draw positrons out of the neon which otherwise would have annihilated near the surface.

Over time, impurities on the surface of the moderator and the growing thickness of the nitrogen layer (due to the nitrogen gas used in the accumulator section as described in 2.4.2) will degrade its efficiency. Once this degradation is judged to be too severe a new moderator must be grown (typically after around 5-7 days).

The source end of the positron apparatus was maintained at a high vacuum of around  $10^{-9}$  mbar in order to increase the lifetime of the moderator and hence the mean intensity of the beam, resulting in an increase in the number of positrons available in the accumulator section. This was achieved with an oil free magnetically levitated turbo pump backed by a scroll pump (at the position indicated in figure 2.3). It was important to maintain an oil free environment throughout the apparatus so as not to introduce large hydrocarbon molecules anywhere into the vacuum system. Such molecules have a very high effective collisional cross-section for positrons which leads to high annihilation rates [53, 54], and hence a reduction in the lifetime of accumulated positrons.

The source holder (and hence also the moderator) was maintained at a positive potential (typically 70 V). This forces positrons which escape the surface of the moderator to be accelerated away from it. A series of water-cooled magnetic coils (operating at a magnetic field of 0.03 T) then restricts the motion of the positrons (which follow the field lines) forming them into a beam. The first two coils at the source end were placed in a configuration which produced a slight field minimum at the midpoint between them (centred on the positron source). This configuration meant that the field automatically compressed the positron beam slightly as it was transported away from the source. A third coil (known as the jog coil) was placed around 2 cm higher than the first two. The purpose of this coil was to remove unwanted high energy positrons. Low energy positrons follow the field misalignment and are steered through the jog coil. High energy positrons are not steered as strongly by this field so are not transmitted through the coil and annihilate on the wall of the apparatus. These position of these coils is indicated in figure 2.3.

The low energy beam then passes into the accumulator through a 1m long narrow-bore pipe. A long water-cooled solenoid (shown in figure 2.3) is mounted on the pipe and produces a field of around 0.03 T. This extends the field from the source section and prevents the beam from expanding and hitting the walls. This narrow pipe is included as a pumping restriction to reduce contamination of the moderator by the relatively nitrogen rich environment

of the accumulator (see section 2.4.2).

### 2.4.2 Accumulation

The accumulation section of the apparatus (shown schematically in figure 2.3) consists of a series of electrodes held in a vacuum chamber inside a 0.14 T water-cooled solenoid. The combined electric and magnetic fields form a Penning trap to confine the positrons. During accumulation, positrons lose energy through interactions with nitrogen gas and some become trapped. Eventually a plasma<sup>§</sup> is formed which can be manipulated by a rotating electric field. These processes will be described below.

A standard Penning trap uses three hyperboloid electrodes (a ring and two endcaps) to produce a harmonic electric field. This has a saddle point at the centre confining the particles axially. A strong homogenous magnetic field provides radial confinement. The axis of the trap is defined by the magnetic field. The positron accumulator uses a variation of this known as a Penning-Malmberg trap where the electric field is not harmonic over its entire length (only the section where the positrons finally accumulate). In this apparatus axial confinement is instead provided by a series of cylindrical electrodes (allowing for easier loading and transfer of positrons into and out of the trap).

The motion of the particles in the Penning trap has several important consequences, so it is worthwhile here to include a short discussion. Itano and Wineland give a summary of this motion on page 42 of their paper on laser cooling of ions [55]. The motion of the plasma as a whole approximates that of a single particle so the single particle case can be considered. The trap consists of a uniform magnetic field  $\vec{B} = B_0\hat{z}$  along the z axis and a quadrupole electrostatic potential of the form

$$V(x, y, z) = A_0(2z^2 - x^2 - y^2).$$

This gives an equation of motion for an ion of mass  $M$ , charge  $q$  and position  $\vec{r}$  of

$$M\dot{\vec{v}} = -q\vec{\nabla}V(\vec{r}) + (q/c)\vec{v} \times \vec{B} \quad (\vec{v} \equiv \dot{\vec{r}}).$$

This motion is characterised by three components. A simple harmonic motion at frequency  $\omega_z$  in the z direction, and a superposition of circular motions at frequencies  $\omega'_c$  (the modified cyclotron frequency) and  $\omega_m$  (the magnetron frequency) in the  $xy$  plane, as given by

$$\omega_z = (4qA_0/M)^{1/2},$$

---

<sup>§</sup>Henceforth the word ‘plasma’ will be used to refer to a one component or non-neutral plasma.

$$\omega_m = \omega_c/2 - (\omega_c^2/4 - \omega_z^2/2)^{1/2},$$

$$\omega_c' = \omega_c/2 + (\omega_c^2/4 - \omega_z^2/2)^{1/2}.$$

Here  $\omega_c = qB_0/Mc$  is the ordinary cyclotron frequency. These solutions assume that  $\omega_c^2 > 2\omega_z^2$ , since otherwise the motion is unstable. The magnetron motion can be interpreted as an  $\vec{E} \times \vec{B}$  drift of the centre of the cyclotron orbit around the trap axis. Note that these equations demonstrate that the axial trapping potential cannot be made arbitrarily large. As  $A_0$  increases,  $\omega_z^2$  increases and  $\omega_m$  and  $\omega_c'$  become imaginary, in physical terms radial confinement is lost.

The total energy is a constant of the motion,

$$E = E_k + E_p = \frac{1}{2}Mr_z^2\omega_z^2 + M\Omega(\omega_c'r_c^2 - \omega_m r_m^2),$$

where  $\Omega = \frac{1}{2}(\omega_c' - \omega_m)$ . Note that the magnetron component of the potential energy is negative.

In the accumulator used by ALPHA, seven gold plated copper electrodes of varying size formed a three-stage trap. The electrodes were separated and electrically isolated from each other by 2 mm diameter sapphire balls seated in machined grooves. This allowed each electrode to be biased individually. The fourth electrode was split into six identical pieces each electrically isolated. A phase shifted sinusoidal potential could be applied to each sector forming a rotating electric field (known as a rotating wall). This was used to compress the positron plasma and increase its lifetime.

The electrodes were biased as shown in figure 2.4. Positrons entering the accumulator would be reflected by the high potential on electrode 7. Provided they lose energy before returning to electrode 1 they would no longer be able to pass that potential barrier and would become trapped. The positrons lose energy by electronically exciting the nitrogen buffer gas. In order to ensure that most of the incoming positrons lose energy on the first pass through the machine the pressure of the buffer gas is fairly high in the first trapping stage. This is achieved by feeding the gas into the centre of electrode 2. The gas pressure decreases in each section of the trap due to the increase in volume because of the increasing radius of the electrodes. Two large 1200 ls<sup>-1</sup> oil-free cryopumps, situated at each end of the accumulator section, pump continually in order to maintain this pressure differential. Their position is indicated in figure 2.3.

Once the positrons are captured, further excitation of the buffer gas will eventually confine them in stage 2 and finally stage 3 of the trap. Here the gas pressure is lowest, decreasing the probability of annihilation, thus increasing the lifetime of the cloud. The positrons are accumulated, eventually forming

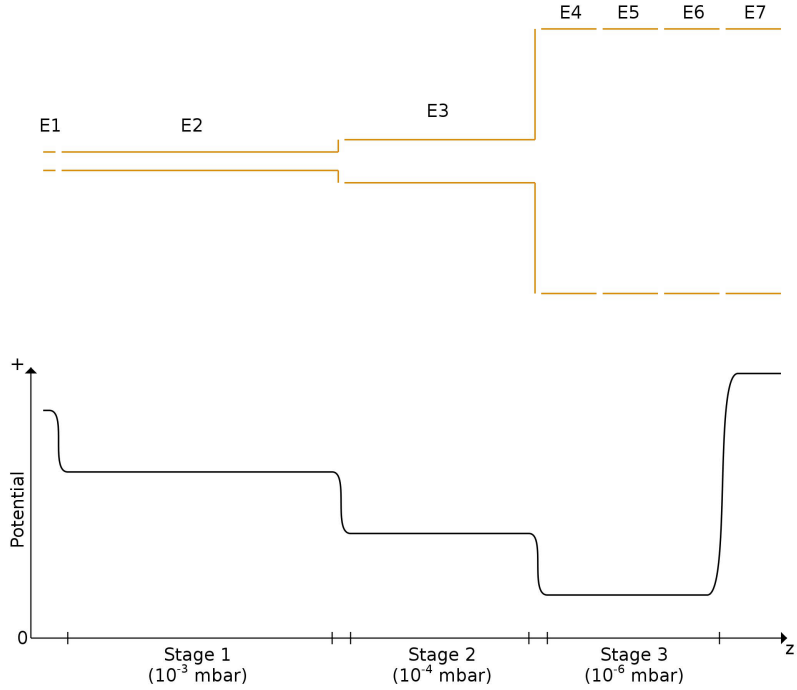


Figure 2.4: Schematic of the positron accumulator trap electrodes and potentials. The nitrogen buffer gas pressure in each stage is shown and the electrodes are numbered E1 to E7: E4 was six-way segmented for application of the rotating wall and E7 was the gate electrode.

a plasma when the dimensions of the cloud are much larger than the Debye length, given by:

$$\lambda_D = \left( \frac{\varepsilon_0 k T_e}{n_e e^2} \right)^{1/2},$$

where  $\varepsilon_0$  is the permittivity of free space,  $k$  is Boltzmann's constant,  $T_e$  is the positron temperature,  $n_e$  is the density of the positrons and  $e$  is the elementary charge. In ALPHA this occurs when around  $10^7$  positrons have been accumulated, which takes around ten seconds.

The number of positrons saturates when the rate of accumulation and the rate of loss are equal, thus a greater number can be accumulated by increasing the lifetime. Positrons are lost through annihilation on the buffer gas and through radial transport. Due to the negative magnetron potential energy, particles losing energy in collisions with the buffer gas are unstable towards an increase in  $r_m$  (the radius of the magnetron motion). In other words the particle cloud tends to expand during cooling (electromagnetic field asymmetries cause further expansion). As well as the low pressure of the buffer gas in the third stage the lifetime can be further increased by application of the rotating wall. The positron plasma has a large space charge and hence its

own electric field. This combined with the axial magnetic field means that the plasma's equilibrium state is one where it rotates around the axis with a constant angular frequency ( $\omega_m$ ). If the rotating field from the split electrode is at a higher frequency it causes the plasma to spin faster. Conservation of angular momentum means that this forces the plasma to a smaller radius, counteracting expansion. The heating of the positrons by this process is removed through further interactions with the buffer gas. This rotating wall technique was developed by Huang and co-workers [56], and its effectiveness for positron plasmas has been established [57, 58].

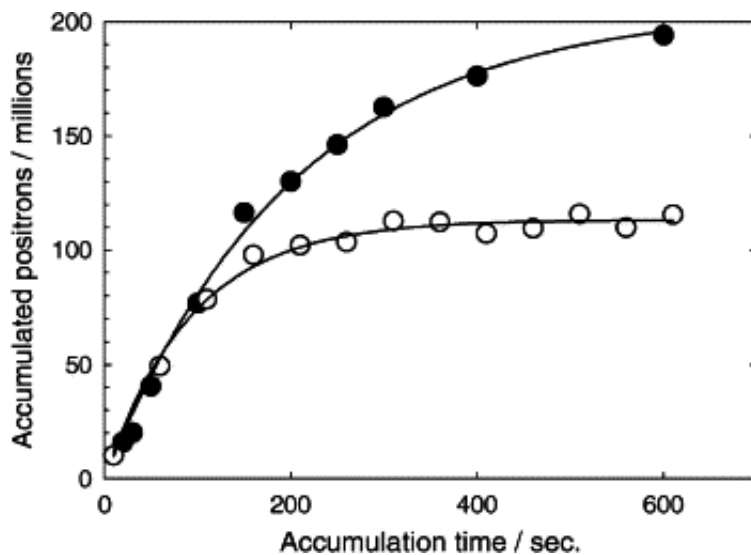


Figure 2.5: The effect of the rotating wall on the number of accumulated positrons. Filled circles are data for rotating wall ON, empty circles for rotating wall OFF. These data were taken with the ATHENA apparatus, with a positron source of approximately 40 mCi (i.e. around twice that of the source in the ALPHA apparatus). Figure taken from [3].

Figure 2.5 shows the effect the rotating wall has on the number of accumulated positrons over time. Note that the data in this figure were collected using the ATHENA apparatus, with a positron source of higher activity than that used in ALPHA. Consequently, for an accumulation cycle of equal length, more positrons would be accumulated in the ATHENA apparatus than the ALPHA apparatus. During a standard mixing in the ALPHA apparatus (described in section 2.5.8), around 75-100 million positrons would be accumulated, at a density of about  $2 - 4 \times 10^7 \text{ cm}^{-3}$ , in around 170 s. The entire accumulation cycle (including transfer) lasted around 300 s.

### 2.4.3 Transfer

The antiproton apparatus was maintained at an extremely high vacuum ( $< 10^{-12}$  mbar). During accumulation the pressure at the antiproton end of the positron accumulator (i.e. stage 3 and environs) was as high as  $10^{-6}$  mbar. In order to prevent contamination of the antiproton apparatus, a remotely operated mechanical valve (known as the transfer valve) was kept closed throughout the accumulation phase of the positron production cycle. Once the accumulation was over (rotating wall settings and accumulation times could be modified to tune the positron number) the potential on electrode 1 would be raised to prevent positrons entering the accumulator. The nitrogen feed would be switched off and the two cryopumps would quickly remove the remaining buffer gas, reaching pressures as low as  $10^{-9}$  mbar in  $\sim 30$  s. This was still significantly higher than that of the antiproton apparatus so a 20 cm long, 1.8 cm diameter pumping restriction was placed between the two. In order to ensure the positrons were transported through this restriction a pulsed magnet around the restriction (known as the transfer magnet) provided a field of 1 T to restrict their radial motion. It could be fired for 1 s every 200 s (this duty cycle was necessary in order to allow the coil time to cool between firings), which set the minimum time between positron transfers. The positions of the transfer magnet and transfer valve are indicated in figure 2.3 (on the far right of the figure).

Once the pressure in the accumulator was low enough the transfer valve would be opened. Then the transfer magnet would be fired and, while it was on, the blocking potential on electrode 7 would be removed. The plasma would move out of the accumulator and towards the antiproton apparatus. The potentials in the accumulator would be ramped slightly to ensure no positrons remained. A series of transfer electrodes were held at ground to ensure the plasma encountered no stray electric fields and continued into the positron trapping section of the antiproton apparatus (see section 2.5).

### 2.4.4 Positron Detectors

Two methods of detection were used by ALPHA to determine the number of positrons at various stages of their production and transfer. The first takes advantage of the fact that, during a positron annihilation, two characteristic back-to-back 511 keV photons are produced:

$$e^+ + e^- \rightarrow 2\gamma.$$

These can be detected using scintillating crystals and photosensitive diodes. The second method is to measure the induced charge when the positrons impact a conducting plate (known as a Faraday cup).

Several scintillation detectors were used at various points of the apparatus. A NaI detector was positioned near the valve which separated the source end from the rest of the accumulator and could be closed to allow access to the source end without contaminating the accumulator vacuum (and vice-versa). This detector and valve are shown near the centre of figure 2.3. The detector was accurately calibrated<sup>¶</sup> for this position and was used to count the number of positron annihilations when the valve was closed. This was used to monitor moderator growth and decay by observing the change in positron number over time. This was particularly useful during the annealing stage of moderator growth (which was difficult to automate so was done manually) and gave a good indicator of when a new moderator was required.

Several CsI scintillators were also placed at various points around the apparatus. They were accurately calibrated in June of 2006 and were used to establish positron numbers at various stages of positron accumulation and transfer. They were also used to monitor positron loss during transfer.

Two Faraday cups were available. One was on a movable armature and could replace the first transfer electrode after the end of the accumulator (shown in figure 2.3). At the end of an accumulation cycle positrons could be dumped onto this plate instead of being transferred to the antiproton apparatus. This was calibrated and gave a measure of the number of accumulated positrons before transfer. The other was the final antiproton degrader foil and its mount\*. This was connected to an amplifier and also used as a Faraday cup. It was calibrated to give a measure of the number of electrons loaded for antiproton capture, but could also be used to give a measure of the number of positrons successfully transferred.

## 2.5 The Antiproton Apparatus

The apparatus used for antiproton trapping and antihydrogen production in ALPHA is a development of the one used by ATHENA. The main difference is the addition of magnets intended for use as a magnetic minimum trap for neutral antihydrogen. The design considerations and underlying physics for this neutral trap will be discussed below, followed by a description of the rest of the ALPHA antiproton apparatus. One of the major design goals was the inclusion of an antihydrogen detector similar to that used by ATHENA so it is worthwhile to begin with a description of that apparatus, since ALPHA's detector had not been installed at the time the work in this thesis was completed.

---

<sup>¶</sup>The detectors are calibrated using an external radioactive source of known activity.

\*See section 2.5.5 for a description of the degrader and the reason for using electrons in the antiproton trap system.

### 2.5.1 ATHENA's Antihydrogen Detector

An important component of the ATHENA apparatus was the custom made antihydrogen detector. It allowed position sensitive detection of antihydrogen annihilations. This information was instrumental in providing many of the results of that collaboration. Incorporating a similar detector was considered to be vital to the redesigned apparatus for the ALPHA experiment, so was one of the major design considerations. A brief description of the ATHENA set-up follows.

The ATHENA apparatus consisted of a series of Penning-Malmberg traps. Antiprotons would be caught, cooled and mixed with positrons in a similar fashion to that used by ALPHA and described in the rest of this chapter. The main magnet (which provided the radial confinement in the traps) was a liquid-helium cooled 3 T superconducting solenoid with a bore of 150 mm diameter and 2.2 m length. Inside the bore the trap vacuum space and also the antihydrogen detector were housed. Outside the main magnet several plastic scintillation detectors were mounted for monitoring antiproton behaviour by detecting the pions created during annihilation. These were used to monitor the beam intensity and stability during degrading and also annihilation signals during antiproton cooling, transfer and mixing.

The antihydrogen detector was specially designed to detect the particles produced in an antihydrogen annihilation in spatial and temporal coincidence (a schematic is shown in figure 2.6). When an antihydrogen atom annihilates it produces several annihilation products. The positron annihilates with an electron and produces the characteristic 511 keV back-to-back photons. The antiproton annihilates on collision with a nucleus and produces several charged and neutral mesons, mostly pions:

$$\bar{p} + X \rightarrow a\pi^{+/-} + b\pi^0,$$

where X is the nucleus, and  $a$  and  $b$  are integers. The neutral pion has a very short lifetime ( $\sim 10^{-16}$  s) and decays into two photons with energies between 50 and 500 MeV, which can then produce positrons and electrons:

$$\pi^0 \rightarrow 2\gamma \rightarrow d(e^+ + e^-),$$

where  $d$  is an integer. If all these products were detected at the same time, originating at the same point in space, then it was highly likely an antihydrogen annihilation had occurred at that point.

The detector could be considered in two sections. The inner section consisted of two layers of sixteen double-sided position sensitive silicon wafers. Each wafer was 81.6 mm long, 19 mm wide and 2 mm thick and had 128 individual silicon strips running down the length and 64 strips across the width

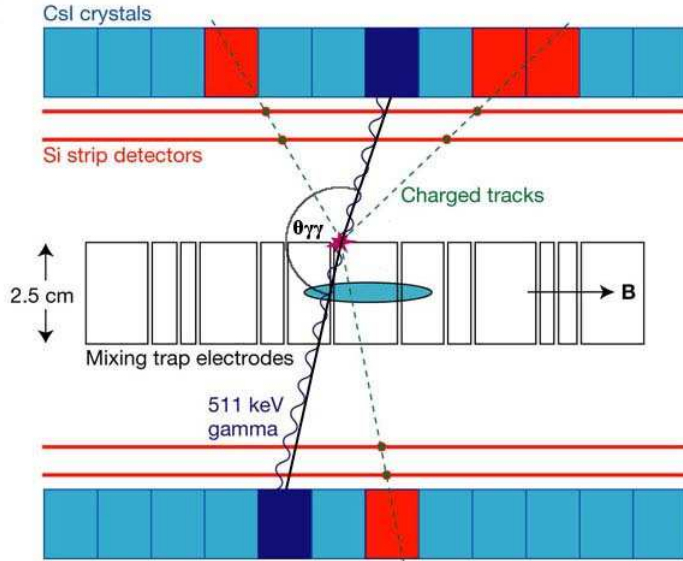


Figure 2.6: A schematic view of the ATHENA detector (figure from [4]). Reconstructed paths of annihilation products from an antihydrogen annihilation are shown. Also indicated is the opening angle,  $\theta_{\gamma\gamma}$ , for photons produced during positron annihilation.

on the opposite side. A charged particle passing through the wafer would induce a current in two orthogonal strips, the intersection of those two strips giving the position of the particle track. Two layers of silicon were used so that straight lines drawn between detection points in both layers of silicon could be used to reconstruct the paths of the charged pions. A third layer would have allowed measurement of the curvature of the particle tracks in the magnetic field but was ruled out due to space constraints. Two or more tracks which occurred at the same time and intersected at the same point in the mixing trap allowed the construction of an antiproton annihilation vertex at that point. There was a reconstruction uncertainty of  $\pm 4$  mm for the position of the vertex. This was mainly due to the unmeasured curvature of the charged pion trajectories, although multiple scattering of the pions on the trap electrodes and other intervening material also added to this uncertainty as did the resolution of the silicon strips.

The outer section of the detector consisted of sixteen rows of twelve scintillators made of pure CsI crystals. Each crystal was  $17 \times 17.5 \times 13$  mm in dimension, and was bonded to the outer aluminium support structure. These crystals had individual photodiode read-outs and were used to detect the photons produced in the positron annihilations. For each successfully reconstructed antiproton annihilation vertex, the opening angle for any two simultaneously occurring gamma events,  $\theta_{\gamma\gamma}$ , would be determined. For a

positron-electron annihilation this should be close to  $180^\circ$ , but there can be a small deviation in this angle due to the resolution of the crystals.

If the line described by the back-to-back gamma's coincided with the antiproton vertex (within 4 mm) at the same time (within  $5 \mu\text{s}$ ) then an antihydrogen annihilation event would be constructed at that point.

Typical results showing the radial distribution of reconstructed antiproton annihilation events are shown in figure 2.7. The figure shows results for both ‘cold’ and ‘hot’ mixing. Cold mixing was the standard procedure for the production of antihydrogen and is described for ALPHA in section 2.5.6 (the procedures in ATHENA and in ALPHA were similar). Hot mixing is a scheme where the positrons are heated to several thousand Kelvin by applying a radio frequency signal (either sinusoidal or white noise) to a sectored electrode over the positrons. This heating suppresses both antihydrogen formation processes (see section 2.5.2 for a discussion of antihydrogen formation). The mixing cycle could also be run without positrons (antiproton only), these two scheme’s were useful for investigating background and for comparison with cold mixing. If antihydrogen is formed then it is no longer contained in the trap and will travel to the wall of the trap (i.e. the electrode) and annihilate. A clear ring can be seen in figure 2.7 during cold mixing which is not present during hot mixing, thus demonstrating antihydrogen production.

Figure 2.8 is a plot of the opening angle for positron annihilation gammas for events simultaneous to antiproton vertex events. For cold mixing it shows a clear excess of events at  $\cos \theta_{\gamma\gamma} = -1$ . Those antiproton events contained in this excess (within the detector efficiency) are considered “fully reconstructed” antihydrogen events.

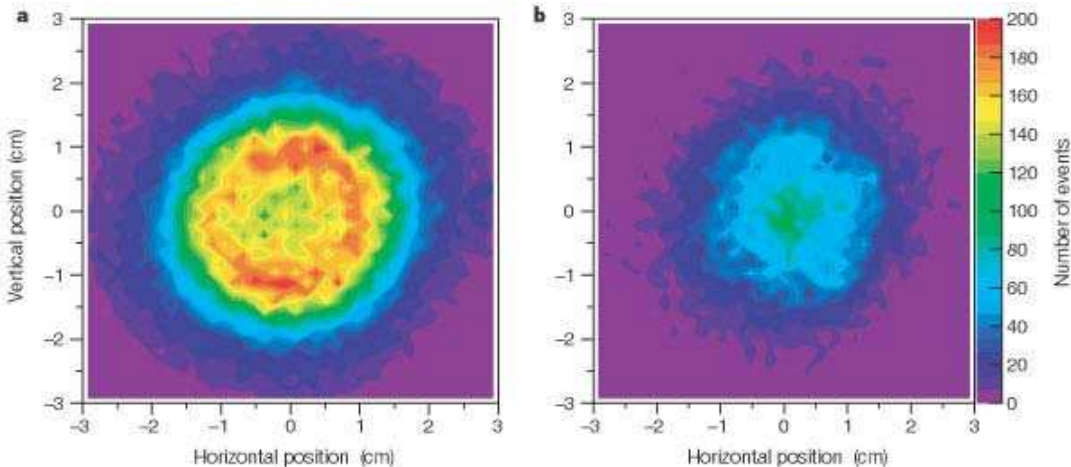


Figure 2.7: Reconstructed antiproton events for (a) cold mixing and (b) hot mixing (positrons are heated with RF noise before mixing in order to suppress antihydrogen formation). Figure from [4].

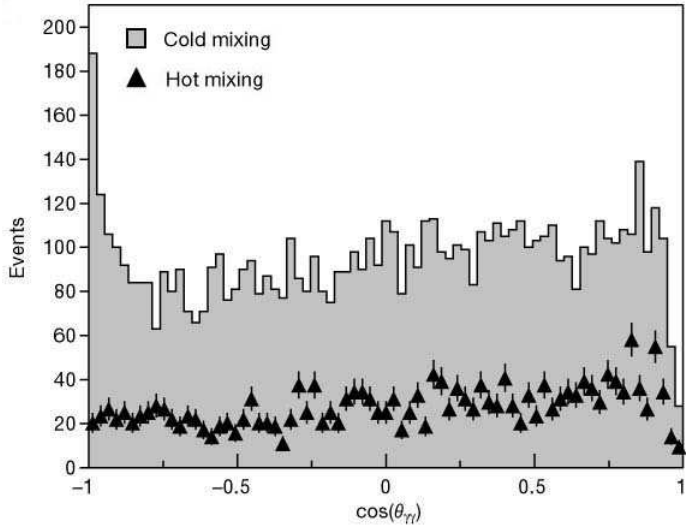
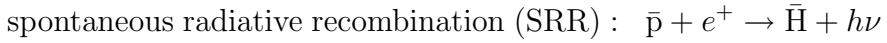


Figure 2.8: Positron annihilation events versus opening angle. For cold mixing a peak is clearly visible at  $\cos \theta_{\gamma\gamma} = -1$ . Figure from [4].

### 2.5.2 Antihydrogen Production Mechanisms

The design of an antihydrogen trapping apparatus, and the analysis of any data it generates, relies upon an understanding of the mechanisms by which antihydrogen forms in such an apparatus. For that reason, it is useful to discuss those mechanisms here.

In order to form a neutral bound state from two free particles, excess energy and momentum must be removed. This is typically via a third particle. Under the ultra-low temperature and high positron density conditions found in the ALPHA (and previously ATHENA) apparatus, two processes are thought to occur. These are:



and



A detailed review of these (and other processes) can be found in [5]; a brief summary follows.

In the radiative process, a positron collides with an antiproton and becomes bound, the excess energy being carried away by the emission of a photon. This can occur if the kinetic energy of the positron in the rest frame of the antiproton is less than the binding energy of the lowest atomic bound state

of antihydrogen. The rate coefficient  $\parallel$ ,  $\alpha^{SRR}$ , for this reaction was given by Stevefelt et al. [59] and Müller and Wolf [60] as

$$\alpha^{SRR} = 4.3 \times 10^{-13} \left( \frac{\text{eV}}{kT_e} \right)^{0.63} \text{cm}^3 \text{s}^{-1},$$

where eV is an electron volt,  $k$  is Boltzmann's constant, and  $T_e$  is the positron temperature (as earlier). If the assumption is made that the two particle species have uniform density and overlap completely then the rate for this process is the product of the rate coefficient, the total number of antiprotons,  $N_p$ , and the positron density,  $n_e$ , as

$$R^{SRR} = N_p n_e \alpha^{SRR}.$$

Thus the rate for this process scales with positron density and temperature as  $n_e T_e^{-0.63}$ .

In the three-body process two positrons collide in the Coulomb field of an antiproton. The “spectator” positron removes energy of the order of  $kT_e$  leaving the other positron bound to the antiproton, typically in a high Rydberg state (i.e. a highly excited state). These high Rydberg atoms can be re-ionised in further collisions but occasionally the positron will be scattered into a state with enough binding energy so that it cannot easily be re-ionised. Mansbach and Keck [61] gave the rate coefficient,  $\alpha^{TBR}$ , for this reaction as

$$\alpha^{TBR} = 2 \times 10^{-27} n_e \left( \frac{\text{eV}}{kT_e} \right)^{9/2} \text{cm}^3 \text{s}^{-1}.$$

Note that this formula was derived in the case of zero magnetic field. Penning trap antiproton experiments take place in a field of several Tesla. In such fields the plasmas are highly magnetised. This means the positron cyclotron radius is small in comparison to its classical distance of closest approach to the antiprotons so this process is suppressed somewhat. Glinsky and O'Neil [62] find it to be around a factor of ten lower than the zero field case.

If the same assumption is made as above for the radiative process then the rate for this process is given by

$$R^{TBR} = N_p n_e \alpha^{TBR}.$$

Thus the rate for this process scales with positron density and temperature as  $n_e^2 T_e^{-9/2}$ . This means that for the conditions in the ALPHA apparatus

---

$\parallel$ The rate coefficient is the recombination rate per  $\bar{p}$  at a particular  $e^+$  density, averaged over a presumed velocity distribution (in this case a spherically symmetrical Maxwell-Boltzmann distribution).

(ultra-low temperature, high positron density) the three-body process is expected to dominate.

It is clear from the rates of these two processes that antihydrogen formation can be greatly suppressed by increasing the temperature of the positrons. Mixing with heated positrons can thus serve as the null case for any antihydrogen formation experiment.

### 2.5.3 Trapping Antihydrogen

The Penning-Malmberg traps used by ATHENA only provide confining forces for charged particles. Antihydrogen is neutral and so is not confined. Once formed, it continues along the trajectory of the antiproton, and, if it escapes the positron plasma and traverses the electric fields of the trap without re-ionising, it will eventually hit an electrode and annihilate. In order to confine it, use can be made of the force exerted by a magnetic field gradient on the atom's magnetic moment.

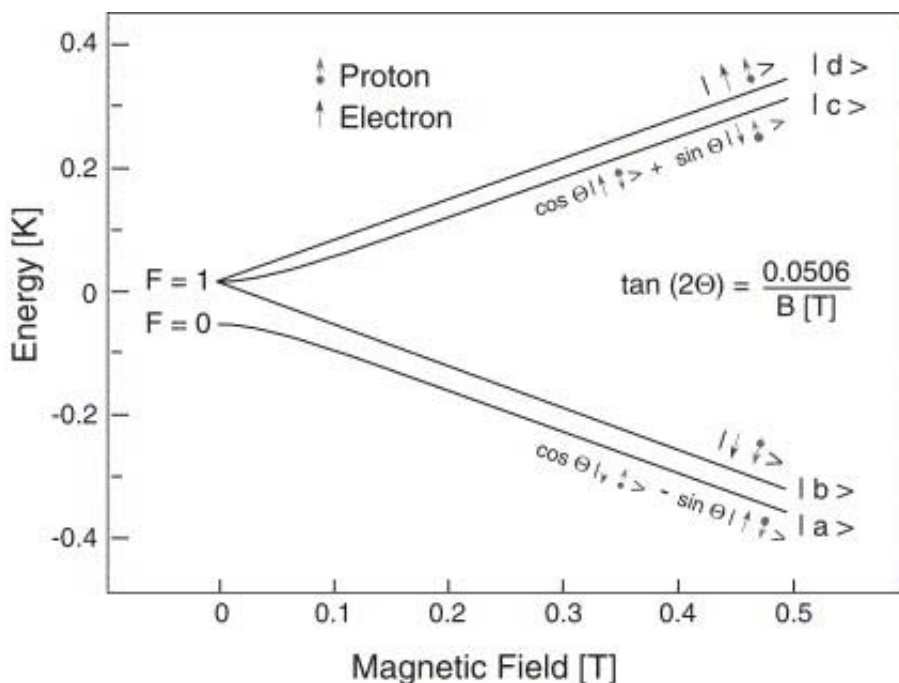


Figure 2.9: Energy levels of hydrogen in the 1S state in an external magnetic field. For antihydrogen the spin labels and magnetic moments are reversed (figure from [5]).

The electronic ground state of the antihydrogen atom is separated into so-called “low-field” and “high-field” seeking states (illustrated in figure 2.9). Atoms in the low field seeking states (states c and d in the figure) can be trapped in a magnetic field minimum provided that the difference between

their total magnetic potential energy at the wall of the trap (where the field has strength  $B$ ) and the centre of the trap (where the field has strength  $B_0$ ) is higher than the kinetic energy of the atoms at the centre. The well depth for such a trap can be expressed as a potential energy,  $kT = \mu(B - B_0)$ , where  $k$  is Boltzmann's constant and  $\mu$  is the magnetic moment. For ground-state antihydrogen  $\mu$  is equal to the Bohr magneton ( $\mu_B$ ). Thus, only atoms with kinetic energies corresponding to temperatures of  $0.67 \text{ K}T^{-1}$  and lower will be trapped. The trap depth for excited states, like those formed in the three-body process dominant in ALPHA, can be significantly deeper. In that case the magnetic moment is given by  $\sqrt{l(l+1)}\mu_B$ . So, for example, the trap depth for an antihydrogen atom with a positron in the 2p state ( $l = 1$ ), would be around 1.4 times deeper than for the ground state. However, only ground state antihydrogen can be easily used for precision spectroscopy.

Since high field seeking states cannot be trapped in the magnetic minimum, any transition between states c, d and a, b in figure 2.9 must be avoided. At zero field states c and d are mixed with state b, so spin-depolarising Majorana transitions can occur allowing some of the previously low-field seeking atoms to escape the trap. In order to avoid this, the centre of the trap must have a non-zero magnetic field.

The trap configuration typically used to confine low-field seeking hydrogen is known as an Ioffe-Pritchard trap [63, 64] (shown in figure 2.10). A set of coils is arranged to give a field minimum at the centre of the trap without having a zero-field location. A pair of coaxial solenoids at either end of the trapping volume (sometimes known as mirror coils) provide axial confinement as well as ensuring a non-zero field at the centre. A quadrupole (or higher order) multipole field is superimposed over the entire length of the axial well in order to provide radial confinement.

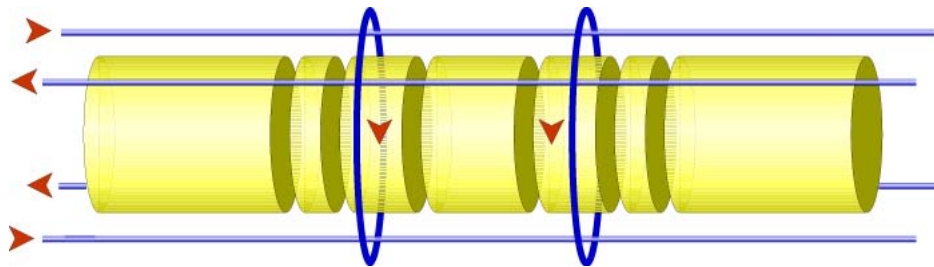


Figure 2.10: A typical Ioffe-Pritchard trap configuration. Red arrows show the direction of current in quadrupole and mirror coils. Penning trap electrodes are also shown as a visual aid.

### 2.5.4 ALPHA Magnet Design

In the ALPHA apparatus the fields that make up the neutral trap have to be superimposed over the solenoidal field required for confinement of the charged positron and antiproton plasmas used to create the antihydrogen. This solenoid field must be of sufficient magnitude to allow efficient synchrotron cooling of positrons and electrons. A stronger field also means that the incoming antiprotons are more tightly constrained so allowing more to be caught (see section 2.5.5 for a discussion of antiproton catching). The equivalent solenoidal field in ATHENA had a magnitude of 3 T. Ideally, magnets powerful enough to create an arbitrarily deep neutral trap would be constructed to allow a similar solenoidal field to be uniformly applied over the whole antiproton apparatus.

Only superconducting magnets are of sufficient strength to make a well of significant depth. However, superconducting wire can only support a limited current before becoming normally conducting. This critical current density depends on the local transverse magnetic field at the wire (see figure 2.11). The strength of the multipole, and hence the maximum depth of the neutral well, depends on this current density. For this reason the neutral trap cannot be arbitrarily deep. In order to maximise the depth of the well the background solenoidal field must be minimised. The decision was made to design a neutral trap to be contained within a background solenoidal field of magnitude 1 T.

### Multipole Order

The positron and antiproton plasmas must remain confined in order to produce antihydrogen. Common Penning traps rely on cylindrical symmetry to guarantee charged particle confinement [65], and this symmetry is broken by the multipolar field of a neutral trap. The consequences of this have been the subject of some debate [66, 67]. More recent experiments [68] have shown that quadrupolar fields of the magnitude necessary for antihydrogen trapping sharply degrade the confinement of the charged constituents. This is particularly evident, for appropriate length plasmas, when the ratio of the quadrupole field  $B_2(r_0)$  to solenoidal field at the plasma radius,  $r_0$ , exceeds about  $B_2(r_0)/B_z \geq 0.05$  [68, 69].

The magnitude of the field of an infinitely long multipole of order  $s$  scales with radius  $r$  as

$$|B_s(r)| = K_s r^{s-1},$$

where the  $K_s$  are constants and  $s$  defines the order of the multipole (e.g. a quadrupole for  $s = 2$ , an octupole for  $s = 4$ , etc.). Figure 2.12 shows the field dependence for  $s = 2-5$  where the field strength is normalised to unity at the

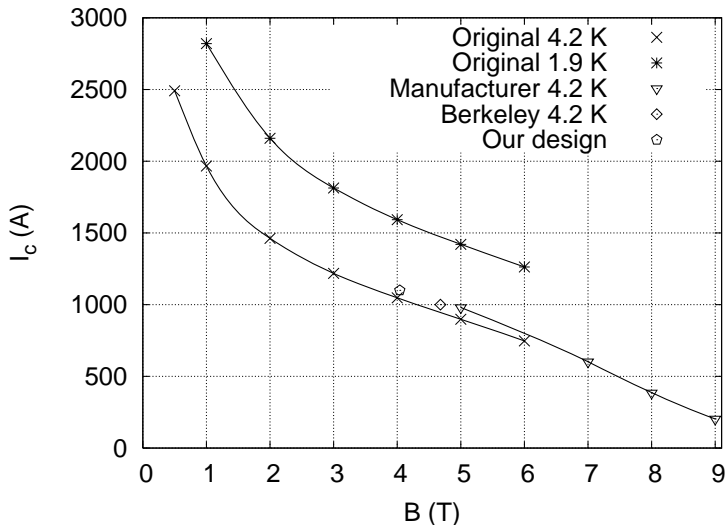


Figure 2.11: Critical current,  $I_c$ , at various magnetic fields for the wire used to construct the ALPHA multipole magnet. All data points were taken using wire with a copper/superconductor ratio of 0.9:1 in a seven stranded cable bundle that was manufactured by Supercon [6]. The points marked “Berkeley” and “Our design” used 0.33 mm wire, the remaining points used a very similar 0.303 mm wire. The two “Original” data sets were taken at the Brookhaven National Laboratory (where the ALPHA magnets were constructed), while the “Manufacturer” data set was taken by Supercon. These three sets were taken with short wire samples and set likely upper bounds on the performance of the wire when incorporated into a magnet. The “Berkeley” point comes from measurements of a prototype magnet at U.C.Berkeley, and is very close to the short sample performance when adjusted for the increased radius. The “Our design” point is located at ALPHA’s intended operation point. Figure from [7].

electrode inner wall radius,  $r_w$ . The maximum field magnitude in a multipole occurs at the coil inner radius and is proportional to the current density in the conductors there. With superconducting wires the current density is, to first order, only dependent on the type of conductor and the local magnetic field magnitude. Thus, to first order, the field at the wall of the multipole is independent of the multipole order [67].

While the maximum field, and hence the trapping depth, is roughly independent of the multipole order, the interior field is not. The higher the order of the multipole, the lower the interior field. The positron and antiproton plasmas extend only a small way to the trap wall. Consequently, for a given trap depth, they will be subject to smaller multipole fields as the multipole order is increased. The plasmas in ALPHA have radii of about  $r_0 \leq 0.2r_w$ . If the assumption is made that the maximum azimuthally asymmetric field that

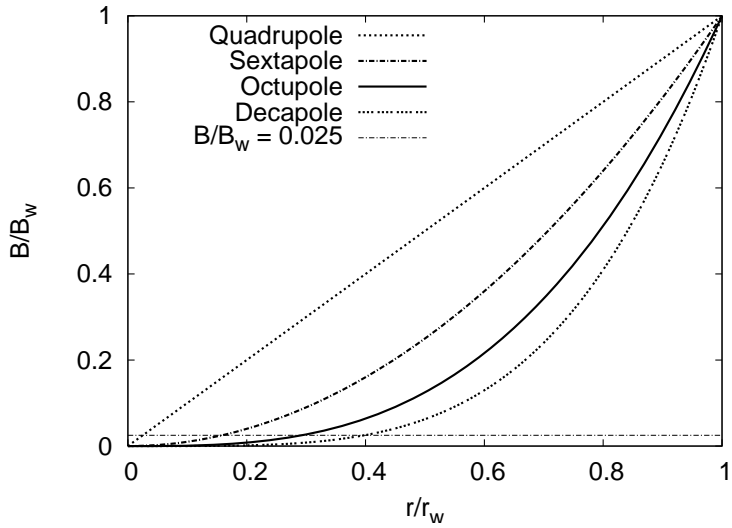


Figure 2.12: Radial field dependence for  $s = 2-5$  (quadrupole through decapole) normalised to unity at the electrode wall radius. The significance of the horizontal line is explained in the text. Figure from [7].

the plasmas can tolerate for a higher order multipole is similar to that of a quadrupole, then the limit for tolerance of a quadrupole field can be extended to the more general limit  $B_s(r_0)/B_z \geq 0.05$ . This limit corresponds to the horizontal line in figure 2.12 (the multipole field at the wall is about twice the solenoid field), and is satisfied by octupoles and higher order multipoles for all radii less than  $0.2r_w$ .

The multipole support form, the vacuum wall and the interior electrodes all have finite thickness. This means that the trap inner wall radius is considerably less than the coil inner radius. This causes the effective maximum field at the trap wall radius to be significantly reduced from the field at the coil radius, a reduction that increases sharply with multipole order. For example, for an octupole of inner radius 25 mm, and a net form, wall and electrode thickness of 2.5 mm, the useful field is reduced by 27%. It was decided that an octupole was the best compromise between minimising the field felt by the plasmas and maximising the neutral trap depth.

### ALPHA's Neutral Trap

ALPHA's neutral trap thus consists of an octupole and two mirror coils. The design of the octupole was severely constrained by the need to minimise material between the trap vacuum and the detector (in order to improve detector efficiency by minimising the scattering of annihilation products). This led to the use of some novel techniques (described below). The mirror coils were on

the edges of the interaction region of the apparatus and so were made with more standard methods.

The critical current in the octupole was around 1100 A, giving a surface current density for a single layer of around 8800 A mm<sup>-1</sup>. To generate fields of several Tesla the surface current density must be several times greater, so it was necessary to use several layers of superconductor. Contributions to the field strength from outer layers fall off as  $r^3$ , so in order to balance the need for a large field with our need to minimise material it was decided to use 8 layers.

When energised, the mirror and octupole coils press outward with considerable force. Calculations show the resultant pressure may exceed 40 bar. To contain these pressures the coil is wrapped with pre-tensioned fibreglass *s*-glass roving. To provide a safety margin, the tension in these tapes exceeds the calculated maximum pressure by 25%. When the coils are de-energised these tapes have no opposing force to counterbalance their own tension. This pressure must be supported by the coil form. However the support form could not be arbitrarily thick as we need to maximise the useful octupole field. After careful consideration of all the forces the form thickness was set to 1.25 mm of 316 LN stainless steel. To further reduce the material between the octupole and the trap vacuum it was decided to wind the magnet directly onto the vacuum wall, eliminating the need for a separate support form. This has an additional advantage of ensuring the vacuum wall will be at 4.2 K and hence will be an excellent cryopump.

The octupole is wound in a serpentine pattern rather than the more common racetrack pattern. By doing this and then reversing the winding direction and azimuthally staggering adjacent layers by 45°, almost all of the axial field that would occur otherwise is cancelled. This means that the axial well is formed entirely by the mirror coils and is thus easier to manipulate. It also means that the mutual inductance between the mirrors and the octupole is reduced.

In addition to staggering the coils on adjacent layers, the number of turns and turn spacing in each layer is adjusted to give as perfect a  $\cos 4\theta$  distribution as possible by minimising the next allowed  $\cos 12\theta$  field harmonic term. The magnet is wound using 11 (innermost), 11, 13, 13, 15, 15, 15, and 15 (outermost) wires in each leg on successive layers. This gives a calculated maximum  $B_{norm}$  for the octupole running at its maximum current of 1100 A, when all other elements in the system are energised, of 4.04 T. This is the intended operating point and as shown in fig 2.11, it is within the critical current for the octupole.

Because of the unique design (serpentine pattern, staggered ends and increasing turns per layer), the octupole could not be wound using conventional

techniques on a machined form. It was made using a novel technique developed at the Brookhaven National Laboratory, USA. The wire is initially ultrasonically glued into place, and then permanently secured with G10\*\* spacers (in winding gaps), *B*-stage epoxy, and the glass fibre overwraps [70]. This technique allows the wires to be placed in almost any pattern, with complete freedom to change the pattern between layers. The BNL technique also removes the need for steel collars to contain the magnetic forces as is commonly done in high field accelerator magnets.

The mirror coils each have four layers of 30 turns. They have an inner radius of 43.5 mm and the coil centre to coil centre separation is 274 mm. They are wound from the same wire as the octupole and will operate at a current of 750 A. The maximum field transverse to the mirror coil wires is around 3.7 T so this is well below the critical current for the wire. It would have been desirable to place the mirror coils over the straight wire region of the octupole in order to keep the transition region short, however this would have increased the outward pressure when the coils were energised and would require a thicker coil form to compensate for the correspondingly higher tension *s*-glass wrap. Instead the mirror coils were placed overlapping only the end turns of the octupole. The coil form was strengthened by increasing the thickness to 2.5 mm just beyond the octupole.

Placing the mirror coils outward opens up “holes” in the magnetic well. The optimal position was chosen by trading off the well depth loss from the holes with the well depth loss that would have resulted from thickening the form. Fig 2.13 shows  $|B|$  (all magnets are energised) as a function of the axial coordinate,  $z$ , for a number of radii spaced 1 mm apart. Each figure shows the field at a different azimuthal angle,  $\theta$ . As can be seen in (a) and (c), the smallest field along the well boundary is at the saddles near the mirror coils; it is through these holes that antihydrogen may escape. The lowest saddle has a value of 2.25 T. The lowest field within the magnet system has a value of 1.09 T giving the trap a well depth of 1.16 T, corresponding to a temperature of 0.78 K for ground state antihydrogen.

### Catching Solenoid

The background solenoidal field for the trap system is restricted to 1 T due to the physical limitations of the neutral trap magnets. However the antiprotons that exit the final degrader do so at a large range of angles and momentum (large transverse emittance). In order to catch as many as possible, the antiprotons must be steered into the trapping region. The stronger the solenoidal field that the antiprotons encounter, the greater the number

---

\*\*A high strength glass-epoxy laminate with low thermal conduction

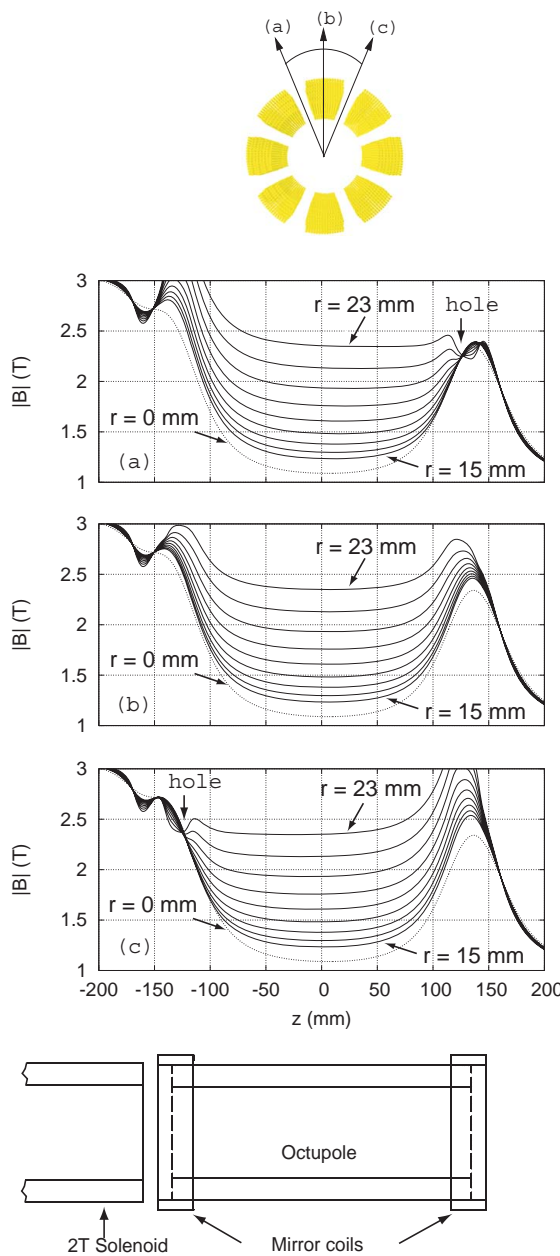


Figure 2.13: The top picture is an axial view of a cross section in the middle of the magnet system indicating the azimuthal angles for the planes for (a), (b) and (c). These three plots show the total field for a number of different radii as a function of  $z$ . The radius for subsequent solid lines differs by 1 mm: (a)  $-22.5^\circ$ ; (b)  $0^\circ$ ; and (c)  $22.5^\circ$  (see text). The bottom picture shows the schematic magnet assembly. Fig from [7].

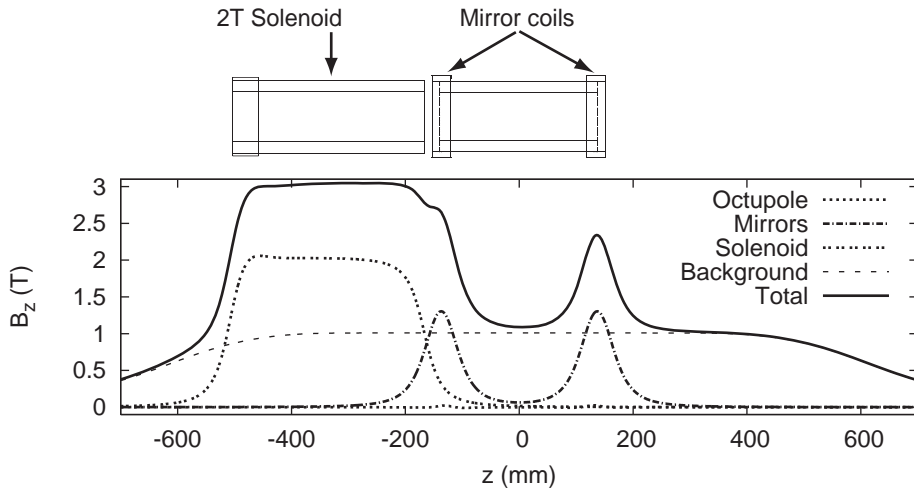


Figure 2.14: Magnetic field on axis for the magnet assembly including the 1 T background field from the large-diameter external solenoid. Fig from [7].

that will be steered into the trap. For this reason an extra, internal solenoid was placed adjacent to the upstream mirror coil (see figure 2.14). This internal solenoid is constructed from the same wire as the octupole. It has 8 layers over most of  $\sim 340$  mm length. The upstream end ( $\sim 45$  mm) has 10 layers in order to compensate for the fact that the external solenoidal field is dropping off in that region. At 230 A it adds around 2 T to give a 3 T region around 300 mm long for antiproton catching.

### 2.5.5 ALPHA Trap Configuration

The ALPHA antiproton apparatus (shown in figure 2.15) is made up of several distinct components. The main magnet supplies the background solenoidal field for radial confinement of the charged antiprotons and positrons. Inside the bore of this magnet is the detector space, the cryostat which contains the inner solenoid and the magnets for the neutral trap, the trap vacuum and finally the electrodes for axial confinement and manipulation of the charged particles. Outside the main magnet are all the ancillary systems, including the vacuum systems.

#### Main Magnet

The main magnet is a liquid-helium cooled superconducting solenoid. It has a 1.7 m long bore of 260 mm diameter. It can be energised up to 130 A to give a field of 3 T.

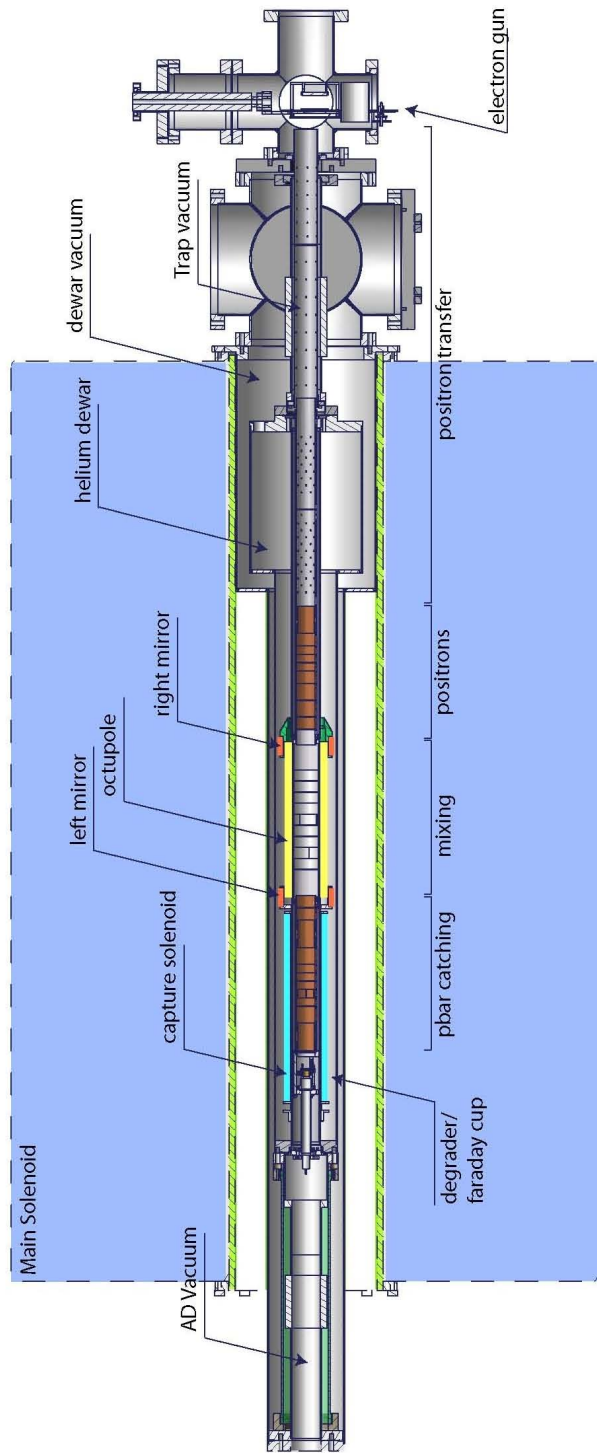


Figure 2.15: Schematic representation of the ALPHA antiproton apparatus. See text for details.

Prior to installation the magnet was surveyed and the position of the bore relative to two permanent external survey points was determined. The field was then mapped. This was achieved with a machine available at CERN. The machine consists of three orthogonally aligned Hall probes mounted on the end of a long rigid arm. The arm can be displaced by the machine with an accuracy better than 0.1 mm. The arm was aligned to the bore of the magnet and then the probes were scanned through the bore in a grid pattern. A measurement was taken from the Hall probes at regular intervals and written to a file. These data were then used to determine the homogeneity of the magnet and the relative divergence of the field from the mechanical bore. Figure 2.16 shows the axial component of the solenoid field, as measured at the axis of the mechanical bore of the ALPHA main magnet. The plot includes the total field and the field homogenous to 1% for the ALPHA magnet, and also the ATHENA magnet for comparison. It can be seen that the homogenous region in the ALPHA magnet is considerably shorter than was the case in the ATHENA magnet. However, after careful consideration of the possible placement of other trap elements (e.g. electrodes and other magnets) it was decided that this reduced homogeneity could be accommodated and the magnet was suitable for use in the ALPHA apparatus.

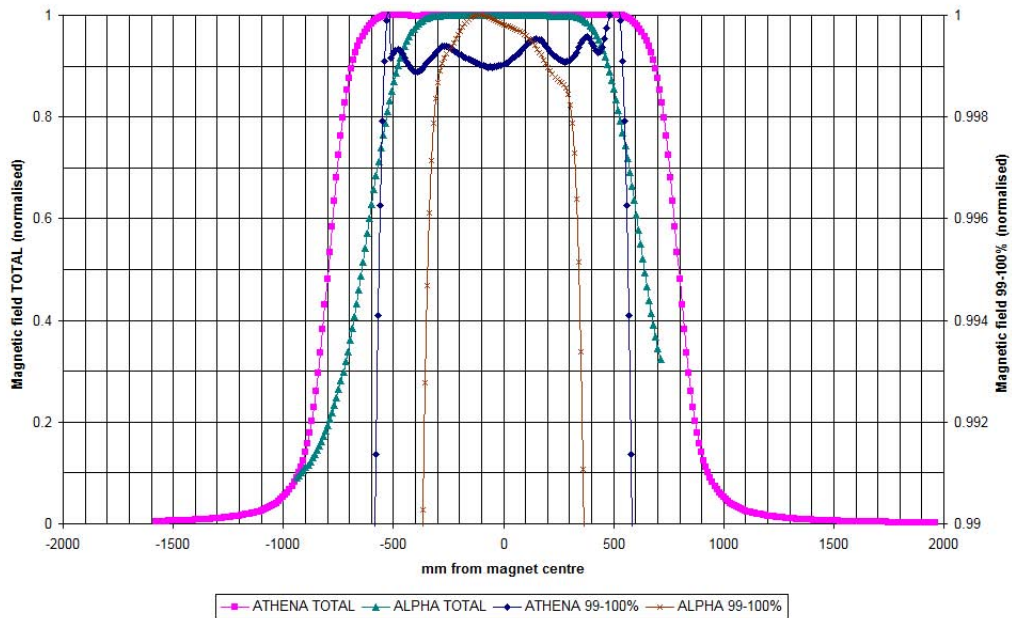


Figure 2.16: Magnetic field in the main ALPHA solenoid. Included are the total field (on the left axis) and the field homogenous to 1% (on the right axis). The field from the ATHENA apparatus is included for comparison.

The divergence of the field from the mechanical axis,  $D$ , was determined from the measured transverse field components  $B_x$  and  $B_y$  using the formula  $D = \sqrt{B_x^2 + B_y^2}/B_z$ , where  $B_z$  is the measured component in the  $z$  direction. This simple treatment gave a divergence of the central region of the field of around 9 mrad (or approximately 9 mm over 1 m). This is similar to that measured in the ATHENA apparatus (around 10 mrad), so was considered acceptable. Note that this apparent misalignment of 9 mrad could derive from a misalignment of the Hall probes rather than one of the field and mechanical axes. The Hall probes were around  $1 \text{ mm}^2$  in area, so a misalignment of the probes of order 10 microns would account for the apparent misalignment of the field. An attempt was made to remove this systematic error by taking a second measurement with the probe arm rotated by  $180^\circ$ , and subtracting the results. This operation gave a corrected divergence of around 4.4 mrad, however the rotation proved difficult and the accuracy of the turn can not be guaranteed. However, it is reasonable to assume that this gives an upper limit on the actual divergence of the field. Both results are presented in figure 2.17.

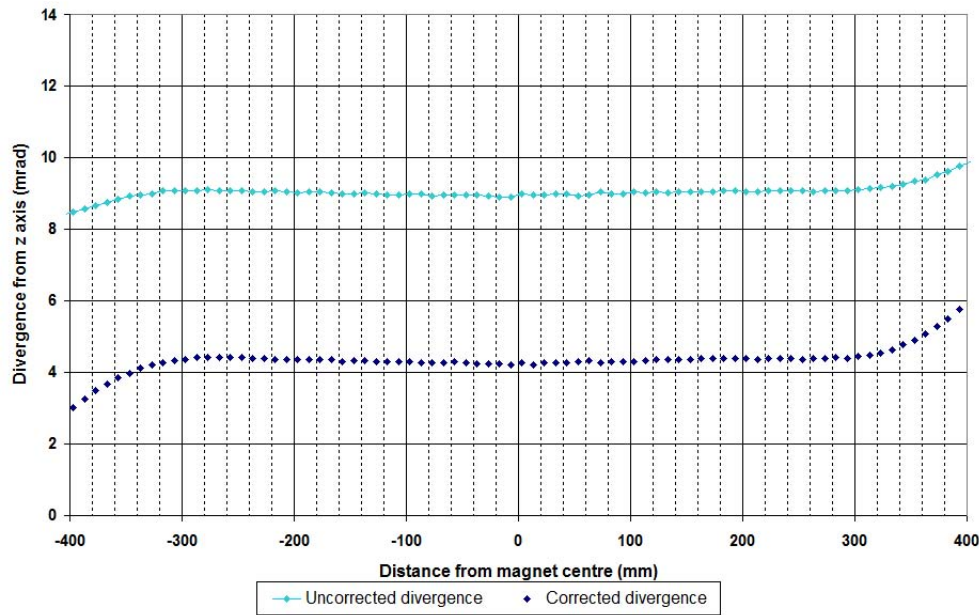


Figure 2.17: Measured divergence of the magnetic axis from the mechanical axis of the main ALPHA solenoid.

Further improvements of the analysis could have been used to ensure that the magnet was oriented with its magnetic axis correctly aligned with the AD beam path. However, since the calculated divergence was similar to that in ATHENA, it was not considered necessary to pursue the analysis further. Instead, with the assistance of the CERN surveyor, the magnet was placed with its mechanical bore aligned to the AD beamline.

## Cryostat

The steel wall on which the inner magnets are wound serves as both the inner wall of the cryostat helium space and also the trap vacuum outer wall. Outside this is the vessel which contains the liquid helium (visible in figure 2.15). There is a knife edge on either end of the helium vessel in order to make ultra high vacuum (UHV) connections. The downstream end (upstream is defined to be the direction from which the antiprotons arrive, i.e. the AD end) is connected via a bellows to the trap vacuum pumping system and further to the positron accumulator. The upstream end of the trap vacuum is closed by an indium-sealed electrical feedthrough flange. This flange also contains the vacuum window, a  $15\ \mu\text{m}$  thick piece of steel which separates the trap vacuum from the AD vacuum and also serves as a layer of degrading material for the antiprotons (see section 2.5.5). Another bellows is attached to the upstream end of the helium vessel to separate the outer vacuum chamber (OVC) from the AD vacuum. Bellows are used in order to make a long thermal path from the liquid helium to room temperature. The helium vessel is wrapped in super-insulation (many thin layers of metallised mylar separated by fine nylon mesh) to reduce the radiative heat load.

This construction is housed inside the OVC. Feet made out of G10 hold the helium vessel away from the OVC wall at the downstream end. The upstream end is supported by a G10 tube which holds the bellows at that end rigid. This bellows then makes an UHV connection to the inside of the OVC wall. The G10 pieces ensure that the helium vessel, and by extension the inner magnets and trap electrodes, is placed precisely at a well defined position inside the OVC. Their poor conduction helps keep the thermal load on the helium vessel as low as possible.

The OVC is held in place by mounting onto a flange at the downstream end of the main magnet. The upstream end is held by several adjustable brass screws which allow the OVC to be centred along the mechanical axis of the main magnet bore.

The cryostat helium space is connected to a vertical helium dewar by three flexible tubes. One contains the superconducting leads to the magnets, one contains a number of sensor wires and voltage taps for monitoring the magnets and the other is left empty for increased helium flow. The superconducting leads are then spliced onto vapour-cooled leads (VCLs) which make the transition to the external bus-bars (large copper bars that carry the high current from the power supplies). The VCLs are housed in a helium dewar, which is supported by a vacuum cross mounted to the outside of the main magnet (shown in figure 2.15).

### **Electron Gun Armature**

Mounted outside the VCL vacuum cross was another smaller vacuum cross (visible in figure 2.15), on which was mounted a remotely controllable stepper motor system. The motor was used to precisely raise and lower a movable armature inside the vacuum system. On this arm was mounted the electron gun, a transfer electrode for use during positron transfer, and a detector assembly consisting of an MCP, phosphor screen and a mirror that reflected the image of the screen out of a vacuum window on one side of the cross. This detection system was not used during the 2006 beam time as there was no camera available to take images of the response of the screen. However, it was used during the 2007 beam time and is described in chapter 5.

### **Catching and Cooling Antiprotons**

In order to perform experiments on antihydrogen it is necessary to create it at a low kinetic energy. The largest contribution to the energy of the antihydrogen atom comes from the momentum of the antiproton (having a much larger mass than the positron). The antiprotons delivered in the AD ejection are still at a relatively high energy. For this reason it is necessary to reduce the energy of the antiprotons as much as possible before mixing with positrons. Two methods are employed to achieve this. The first is to place degrading material in the path of the antiprotons before they reach the trapping region of the apparatus. The second is to allow caught antiprotons to interact with cold electrons. Both techniques are described below.

If the antiproton bunch is steered onto a very thin foil some fraction of the antiprotons will pass through to the other side and continue. Most of those that are transmitted through the foil will be reduced in energy. For example, the PS200T experiment found that for a beam of antiprotons at a kinetic energy of around 5 MeV, if 50% of the incoming antiprotons were stopped in the final foil, then the remaining 50% emerged from the downstream end with a significant fraction at keV energies (1-2% below 30 keV) [71]. In this way the total number of antiprotons with low kinetic energy (a few keV) can be increased.

In ALPHA the degrading material consists of a rotatable foil, the beam counter, the vacuum window and the final degrader foils which are mounted on the Faraday cup inside the trap vacuum (for descriptions of the beam counter and Faraday cup see section 2.5.7). The rotatable foil is used in order to vary the total degrading thickness. As the foil rotates from perpendicular to the direction of the incoming beam, the effective thickness of material in the beam

path increases  $\dagger\dagger$ . As the thickness increases the chance that an antiproton will be reduced in energy increases but so too does the chance that it will annihilate inside the foil. A curve is made showing the number of caught antiprotons versus the thickness of the rotatable foil. This curve has a maximum when approximately 50% of the incident antiprotons are transmitted through the foil, or equivalently around halfway through the range curve $\ddagger\ddagger$  for the foil.

The highest energy that an antiproton can have and still be caught is set by equipment limitations. In order to capture the incoming antiprotons a blocking potential is set at some point in the trap. Particles that do not possess enough kinetic energy to pass this barrier are reflected back towards the trap entrance (they are restricted to motion along the axis by the magnetic fields from the main and catching solenoids). Then, before they can return to the degrader foil and annihilate, another blocking potential is quickly raised at that end of the trap thereby confining them. In the ALPHA apparatus this potential is restricted to 5 kV. In other words antiprotons with an axial kinetic energy of 5 keV or less are the only ones that will be trapped. This equates (after degrading) to approximately 0.1% of the antiprotons in the AD ejection. The system for this fast high voltage switching is described in detail in appendix A.

The second method of cooling the antiprotons is applied to those that have been caught by the high voltage. Before AD ejection occurs the central shallow area of the trap is loaded with a cloud of around  $10^8$  electrons. On a timescale of around a second these will cool through the emission of synchrotron radiation in the strong magnetic field to the ambient temperature of the trap (usually maintained at 20 K or below during antiproton operation). The captured antiprotons pass through the electrons many times, eventually losing energy through Coulomb interactions with them (which then radiate the excess away). Thus, the antiprotons are reduced to the temperature of the electrons and hence the temperature of the trap. The electrons are eventually removed by lowering the confining potential on one side on a timescale such that many of the light (and hence faster moving) electrons can escape while losing few of the much heavier antiprotons. This process (known as electron kicking or e-kicking) is repeated several times until all of the electrons are removed. This electron kicking could be performed either in the antiproton catching region before the antiprotons were transferred into the mixing region, or after in the mixing region itself. There are reasons for and against each

---

$\dagger\dagger$ Effective thickness given by  $d = \frac{\text{thickness of foil}}{\cos(\text{angle of foil})}$

$\ddagger\ddagger$ The antiproton range curve for a material is a plot of the fraction of transmitted antiprotons versus the thickness of the material. For example the PS200T experiment at LEAR in CERN investigated degrading of antiprotons in 1992 and determined the range curve for antiprotons in aluminium [71].

approach which will be discussed in chapter three.

The number and density of antiprotons in the cloud prior to e-kicking and transfer could be increased by using a procedure known as “stacking” (described in more detail in 3.5). Instead of removing the electrons after a single antiproton shot, the trap is readied to catch additional antiproton shots. This procedure was typically used in order to not waste antiprotons while waiting for the positron accumulator to finish its cycle.

### Trap Electrodes

The electrodes in the ALPHA apparatus can generally be divided into three parts. Those that are used to catch and cool the antiprotons ejected from the AD, known as the catching trap, those that receive the transfer of positrons from the positron accumulator, the positron trap, and finally the central section which deals with mixing the two species of antiparticles together, the mixing trap.

The catching trap electrodes (designated E1 through E11 in 2006, see figure 2.18) were gold plated cylindrical aluminium electrodes with an internal diameter of 40 mm. Electrode E4 was a segmented electrode designed for application of the rotating electric field known as a rotating wall. Electrodes E1 (HVA) and E9 (HVB) were the high voltage (HV) electrodes used for catching antiprotons. The HV electrodes were separated and electrically isolated from their neighbours using ceramic pieces; all other electrodes were separated using ruby balls. The electrodes in the positron trap (E23 through E32) were similarly constructed also with an internal diameter of 40 mm. E32 (HVC) was another HV electrode placed so that experiments could be considered where the antiprotons would be caught directly in the mixing region, however this has not to date been considered worth pursuing. It was used as the catching electrode for the positron transfer in a similar fashion to HVA for antiprotons. The transfer electrodes (between E32 and the positron accumulator) were steel and not gold plated.

In order to minimise scattering material and, more importantly, maximise the useful octupole field, the mixing trap electrodes had to be made as thin as possible and placed as close to the vacuum chamber wall as possible. For this reason they were constructed using a water jet cutting technique which allowed for extremely high precision features (the design allowed a general tolerance of  $\pm 0.02$  mm).

Figure 2.19 shows the design of the thin electrodes used in the mixing trap. Figure 2.20 shows an enlarged view of a section of that design highlighting several important features. The electrodes were held together by tensioned

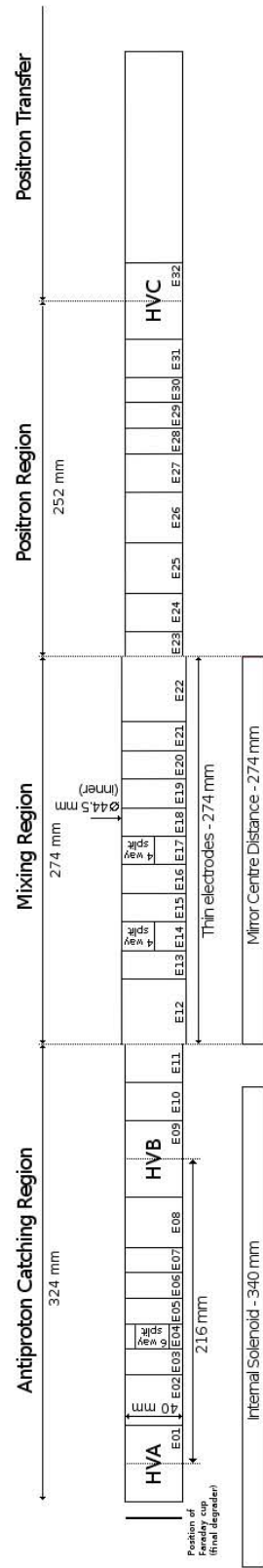


Figure 2.18: Schematic overview of the system of electrodes used in the ALPHA apparatus in 2006. Also shown are the positions of the internal (catching) solenoid and the centres of the neutral trap mirror coils.

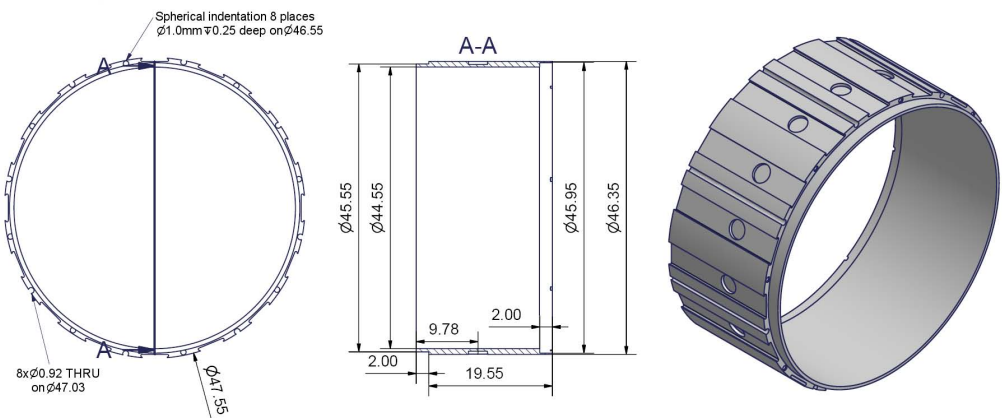


Figure 2.19: Thin electrodes used in the mixing trap region. See text for description.

aluminium wires that ran down lengths of Kapton<sup>†</sup> tube that fit precisely inside channels cut through the outer surface of each electrode (these channels are highlighted in green in figure 2.20). The Kapton tubes perform two functions. They ensure the aluminium wire does not short electrodes together, and they squeeze partially out of the channel on the outside of the electrode. These slight extrusions (which were repeated at 8 positions around the outer circumference of the electrode) both support the electrodes and, more importantly, ensure that they do not make contact with the vacuum chamber wall (which could short electrodes together). This removed the need for “feet” thus ensuring that the outer circumference of the electrodes was as close as possible to the vacuum chamber wall. The electrodes were held apart and electrically isolated from each other by ruby balls which sat in small depressions in the surfaces between each electrode, as shown in red in figure 2.20.

This novel design ensured the electrodes sat as close as possible to the chamber wall, but left very little space for wires to make electrical connections. Instead “strip-lines” were constructed which consisted of layers of Kapton and conductor sandwiched together (inner conductor surrounded by Kapton, then ground planes, then more Kapton) and then laser-cut to precisely fit in flat channels in the outer circumference of the electrodes. These channels are shown in light-blue in figure 2.20. The strip-lines were soldered to the electrodes at cylindrical wells on their outer surface (which can be seen in figure 2.19), and then spliced onto more typical cables further out of the system where space was no-longer at such a premium.

This design placed the inner wall of the electrode approximately 1.95 mm away from the inside of the vacuum chamber wall, or around 4.35 mm from the first layer of the octupole. Electrodes E14 and E17 were segmented electrodes

<sup>†</sup>Kapton is a polyimide film suitable for use in high vacuum and low temperature environments.

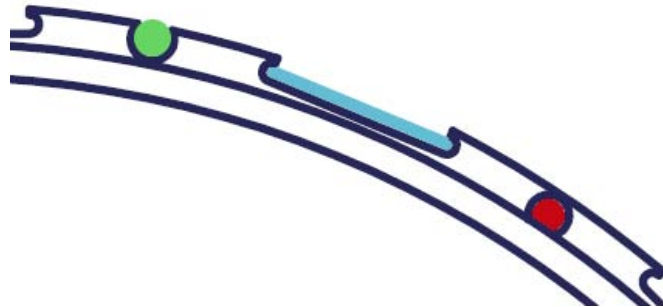


Figure 2.20: Enlarged view of a section of a thin electrode. The red area highlights a spherical indentation which is a seat for one of the ruby balls used to separate and electrically isolate electrodes. The green area highlights one of the channels used for the wires that hold the trap together and away from the vacuum wall. The light-blue area highlights one of the channels used for the strip-lines that make the electrical connections to the electrodes. See text for details.

for application of rotating-wall potentials.

### 2.5.6 Control System

There were many different systems involved in controlling the ALPHA apparatus. Figure 2.21 gives an overview of the most important. Over 100 different parameters were controlled, many requiring a high degree of timing precision. This precision was achieved via the sequencer. The sequencer was the top-level control system which coordinated the operation of the rest of the apparatus. It was built using a PXI framework (PCI eXtensions for Instrumentation), which is a PC-based platform for measurement and automation systems. PXI systems are composed of three basic components (shown in figure 2.22), the PXI-chassis, RT (Real-Time) controller, and peripheral modules. The chassis contains the high-performance PXI backplane, which includes the PCI bus as well as timing and triggering buses.

The RT controller is a custom computer built into a PXI module and installed directly into the PXI-chassis controller slot. It has a real time operating system and can take full advantage of the PXI backplane capabilities to deliver real-time deterministic performance and headless (i.e. not requiring control from outside the PXI system) reliable operation. An operating sequence would be designed (using a custom LabVIEW<sup>‡</sup> interface) on the sequence host computer, and then passed via a TCP/IP connection to the RT controller which then passed instructions to the peripheral modules.

---

<sup>‡</sup>LabVIEW is a graphical programming environment from National Instruments [72]. It is optimised for instrument control and data acquisition.

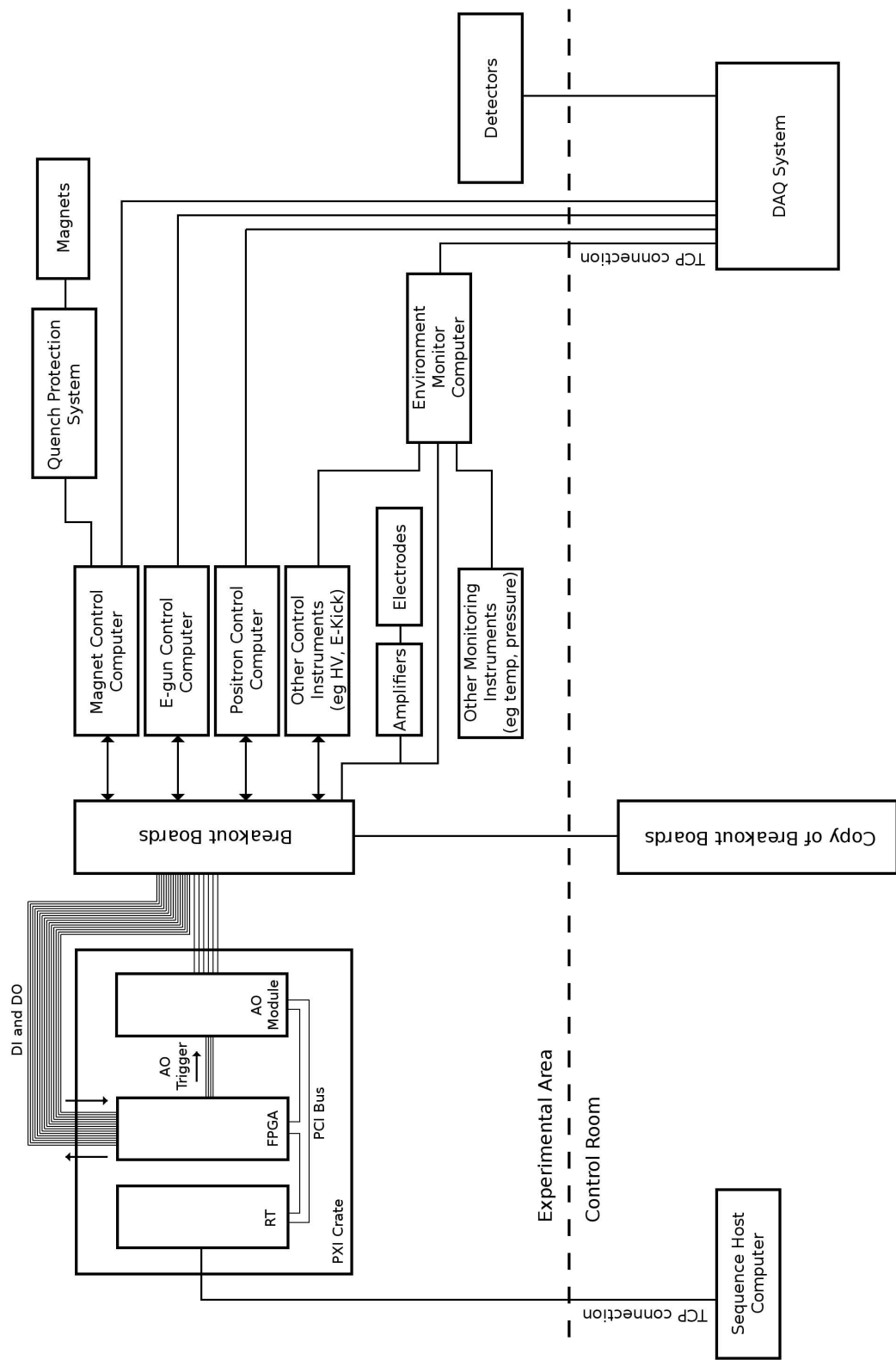


Figure 2.21: Schematic overview of the various control elements involved in running the ALPHA apparatus. See text for details.

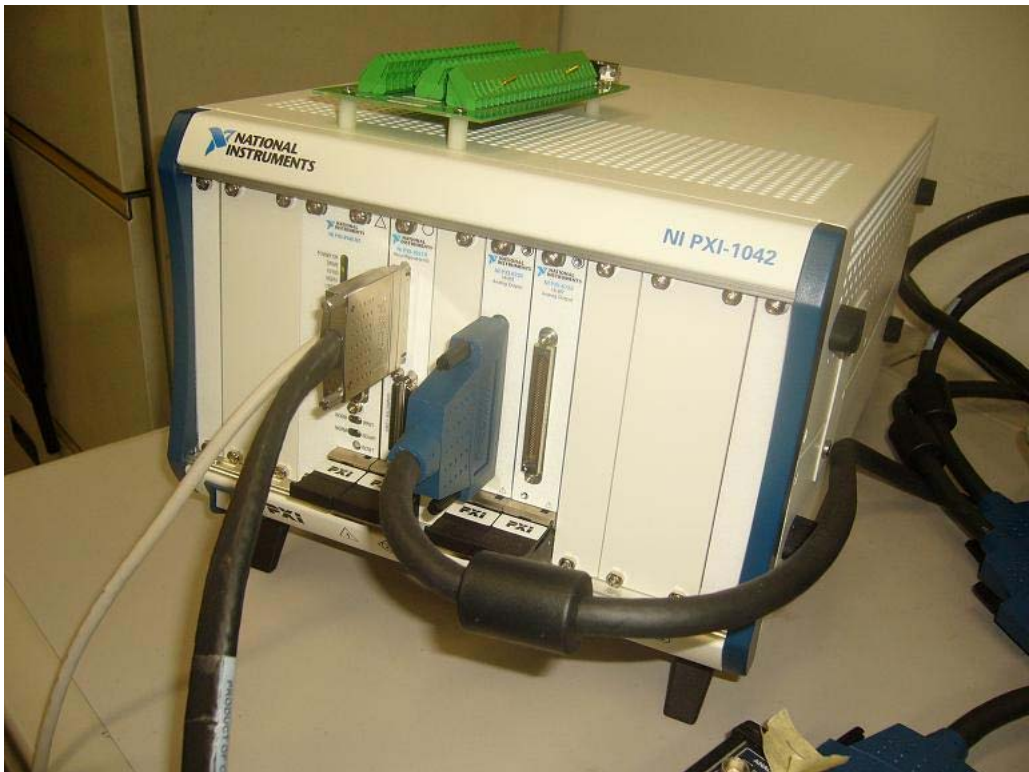


Figure 2.22: The PXI system used as the ALPHA sequencer. This picture was taken during system development. Modules shown (left to right) are; RT controller, FPGA module, 2xAO module, see text for details.

Synchronisation of PXI modules and all experimental operations was controlled by 2 Field Programmable Gate Arrays (FPGA), one for the catching region and one for the mixing and positron regions (known as the pbar and mix sequencers respectively). The FPGAs used by ALPHA had 8 analog input channels, 8 analog output (AO) channels, and 96 digital Input/Output (DI/DO) channels. They provided hardware level determinism of operations with a timing resolution of 25 ns. They were configured for ALPHA to have 80 digital output and 12 digital input triggers, and also 6 analog output triggers for the AO modules. Each AO module could create 8 independent analog signals in a range of  $\pm 10$  V, with 16 bit resolution, at an update rate of 0.75 MHz. The levels of the outputs were set by the RT controller and triggered by the FPGAs. These analog outputs were sent to amplifiers which drove the trap electrode potentials.

All of the inputs and outputs from the two sequencers were passed to the experimental area via a set of custom “breakout boards” designed and built at TRIUMF. These breakout boards separated the signals to individual BNC (for

the digital inputs/outputs) or LEMO (for the analog outputs) connectors<sup>§</sup>. Standard coaxial cables could then be used for connection to instruments. Each connection had a small LED positioned above it that illuminated to give a visual indication of activity on that channel. A copy of the breakout boards including duplicate output signals and activity LEDs was placed in the control room for monitoring sequencer activity.

Many of the digital inputs and outputs then passed (via other breakout systems and I/O cards) to several other control PC's; each used custom LabVIEW interfaces to control different parts of the apparatus. The magnet control computer used an FPGA based system to drive the quench protection system for the internal magnets. These magnets were designed to operate at high currents (1100 A for the octupole, 750 A for each of the mirror coils and 230 A for the internal solenoid), such that an unprotected quench would dump a large amount of energy into the magnet coils, likely destroying them (as well as vapourising a large amount of liquid helium causing extremely high pressures inside the magnet cryostat). The quench protection system was designed to protect the magnets by quickly cutting off the power supplies and dumping the stored energy into a system of resistors. This function would be triggered automatically in the event of a quench, but could also be deliberately triggered and was used in an attempt to identify trapped antihydrogen (see section 4). Because of the importance of continual operation of the quench protection system, the magnet control computer (and hence the controlling FPGA) were connected to an uninterruptible power supply. The main magnet was not connected to this system and was instead controlled directly from its own power supply.

The electron gun control computer coordinated the operation of the movable armature on which the electron gun was mounted (as well as the positron transfer electrode). It also controlled the power supply that drove the electron gun. The positron control computer coordinated the operation of the positron accumulator apparatus (described in section 2.4). Other instruments (such as the e-kick control system and the high voltage boxes) were controlled directly from the associated sequencer via the breakout boards.

The environment monitor computer collected data from several sources. It monitored the analog levels sent to the amplifiers as a measure of the potential applied to each electrode. It also monitored other instruments such as e-kick parameters, and voltage applied to the HV system. There were also several temperature and pressure sensors at various points, and helium level meters in the main magnet, cryostat and helium transport dewars, all of which sent data to the environment monitor computer. All these data, as well as data

---

<sup>§</sup>BNC is an industry standard connector type. LEMO is the name of a connector manufacturer based in Switzerland [73], the connectors in this case being the LEMO-00 connector.

from the magnet, positron and e-gun computers, were sent via TCP/IP to the DAQ system. The DAQ system also collected all of the signals from the various detectors. Section 2.5.7 describes the detectors and DAQ system.

### 2.5.7 Detection and Data Acquisition

The position sensitive antiproton annihilation detector designed for use in the ALPHA apparatus was not completed (or installed) during the period that this thesis covers. However, several other detector systems were installed. This section will describe the detectors used by ALPHA (during 2006), and will go on to describe the data acquisition (DAQ) system.

#### Current Transformer

The current transformer was an induction loop that passed around the antiproton beam pipe in the AD extraction line. As the antiproton bunch passed through the loop a current was induced in the transformer proportional to the number of antiprotons. This provided a good measure of the number of antiprotons delivered to the experiment in the AD ejection. It was an AD system, but the reading was sent to the ALPHA DAQ system shortly after each ejection (other experiments use the same device when they receive the beam). Large reductions in the reported current were often the first evidence of problems in the PS/AD cycle. The value was also used to normalise results from other detectors to the beam intensity.

#### Beam Counter

The beam counter was a  $60\ \mu\text{m}$  thick silicon wafer, separated into 5 independent sectors (as in figure 2.23). Each semiconducting silicon section acts as a diode, and as the charged antiprotons pass through the wafer some of their kinetic energy is deposited into the silicon and creates electron-hole pairs. By applying a bias voltage across the wafer these mobile charges can be collected before they recombine with each other. With a sufficient bias voltage, such that the majority of the liberated electrons are collected, the signal induced in the beam counter will be proportional to the number of antiprotons passing through it. Each of the five sectors was measured independently, so by comparing the beam intensity incident on each pad the position of the beam just before entering the trapping region could be determined.

Note that it should be possible to use the beam counter to measure the total number of incoming antiprotons. However, due to the fact that (in normal operation) the incoming beam was fairly diffuse at the position the beam counter was mounted, the current transformer was considered to give a much more reliable measure of that number.

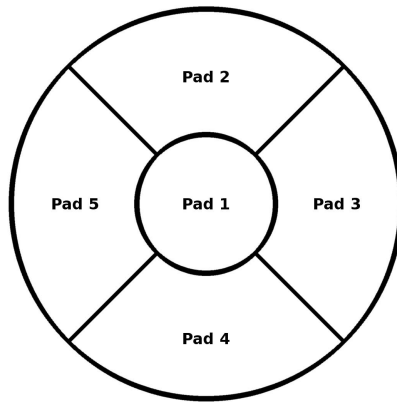


Figure 2.23: Schematic representation of the segmented silicon beam counter. The five sectors (or pads) are shown and labelled.

### Faraday Cup

The final degrading foil (described in section 2.5.5) was mounted in an electrode which was then mounted (on insulated stands) to the rotatable flange that was used to close the vacuum window. The foil and electrode were electrically connected to outside the apparatus, and together comprised the Faraday Cup (shown in figure 2.24). Electrons (or positrons) incident upon the Faraday Cup induce an electric charge. During a dump this charge was measured (via an amplifier) and used to determine the number of electrons (or positrons) present in the dump.

### HPDs

Two small scintillator<sup>¶</sup> pads were placed at different points in the ALPHA experimental area, one fairly close to the degrader end of the apparatus (known as HPD1), and one further away (known as HPD2). The response of each was measured via a hybrid-photodiode (or HPD). An HPD employs a photocathode separated from a photodiode by a gap with a high voltage difference (8-15 kV). Electrons produced by a photon incident on the photocathode are accelerated across the gap and produce a much greater response from the photodiode than the original photon would have.

The response of HPD1 could be used as a measure of the number of antiprotons dumped onto the degrader from the trap, but would saturate during

---

<sup>¶</sup>A scintillator is a substance which absorbs high-energy electromagnetic or particle radiation, and then releases that energy as photons. The response of such a material can be measured by collecting the released photons. The material is usually completely enclosed (typically with opaque plastic) to ensure that only internal photons are collected.

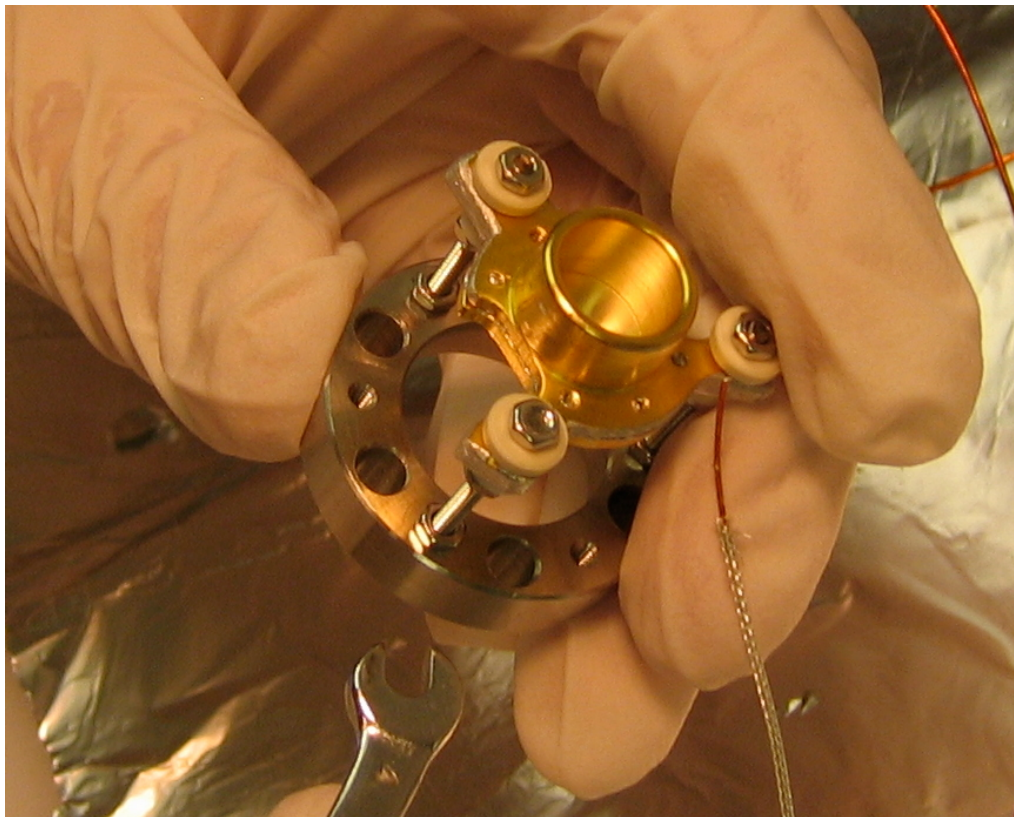


Figure 2.24: The Faraday Cup during construction. The final degrading foil can be seen in the centre of the cylindrical section of the electrode. Ceramic pieces used to electrically isolate the electrode from the mount are also visible.

the AD ejection. The response of HPD2 could be used as a measure of the number of antiprotons present in the AD ejection and hence served as an independent check on the current transformer.

### External Scintillators

Four large scintillator pads (known as PMT 1 through 4) were mounted in pairs on the outside of the main magnet, approximately aligned with the centre of the catching region and covering the final degrader. The response from these scintillators was measured with photo-multiplier tubes (or PMTs). PMT's consist of a photocathode, several dynodes, and an anode all mounted in a vacuum tube. Photons striking the photocathode material (a thin layer deposited on the entry window of the device) produce electrons which are accelerated by a focussing electrode towards the first dynode. The electrons hit the dynode with more energy than the original photon and cause more electrons to be released, which are in turn accelerated towards the second dynode. Each dynode is held at a more positive voltage than the previous

and the geometry of the chain of dynodes is such that a cascade occurs with an increasing number of electrons at each stage. Finally the anode is reached and the accumulation of charge produces a sharp current pulse, proportional to the number of incident photons. PMTs have a high gain, low noise, high frequency response, and can be made with a large collection area.

In ALPHA the PMTs were used to detect antiproton annihilations on the degrader during dumps (AD ejection would saturate the detectors). PMTs 1 and 2 were mounted together on one side of the main magnet, PMTs 3 and 4 on the other. They were mounted together so that any annihilation product would have to pass through two independent scintillators, thus any signal that appeared coincidentally in PMT 1&2 or PMT 3&4 could be counted as representing one antiproton annihilation. The total number of such events was counted (known as the “PMT OR” signal) and either used directly as a relative measure of the number of antiprotons dumped onto the degrader, or combined with the detector efficiency to give the absolute number.

## APDs

The external scintillators were too far from the mixing region to give a reliable signal for antiproton annihilation events during mixing. In order to generate such a signal, four scintillators were placed inside the bore of the main magnet adjacent to the mixing trap. The strong magnetic field in this region meant that PMTs and HPDs could not be used to measure the response of these scintillators. Instead they were read out using avalanche photodiodes (or APDs). In an APD a high reverse bias voltage is applied across the diode. Electrons produced by incident photons accelerate within the diode substrate and generate more electron-hole pairs. These electrons undergo the same acceleration and generate further electrons, a process known as an avalanche breakdown. The gain produced by the breakdown increases as the reverse bias voltage increases. The mean free path of an electron in this process is short (especially compared to that in a PMT or HPD) so an APD is essentially immune to the effect of an applied magnetic field.

The APDs in the ALPHA apparatus were used to count antiproton annihilations during mixing. An event was registered if two or more of the detectors fired in coincidence (within 100 ns). The time evolution of this event rate could then be compared to results from ATHENA and used as evidence of antihydrogen production (see section 3.7). The solid angle subtended by the detectors was about 35% of  $4\pi$ .

## Data Acquisition

Several different data gathering systems, and recording and display programs make up ALPHA's data acquisition system (shown in figure 2.25). This section will describe the operation of each element of the system.

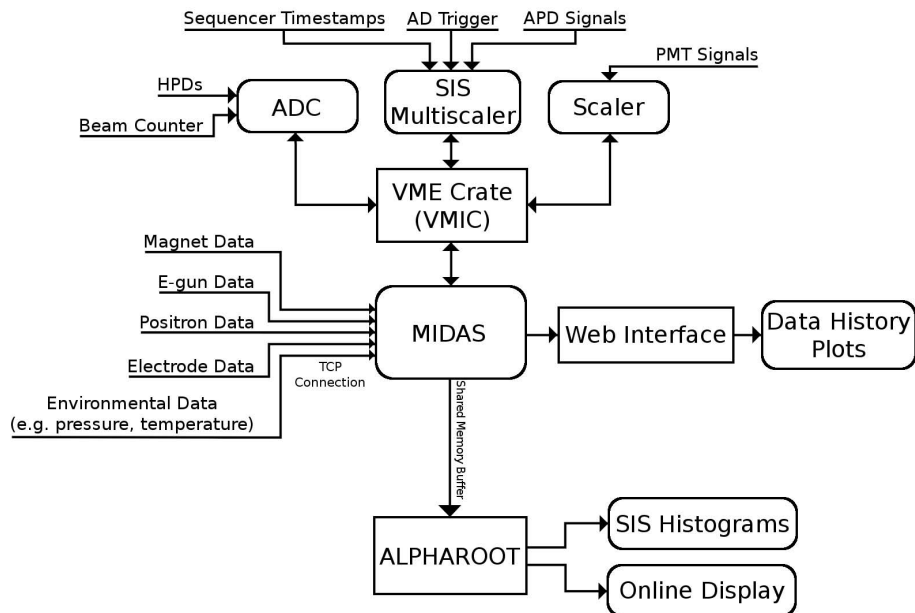


Figure 2.25: Schematic overview of the ALPHA data acquisition system.

Data from the detectors was brought to several VME<sup>||</sup> modules located in a VME crate in the control room. Signals from the beam counter and HPDs were digitised by the CAEN v792 ADC (Analog to Digital Converter) module. Signals from the external scintillators (PMTs 1-4) were counted by a CAEN v560 scalar module. All other signals (plus some of the outputs from the ADC and scalar) were sent to a SIS3840 multiscaler module. This module had 32 channels and supported 64 Mbytes of SDRAM. It could handle 250 MHz counting rates with 32-bit counter depth. For the ALPHA experiment, the SIS module was set up with a first-in-first-out input data buffer for primary use as a timing module for synchronisation of the incoming data. As each instrument performed an operation, a time-stamp was sent to the SIS module and the order of their arrival was then used to organise the data and ultimately coordinate it with sequencer operations (vital for the interpretation of particle behaviour within the apparatus).

<sup>||</sup>Versa Module Eurocard bus. This is an open-ended bus system that uses the eurocard standard. It was originally developed by Motorola.

Access to the ALPHA VME bus was provided through a VMIC VMIVME-7805 microprocessor. The VMIC was essentially a custom computer built into a VME module. It was capable of running most current operating systems and contained many of the features of a typical desktop computer. It was designated alphavme01 and was cross-mounted with desktop computers designated alphacpc04 and alphacpc05. All of these computers were running Scientific Linux 4. Data acquisition and display responsibilities were split between these three computers. The MIDAS\*\* software (including the web interface) ran on alphavme01, the ALPHAROOT analysis and visualisation program ran on alphacpc05, whilst alphacpc04 was reserved for offline analysis. The MIDAS event buffer was shared between all three computers.

The MIDAS data acquisition system was the central component of the DAQ. All data generated by the apparatus was passed through MIDAS to be organised and recorded. Fast data from the ADC, scaler and multiscaler modules were accessed directly by MIDAS frontends (data collection subroutines) via the VME interface. Other data were sent to MIDAS, through a TCP network connection, from custom LabVIEW programs that interfaced directly with the associated instruments. Once the data had been collected by the frontends it was organised and recorded by the so-called MIDAS backend (data handling and logging subroutines). The web interface contained the controls to start and stop data acquisition and recording, as well as displaying system messages and equipment warnings/alarms (which could be sent via the TCP connections along with data, or set individually via the web interface, e.g. the helium level low alarm). The web interface also included a plotting feature to display histories of the data coming into MIDAS (an example is shown in figure 2.26), and an electronic logbook (or e-log) which was used to record and archive information about experiments in place of a physical logbook.

The ALPHAROOT program ran in conjunction with the MIDAS system and provided preliminary analysis and data visualisation. It was built using the ROOT<sup>††</sup> framework and generated the online status display (shown in figure 2.27), and also histograms based on the data received by the SIS multiscaler. It was also used offline to generate specific histograms from data stored by MIDAS (for example, APD events during mixing as illustrated in figure 2.28).

---

\*\*Maximum Integration Data Acquisition System [74]. This is a flexible framework which can accommodate a variety of hardware and computing components, with a powerful recording and data distribution system. It was developed at PSI [75] and TRIUMF [76].

<sup>††</sup>An object oriented data analysis suite based in C++. <http://root.cern.ch/>.

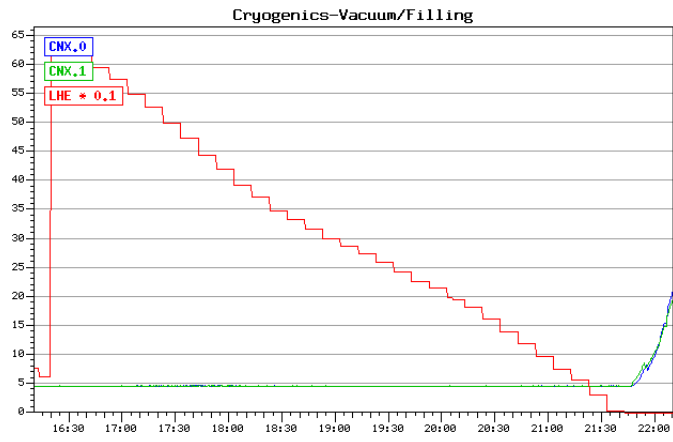


Figure 2.26: An example of a histogram produced by the MIDAS web interface. This histogram shows 3 variables; the helium level in the transport dewar (read once every 10 minutes), and the temperature reading from two cernox sensors in the cryostat.

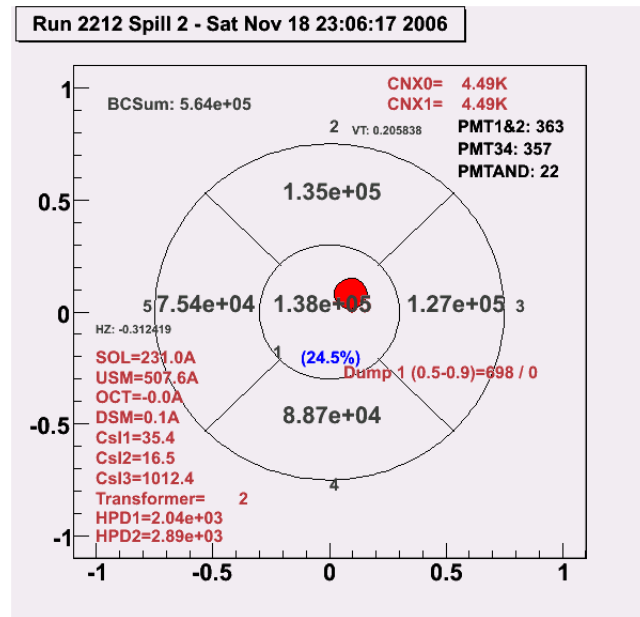


Figure 2.27: An example of the online status display generated by the ALPHA-ROOT program. Beam counter response plus several other status values can be seen. An image such as this one is generated (and updated as information arrives) for each AD antiproton ejection.

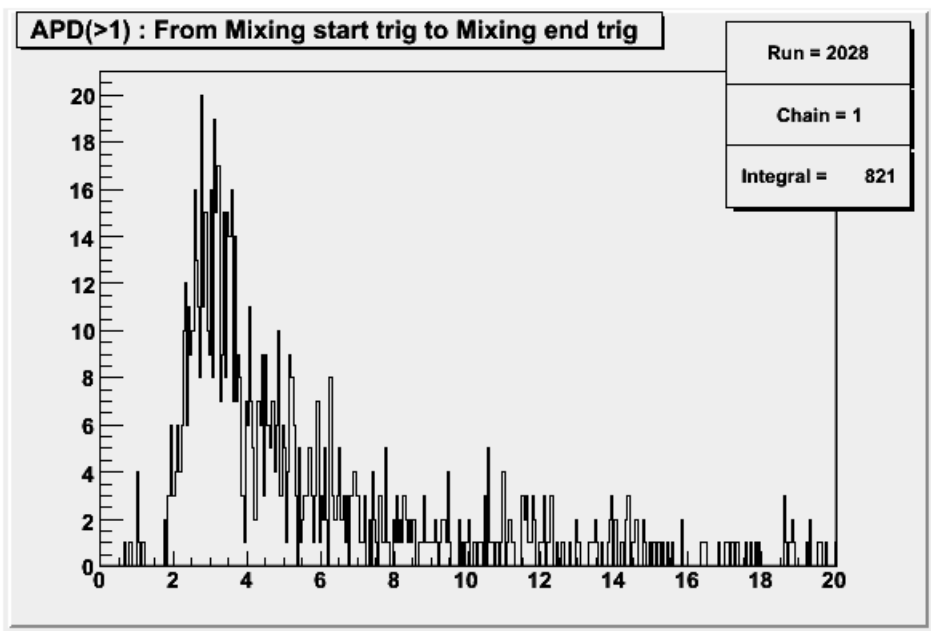


Figure 2.28: An example of a histogram generated during offline analysis using the ALPHAROOT program. This histogram shows the APD event rate (i.e. the rate of signals that appear in more than one APD coincidentally) from the “start of mixing” trigger to the “end of mixing” trigger.

### 2.5.8 Standard mixing

The operational sequence known as “standard mixing” was essentially the same as the one developed by the ATHENA collaboration and used by that group to demonstrate production of cold antihydrogen. It was used by ALPHA as the basic experimental cycle against which other experimental results (such as mixing in the presence of the octupole) could be compared.

Positrons were accumulated in an approximately 300 s cycle and transferred to the antiproton apparatus as described in section 2.4. In the standard cycle, all the electrodes in the mixing and positron regions (described in section 2.5.5) were used to receive the positrons after transfer. These electrodes were biased such that as the positrons cooled they were forced into the centre of the mixing trap and into a well that would later become the centre of the nested potential. During this time three antiproton shots were caught and cooled as described in section 2.5.5. The antiprotons were then transferred (using a procedure similar to that shown in figure 2.29) to a pre-injection well next to the nested potential.

Figure 2.30 demonstrates the potential manipulations involved during the actual mixing of the positrons and antiprotons. Antihydrogen formation begins as the antiprotons cool to a similar speed to the positrons, i.e. when the

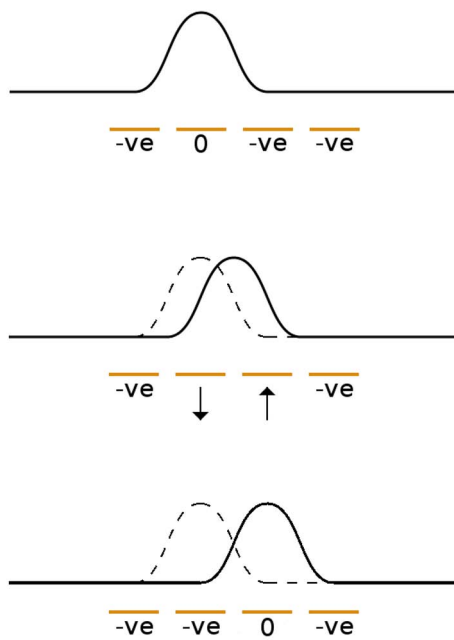


Figure 2.29: Schematic depiction of antiproton transfer from one electrode to an adjacent electrode. Arrows represent increasing (or decreasing) applied voltage.

distributions of positron and antiproton speeds begin to overlap. Eventually the antiprotons cool into the side wells and become axially separated from the positrons. The left well dump includes all antiprotons that have cooled into the left well, plus any that remain at a higher energy than the positrons. The right well dump contains only antiprotons that have been cooled. Both of these dumps are shown in figure 2.30. Synchrotron cooling of antiprotons is negligible over the timescales of a mixing sequence, so any that appear in the right well imply cooling through interaction with the positrons (or electrons - ineffective e-kicking can be identified by observing cooling in the absence of positrons, see section 3.4). The energy of the ejected antiprotons can be determined by correlating the time structure of the detector signal (see section 2.5.7) with the progress of the ramp (determined via sequencer time-stamps).

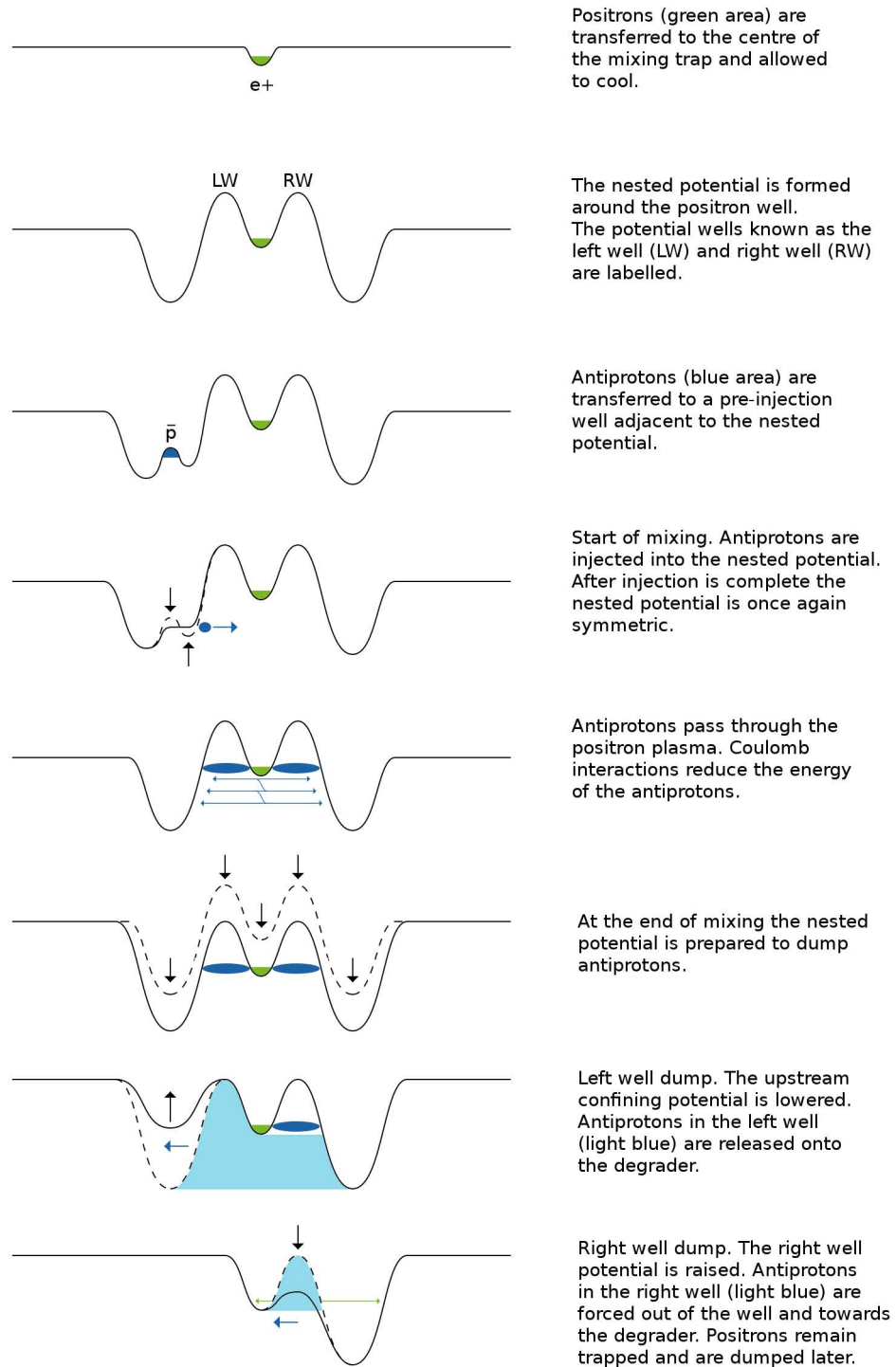


Figure 2.30: Schematic depiction, with commentary, of the mixing phase of a “standard mixing” sequence.

## Chapter 3

---

# Antiparticle Catching and Transfer and Antihydrogen Formation in the 2+1 T Solenoidal Field Configuration

---

The 2+1 T field configuration is the new configuration used in the ALPHA apparatus, consisting of a 1 T background solenoidal field (provided by the large bore main magnet) and an additional 2 T solenoidal field over the antiproton catching region (see section 2.5.4). In this chapter, results will be presented which demonstrate that positrons and antiprotons have been caught and transferred to the mixing region in the new field configuration without significant loss. It will further be demonstrated that antihydrogen formation has occurred at the reduced field which, as discussed in section 2.5.4, is necessary for the neutral trap.

### 3.1 Positrons

In a standard mixing cycle the positrons are collected in the positron accumulator before being transferred into the antiproton apparatus (see section 2.5.8 for a typical mixing cycle). The positron catching in the antiproton apparatus occurs downstream of the mixing region, i.e. in the 1 T solenoidal field region generated solely by the main magnet (and extending slightly into the fringe of that field). The mixing region is also at 1 T, such that when the positrons are moved to the mixing region they do not encounter the field gradient due to the 2+1 T configuration. Furthermore, there was no non-destructive method

of deducing positron plasma properties in the antiproton apparatus available at the time (such as measuring the electrostatic plasma modes to give information about plasma shape and density as in [77]). Thus initially, the only parameter of importance was the total number of positrons available for mixing after transfer into the mixing region, given the reduced (1 T instead of 3 T) solenoidal field.

This could be determined via a calibrated dump onto the Faraday cup (i.e. the final degrader foil) from the mixing region. Typically around 30 million positrons were available for mixing. Note that since the number of positrons is very much greater than the number of antiprotons (typically around a factor of 4000 larger), the number of positrons lost during mixing is very much smaller than the number initially available for mixing. This means that the number of positrons was virtually unchanged by mixing, so could be measured at the end of a mixing cycle.

## 3.2 Antiproton Catching

Several stages of optimisation were undertaken in order to maximise the number of  $\bar{p}$ 's caught. The beam from the AD was steered (section 3.2.1), the closing time for the high voltage used for catching was tuned (section 3.2.2), and the optimum position for the rotatable degrader was found (section 3.2.3). Furthermore, for comparison, data were taken for the number of  $\bar{p}$ 's caught at various settings of both high voltage and solenoid field strengths. These data will be presented at the end of this section.

For all these optimisation scans a “catch and hot-dump” sequence was used. In this sequence antiprotons were caught without electrons, held for a short time (of order 200 ms) and then dumped onto the degrader by disengaging the upstream high voltage. This procedure is known as a hot-dump. The annihilation products from the dump were detected by the external scintillators (see section 2.5.7) and this signal (along with the detector efficiency) used to determine the number of antiprotons present in the dump. The short hold was to ensure the signal generated by the dump was distinct from the scintillator afterglow caused by the antiprotons hitting the degrading material on injection into the apparatus. The hot-dump signal in this case represents the total number of “caught” antiprotons.

### 3.2.1 Beam Steering

Figure 3.1 shows the final elements in the extraction line from the AD to the ALPHA experimental area. The dipole magnet designated DE2.BHZ10 steers antiprotons from the extraction beamline common to all experiments

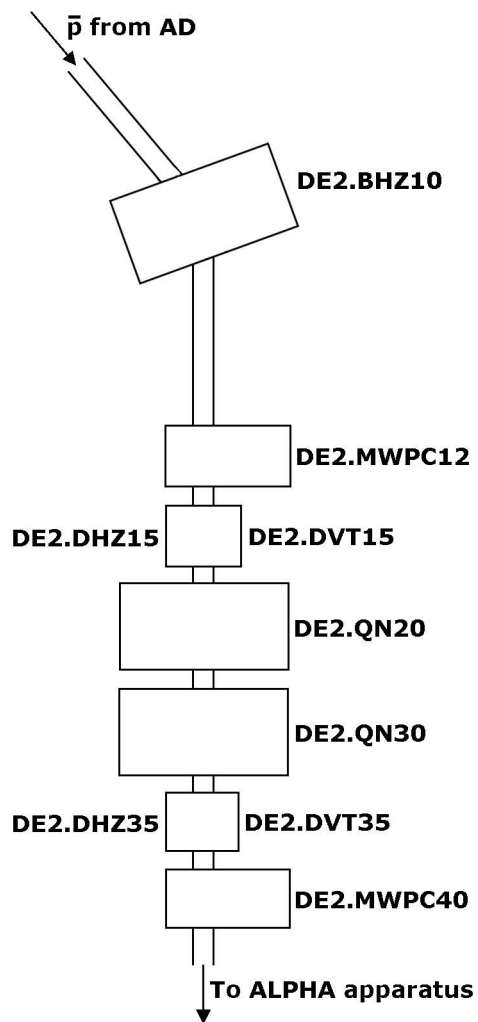


Figure 3.1: The AD extraction beamline into the ALPHA apparatus. Individual elements are described in the text.

towards the ALPHA apparatus. The beam then passes through a multi-wire proportional chamber (MWPC) designated DE2.MWPC12. There are several of these chambers in the extraction line. They contain a retractable screen of vertical and horizontal wires that register the passage of charged particles near the wires. The screens can be moved into the path of the antiprotons for use as a beam profile diagnostic (measuring beam position and size). However, antiprotons are stopped and annihilate within the screens, so in normal operation they are left out of the beam path. After MWPC12 the beam passes through a set of dipole steering magnets designated DE2.DHZ15 (acting horizontally) and DE2.DVT15 (acting vertically). It then passes through two quadrupole magnets designated DE2.QN20 and DE2.DN30. These two quadrupole magnets can together be used to focus the beam both horizontally and vertically. Finally the beam passes through another set of dipole magnets (DE2.DHZ35 and DE2.DVT35) and another MWPC (DE2.MWPC40) before passing into the ALPHA apparatus.

The AD operators tune all these elements (and others) so that the antiproton beam is centred on the final wire chamber. However due to slight (unmeasured) irregularities in the fringe fields of the ALPHA magnets this steering setting was typically not the optimum one for maximising the number of  $\bar{p}$ 's caught. The last two dipole magnets were used to tune the steering for the ALPHA apparatus, DE2.DHZ35 horizontally and DE2.DVT35 vertically.

Ideally the beam would have been focussed such that most of the beam would hit one pad of the beam counter (see section 2.5.7 for a description of the beam counter). The final dipoles could then be adjusted to maximise the percentage of the beam on the central pad, thus centring it (this was also the case in ATHENA, for example). This technique was used for initial steering with the rotatable degrader completely withdrawn from the beamline. However, due to the fact that the rotatable degrader and beam counter were further out of the solenoidal field than in the ATHENA apparatus, the focussing effect of the solenoidal field was reduced. For this reason, when the rotatable degrader was in use, the beam was more diffuse at the position of the beam counter. This meant that it was more difficult to meaningfully centre the beam using the beam counter. Instead, when using the rotatable degrader (see section 3.2.3 for tuning of the rotatable degrader), the number of  $\bar{p}$ 's caught was used as the figure of merit for the beam steering. Figure 3.2 shows the result of a typical steering scan.

Beam steering was performed regularly as changes in the AD and PS cycles, and also changes in the magnets of other experiments in the AD hall, could have an impact on the position of the beam inside the AD (and hence its position at extraction). Typically, over a few days, there would be a slight

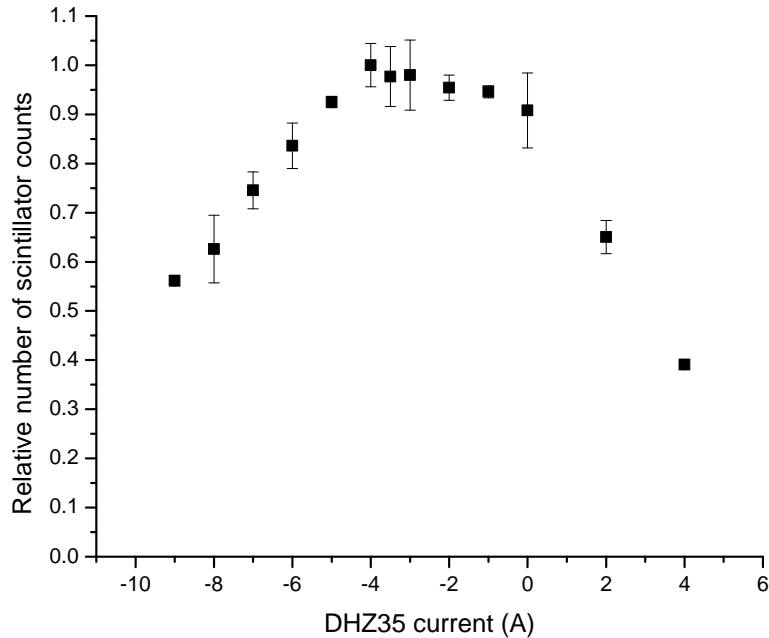


Figure 3.2: Scan of horizontal dipole current for magnet DHZ35 during run number 931 (22/10/06). The ordinate represents the external scintillator counts during the ‘hot-dump’ integration period. Uncertainties are comprised of counting statistics only (one standard deviation).

drift of AD magnets such that a short steering scan could increase caught  $\bar{p}$  numbers by around 10-15%. However, sometimes large changes would mean that the beam did not reach the ALPHA area at all, for example when the ATRAP collaboration ramped their main magnet from 5 T to 3 T. In these cases the AD operators would have to spend an hour or two re-steering the AD in several places to return the beam to ALPHA.

### 3.2.2 HV delay

As described in appendix A, the signal sent to the HV system to trigger the fast pulse used to catch the incoming antiprotons could be delayed by a variable delay module. The system was triggered by the AD pre-trigger (a signal sent from the AD control system). This signal could be set (by the AD operators) to arrive any time between a few tens of nanoseconds, to several seconds before the antiproton ejection (with a jitter of around 12 ns). The variable delay module in the HV trigger could also be varied over a large range (from 10 ns to several seconds, with a jitter of  $< 1$  ns). The HV could thus be triggered anywhere from several seconds before the antiproton ejection to

several seconds after (with a step size of as low as 10 ns). The delay module was initially set so that it could be adjusted to trigger the HV anywhere from  $\sim 200$  ns before the antiproton shot arrived to several seconds after it had traversed the trap and escaped. A scan was made to find the optimum delay setting. Again the number of  $\bar{p}$ 's caught is the figure of merit.

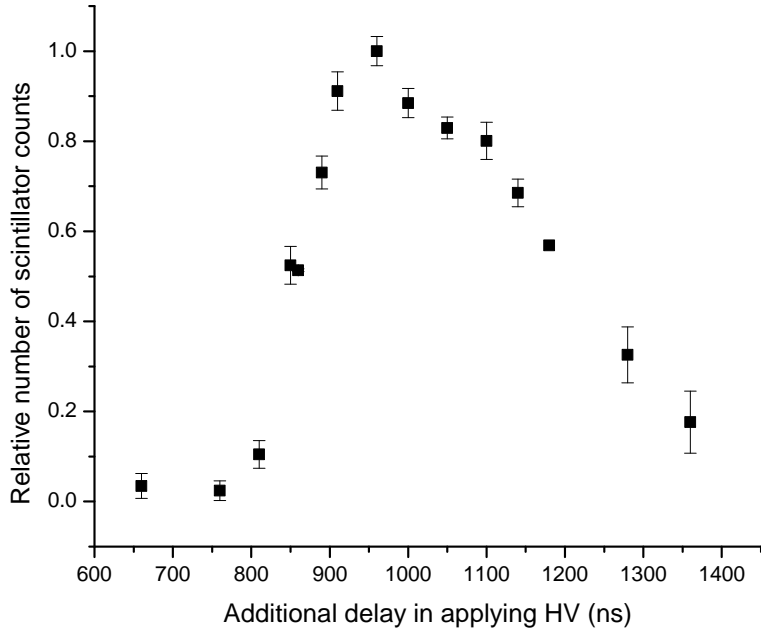


Figure 3.3: Optimisation of the delay in applying HV for antiproton trapping. Uncertainties are comprised of counting statistics (one standard deviation).

The sharp rise in caught  $\bar{p}$ 's shown in figure 3.3 shows that the bunch length of the shot ejected from the AD is around 150 ns. The time between the onset and termination of trapping gives a good indication of the effective trap length. In this case we use “trap length” to refer to the window of opportunity for trapping, i.e. the total time that the antiprotons spend in the region where they can be trapped (given no other applied forces). The FWHM of around 400 ns compares well with the expected trap length of 380 ns. Note that the delay quoted in the figure is the delay between the AD pre-trigger arriving at, and the HV trigger leaving, the logic system in the control room (as measured on an oscilloscope). It is not the total delay in applying the HV. However, since we only seek to maximise the number of caught  $\bar{p}$ 's, the absolute time delay is not important. A clear peak at 960 ns can be seen in figure 3.3 so a delay setting of 960 ns was chosen as optimal.

### 3.2.3 Rotatable Degrader

The degrading of antiprotons in the ATHENA apparatus was carefully analysed using a package known as SRIM [78]. The package is a Monte-Carlo based program that is used to calculate the passage of light ions through matter [79]. This analysis was used to simulate the degrading characteristics for catching with 5 kV blocking voltages, using a system of materials equivalent to the ATHENA system, and was found to be in good agreement with ATHENA experimental observations. The simulation was then used to design the degrading system for the ALPHA apparatus (necessarily similar to the ATHENA system). Careful consideration of thicknesses and axial positions of the various elements (rotatable degrader, beam counter, vacuum window and final degrader) allowed the use of a minimum of material in the rotatable degrader (thus minimising blow-up of the antiproton beam). The thickness of the foil used for the rotatable degrader was 18  $\mu\text{m}$ .

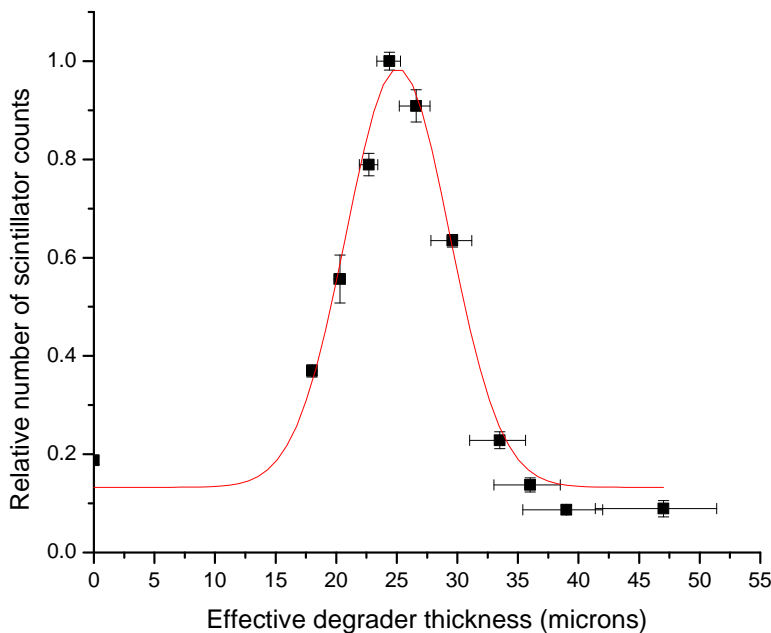


Figure 3.4: Degrading curve (see text for details). Uncertainties in the ordinate represent counting statistics only (one standard deviation). Uncertainties in the abscissa derive from the mechanical error in the rotation setting ( $\pm 2.5^\circ$ ) and thus are at a minimum when the foil is orthogonal to the beam (i.e. at its minimum thickness, in this case 18  $\mu\text{m}$ ). The data point at 0 thickness was acquired with the degrader foil completely removed from the beam path.

In order to determine the optimum position (and hence optimum effective

thickness) of the rotatable degrader, the number of trapped antiprotons was measured as a function of the effective thickness of the foil. This was done by recording the number of  $\bar{p}$  caught as the degrader was scanned over its range of movement. Figure 3.4 is the result of one such scan (taken during runs 1477-1488). The foil in this case was  $18 \mu\text{m}$  thick. The line in the figure is a Gaussian fit to the data, with a peak at  $25.09 \mu\text{m} (\pm 0.08)$ , and a FWHM of  $8.53 \mu\text{m} (\pm 0.17)$ . Thus the optimum effective thickness for this foil was approximately  $25.1 \mu\text{m}$ . The narrow width of the curve highlights the need for careful consideration of the total amount of degrading material. For instance, a difference of order  $10 \mu\text{m}$  could have led to a drastic reduction in the number of caught antiprotons.

### 3.2.4 Catching Voltage and Solenoidal Field Strengths

For comparison, data for the number of  $\bar{p}$ 's caught were taken for varying HV magnitudes and solenoidal field strengths. Figure 3.5 shows that the number of trapped  $\bar{p}$ 's is, within uncertainties, increasing linearly with trapping voltage. The number of  $\bar{p}$ 's also increases with total magnetic field, as illustrated in figure 3.6. This suggests that increased trapping voltage and increased solenoidal field in the trapping region could both lead to considerably more caught  $\bar{p}$ 's. Future iterations of the apparatus may try to exploit this.

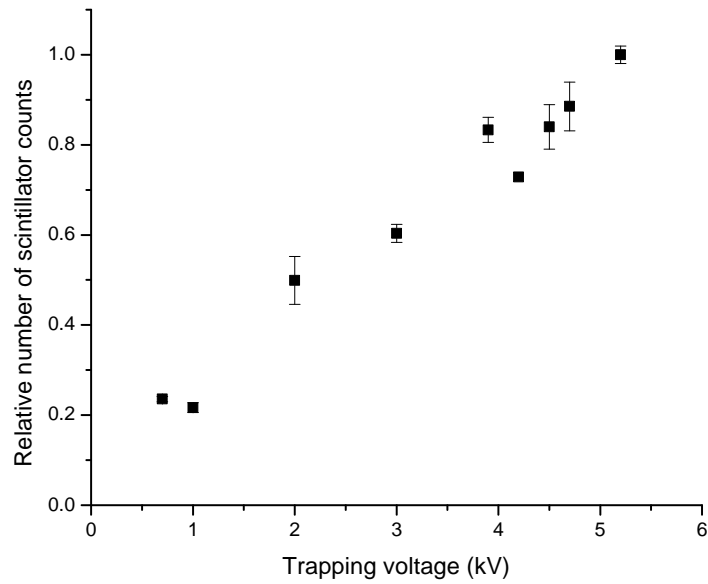


Figure 3.5: Effect of varying applied high voltage on the number of caught antiprotons.

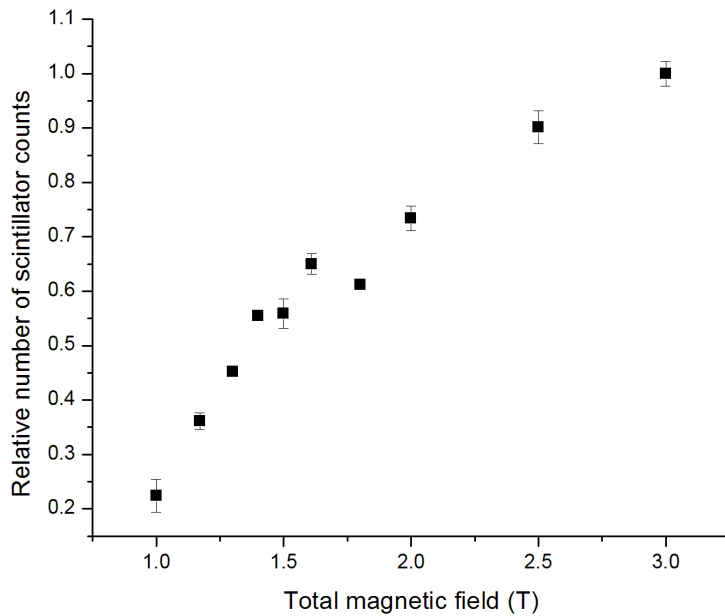


Figure 3.6: Effect of varying applied solenoidal field on the number of caught antiprotons.

### 3.3 Antiproton Cooling

Once the number of caught  $\bar{p}$ 's has been optimised the next stage was to optimise the electron cooling of them. For this investigation a “catch, cool and dump” sequence was used. In this sequence, before the shot of  $\bar{p}$ 's arrives, an electron plasma was loaded into a potential well in the catching trap. The electrons were produced by the electron gun described in section 2.5.5. Electron loading could be precisely controlled by raising a blocking potential between the gun and the trap until the emission from the gun was stable, then lowering the blocking potential for a set time to allow electrons to reach the trap. In this way typically around  $10^8$  electrons were loaded into the catching trap. Synchrotron cooling in the strong magnetic field reduced the temperature of these electrons to the trap temperature after a period of around a second.

Synchrotron cooling occurs because of the motion of the particles in the magnetic field. A moving charge in a magnetic field experiences a force perpendicular to both the direction of the field and the direction of motion, given by

$$\mathbf{F}_{\text{mag}} = q(\mathbf{v} \times \mathbf{B}),$$

where  $\mathbf{F}_{\text{mag}}$  is the force (in Newtons),  $q$  is the electric charge of the particle

(in Coulombs),  $\mathbf{v}$  is the instantaneous velocity of the particle (in  $\text{ms}^{-1}$ ),  $\mathbf{B}$  is the magnetic field (in Tesla) and  $\times$  is the vector cross product. This force is the magnetic component of the more general Lorentz force due to an electromagnetic field. The acceleration due to this force causes the particle to curve around the magnetic field lines. For a high enough field (or equivalently a low enough velocity) the particle will be trapped in a circular path around the field lines (this is how radial confinement is achieved in a Penning trap). The acceleration also causes the particle to emit electromagnetic radiation (known as Larmor radiation). This emission causes a recoil force (known as an Abraham-Lorentz force) which is directed opposite to the motion of the particle, thus reducing the speed and kinetic energy of the particle.

Next,  $\bar{p}$ 's were caught and allowed to interact with the electrons. During this time some of them would lose energy in Coulomb interactions with electrons and become trapped by the much lower potentials surrounding the electron well. After this interaction time was complete, the upstream high voltage was disengaged and the  $\bar{p}$ 's that had not cooled enough to be confined by the lower potential were released onto the degrader ("hot-dump"). After a short delay (to distinguish between the different signals) the electrode potentials were manipulated so that the blocking potential on one side of the well could be dropped and the cooled  $\bar{p}$ 's released onto the degrader (known as a "cold-dump"). Figure 3.7 is a schematic representation of a typical catch, cool and dump sequence.

Both hot and cold dumps were recorded as the interaction time was varied. These numbers, along with the total count (given by hot-dump + cold-dump), were plotted as a function of interaction time (e.g. figure 3.8). The total count is expected to remain constant, however at longer interaction times the total count begins to diminish. This is due to annihilations of  $\bar{p}$ s on residual gas molecules and also to radial transport of antiprotons due to interactions with electrons, forcing some  $\bar{p}$ s out of the potential well. Figure 3.8 represents a series of runs chosen to illustrate this fact, since the  $\bar{p}$  lifetime for these data was somewhat shorter than normal (see section 3.5 for a more typical lifetime with electrons). However, the exponential fit of the hot dump data in figure 3.8 is typical. It shows a decay with a characteristic time  $\tau$  of around 15 s, thus 40 s of cooling corresponds to around  $2.7\tau$  or around 93% of the antiprotons undergoing cooling. Thus after an interaction time of 40 s little increase in the number of cooled  $\bar{p}$  is observed, hence 40 s of cooling was identified as sufficient and this was used throughout the rest of the run.

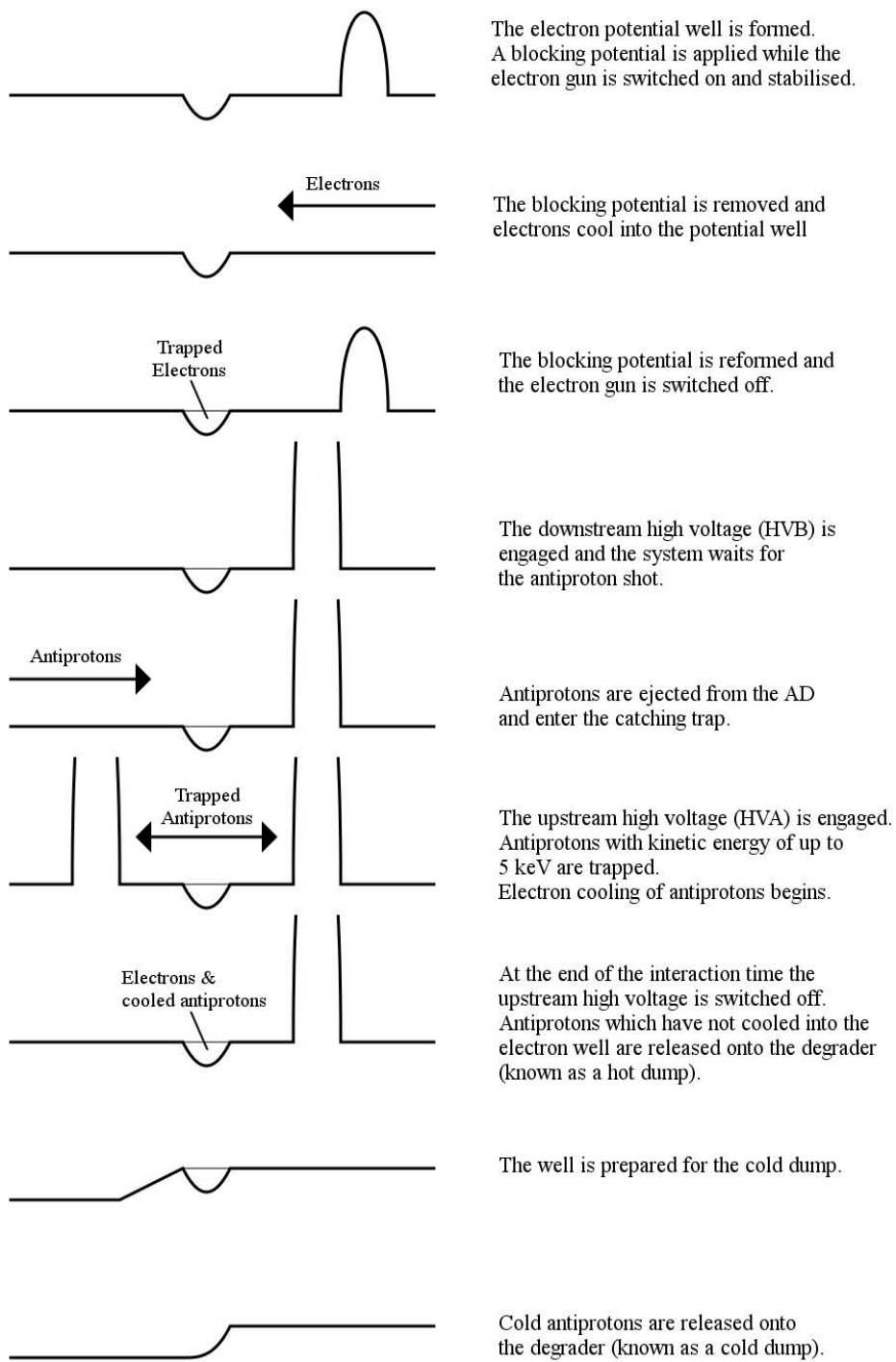


Figure 3.7: Schematic overview, with commentary, of a typical catch, cool and dump sequence.

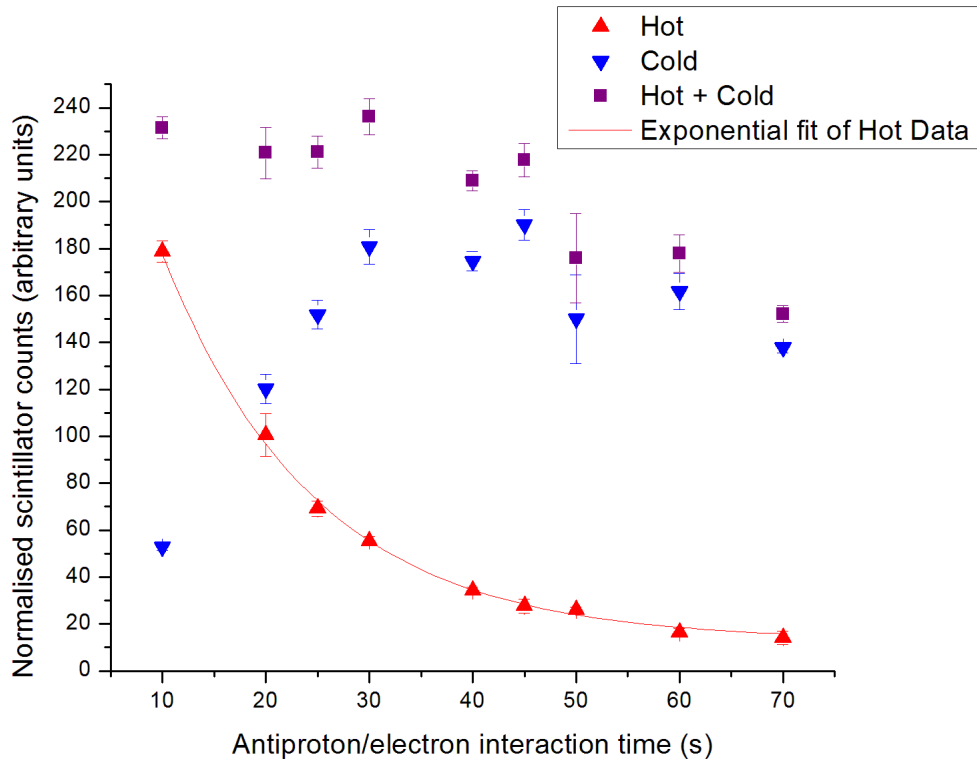
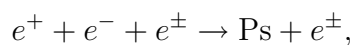


Figure 3.8: Cooling curve (values taken from runs 1111-1119). Hot and Cold dumps are shown, as well as their total (Hot+Cold). Uncertainties represent counting statistics (one standard deviation). The exponential fit of the hot dump data has a time constant of 14.7 ( $\pm 0.7$ ) seconds.

### 3.4 Electron Kicking

Electron kicking (or e-kicking) is the process by which the electrons that have been used for cooling the  $\bar{p}$ 's were removed from the potential well containing the  $\bar{p}$ 's. This must be done before mixing of  $\bar{p}$ 's with positrons because in the nested potential of the mixing well, the electrons quickly cool into the side wells. The antiprotons will then also cool into the side wells through interaction with them, leading to axial separation from the positrons in the centre of the nested potential, and thus prohibiting the interactions which result in the formation of antihydrogen. Electrons are also likely to form excited positronium (a bound state of an electron and a positron) via



leading to positron/electron annihilations, and/or transport out of the mixing region, thus depleting the number of positrons available for antihydrogen formation.

E-kicking works by exploiting the large mass difference between a  $\bar{p}$  and an electron. The velocity,  $v$ , of a particle can be found from

$$k_b T = \frac{mv^2}{2},$$

such that

$$v = \sqrt{\frac{2k_b T}{m}},$$

where  $k_b$  is Boltzmann's constant,  $T$  is the temperature of the particle and  $m$  its mass. The mass of an antiproton is approximately the same as that of a proton, around  $1.67 \times 10^{-27}$  kg. Electrons have a mass of around  $9.11 \times 10^{-31}$  kg, nearly 2000 times lighter. Their velocities at  $T = 4.2$  K are  $\sim 260$  ms $^{-1}$  for antiprotons and  $\sim 11000$  ms $^{-1}$  for electrons. This means that electrons traverse the approximately one electrode length of the cooling well ( $\sim 5$  cm) in around 4.5  $\mu$ s, whereas the antiprotons traverse the same distance in around 200  $\mu$ s, more than 40 times longer. If the confining potential is removed from one side of the cooling well, then the electrons will leave the well much faster than the antiprotons. If the potential is then raised back so that it once again confines the remaining particles, then a large number of electrons will have been removed with a much smaller number of antiprotons having escaped. This manipulation is known as an e-kick.

In practice, in order to maximise the number of  $\bar{p}$ 's left in the well but still ensure all electrons are removed, e-kicks are applied over a very short timescale (of the order of 200 ns) and repeated many times until all electrons are removed. This procedure is optimised by scanning over varying kick lengths, numbers of kicks and amplitude of kick (higher applied kick voltages mean a greater rate of change of the confining potential).

The electrons were kicked towards the degrader so that during the first few kicks a signal could be seen on the Faraday cup. The first kick could be used as a rough measure of the number of electrons loaded into the well by comparing it to similar electron loads dumped directly to the Faraday cup without interacting with  $\bar{p}$ 's. However, the Faraday cup could not be used to determine if all the electrons had been removed from the well. The number of electrons that would cause noticeable cooling of  $\bar{p}$ 's was much less than the number required to generate a measurable signal from the Faraday cup. This meant several stages of optimisation were required.

Initial e-kick optimisation was performed by measuring the signal on the Faraday cup for two e-kicks and then scanning over kick length, kick amplitude

and separation between kicks. These parameters were adjusted until settings were found where each e-kick gave a large loss of electrons for a negligible loss of antiprotons.

The next step was to determine the number of e-kicks required to remove (effectively all of) the remaining electrons. After the kicks had been applied the  $\bar{p}$ 's would be transferred to and injected into the mixing potential well just as in a normal mixing sequence, but without positrons present. Over the timescales used in the mixing sequence,  $\bar{p}$ 's would not undergo any measurable synchrotron cooling. Any  $\bar{p}$ 's present in the right well (see section 2.5.8 for a description of a typical mixing sequence and the significance of the right well) implied cooling of  $\bar{p}$ 's and hence, in the absence of positrons, also implied the presence of electrons. The number of e-kicks was increased until no measurable cooling of antiprotons occurred.

The parameters chosen were, 32 kicks of 140 V, 175 ns length and 100 ms separation.

### 3.5 Antiproton Stacking

In normal operation, the positron accumulator can provide a shot of positrons to the antiproton section of the apparatus once every 200 seconds. In that time the AD could have performed nearly 3 full cycles. In order not to waste antiprotons during a mixing cycle it was thus necessary to “stack” antiproton shots. Stacking was the term used to describe the procedure where a number of antiproton shots were caught and cooled before e-kicking and transfer took place. Stacking 3 antiproton shots meant that no antiprotons were wasted while waiting for the next transfer of positrons from the accumulator.

In a stacking sequence the first shot of the stack would be caught by the high voltage electrodes and cool into the electron well as normal. However, instead of interacting for only 40 s, the first shot would be held until the AD was about to eject the next shot. The upstream high voltage would be disengaged (giving a hot-dump) and then, instead of disengaging the downstream high voltage and proceeding to antiproton transfer, the next shot would be caught in the same way as normal (engaging the fast upstream high voltage in the same fashion as for a single shot). This would then be repeated another time to catch a third antiproton shot. This would be held for 40 s (cooling) and then hot-dumped and transferred to mixing.

The effect of stacking can be seen by cold-dumping onto the degrader instead of transferring to the mixing trap. Figure 3.9 shows the number of antiprotons in the cold dump after an increasing number of antiproton shots stacked. However, increasing the number of stacks cannot be used to arbitrarily increase the number of antiprotons available for a single mixing. The

limited lifetime of antiprotons in the presence of electrons means that the number which can be caught saturates. The linearity of the plot suggests a lifetime with electrons of better than 1200 s (the AD cycle during this set of measurements was around 100 s long).

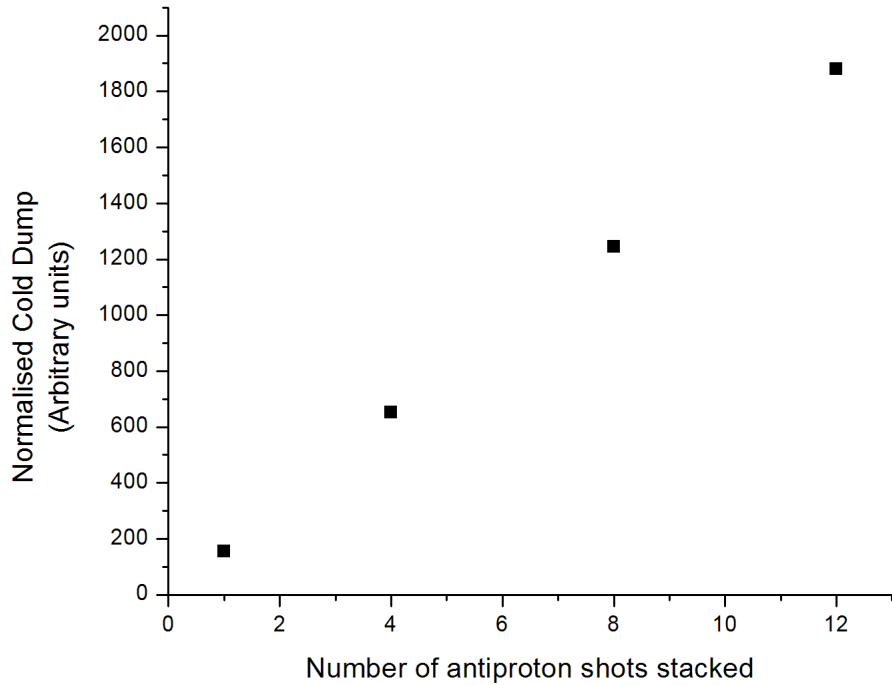


Figure 3.9: Effect of antiproton stacking on the number of antiprotons available for mixing.

As the number of antiprotons available increases linearly up to a large number of stacked shots, it may seem as though running with more stacks would provide an advantage (more antiprotons available for mixing means a higher rate of antihydrogen production). However due to the fact that each antiproton shot from the AD takes at least 80 s, large numbers of stacked shots greatly reduces the frequency with which it is possible to change experimental parameters, and to repeat measurements for statistical analysis. Both of these are important considerations and thus, in standard mixing, it is not considered prudent to stack more than the 3 shots necessary due to the duty cycle of the positron apparatus.

### 3.6 Antiproton Transfer

Antiproton transfer is the stage of a mixing sequence where cold antiprotons are moved from the catching trap into the mixing trap (as discussed in section 2.5.8). Each time the plasma was moved from one electrode to the next a series of time-stamps, one corresponding to each step of the ramping potential, was sent to the data acquisition system. The scintillator signals were thus synchronised with the sequencer time-stamps so that any  $\bar{p}$  loss during transfer could be correlated precisely to a particular potential manipulation. An example of this is shown in figure 3.10. This figure shows the response of the PMTs during an antiproton transfer. In this case each group of time-stamps shown in the lower plot represent a transfer from one two-electrode well, to an adjacent one. The first group (on the left) corresponds to transfer from electrodes 3&4, to electrodes 4&5, the following group from 4&5 to 5&6, and so on. Thus the antiproton loss evident in the upper plot begins in the transfer from electrodes 7&8 to 8&9 (E9 is the downstream high voltage electrode HVB).

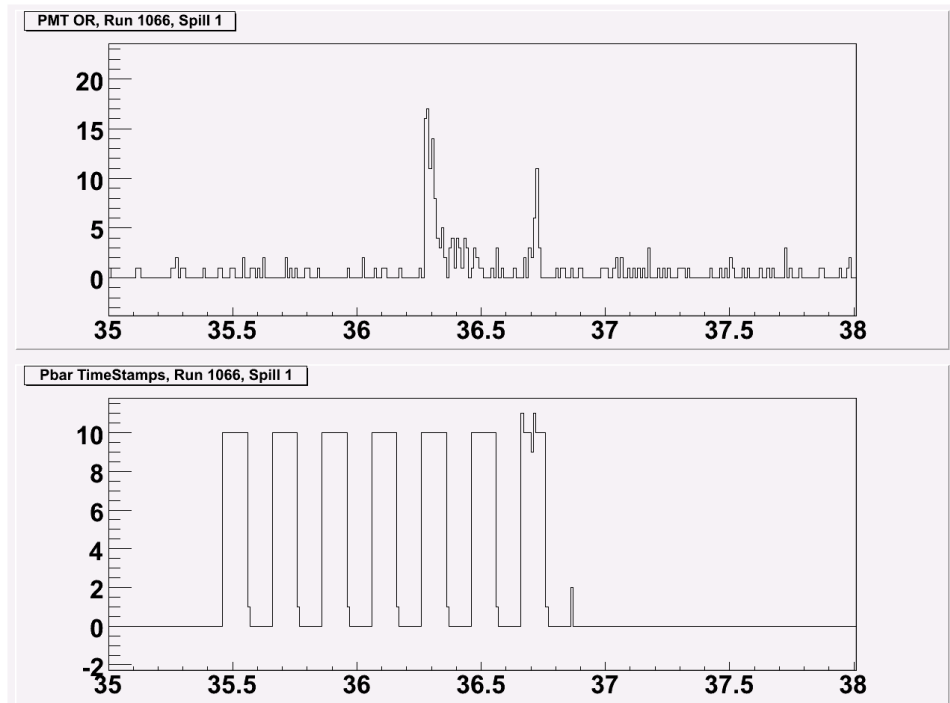


Figure 3.10: Histograms showing antiproton loss during transfer. The upper plot shows the response of the external scintillators (PMTs) during an antiproton transfer. The lower plot shows the time-stamps sent from the sequencer during the same period. The abscissa in each case shows the time (in seconds) since the start of the sequence, and is used to identify which sequence steps are represented by the recorded time-stamps. See text for details.

E-kicking could be applied in the catching trap, before the antiprotons were transferred, or in the mixing trap itself. Any manipulation of potentials used to move the antiprotons has the unavoidable consequence of increasing their energy, so it would seem most prudent to move them with electrons so that once the move was complete they would be able to cool again before the electrons were removed. However the 2+1 T field configuration complicates this somewhat. As the particles are moved from 3 T to 1 T the particle clouds expand in radius. The electron plasma is particularly susceptible to this. Furthermore as the electron plasma expands it draws the  $\bar{p}$  cloud with it. Thus as the particles move into the lower field region they will be drawn outward (reducing the particle densities), and some could be drawn to the electrode walls (where the  $\bar{p}$ 's will annihilate). For this reason e-kicks were typically performed in the catching trap (i.e. before transfer).

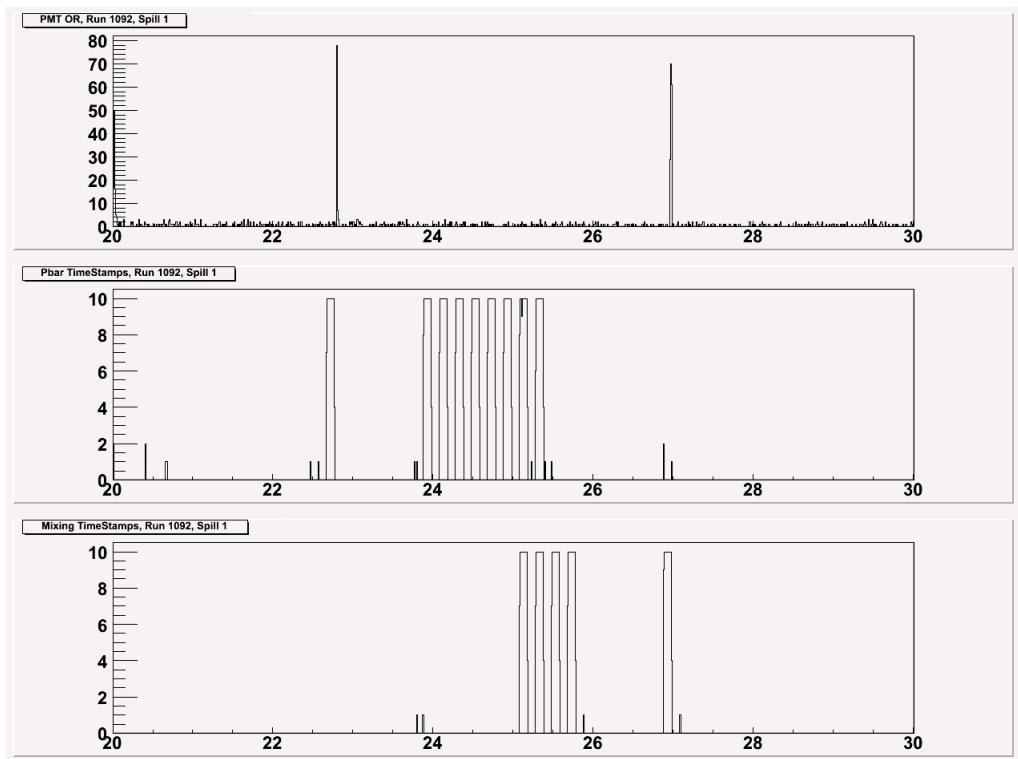


Figure 3.11: Histograms showing transfer without loss to a two electrode well in the mixing trap (electrodes E14 and E15). The lower two plots show sequencer time-stamps from both the  $\bar{p}$  and mixing sequencers during the transfer. The upper plot shows the external scintillator (PMT) response during the same period. The scintillator signal at around 23 seconds corresponds to the hot-dump, the one at around 27 seconds to the dump from the mixing trap after transfer. The abscissa shows the time (in seconds) since the start of the sequence.

Figure 3.11 demonstrates that it is possible to transfer  $\bar{p}$ 's from the 3 T

catching region to the 1 T mixing region without significant loss. The leftmost group of pbar time-stamps in the figure corresponds to the hot-dump, the rightmost group of mixing time-stamps to the dump from the mixing trap. No obvious loss can be seen in the external scintillator signal between these two dumps. The relative efficiency of the transfer can be calculated by comparing the number of  $\bar{p}$ 's dumped to the degrader from the catching trap after e-kicking, to the number dumped from the mixing region after transfer. After optimisation of the procedure, this transfer efficiency was typically better than 90%, such that transfer could be accomplished with less than 10% loss of  $\bar{p}$ 's. This is an important step in verifying that this configuration of fields is appropriate for trapping antihydrogen.

### 3.7 Antihydrogen Production at Reduced Field

The 2+1 T magnetic field configuration necessary for the antihydrogen trap results in a reduced solenoidal field (1T as compared to 3T in ATHENA and 5T in ATRAP) in the mixing region. One important consequence of this reduced field is that, due to the increased radius of the particle clouds, the positron and antiproton densities are reduced. Also, the positron synchrotron cooling time is longer by a factor of  $1/B^2$ , so the antiproton-positron dynamics will change on mixing. Thus it is necessary to demonstrate that antihydrogen formation is not prohibitively affected by these altered conditions.

The ATHENA experiment used position sensitive detection of antiproton and positron annihilation products as evidence of antihydrogen production. However, in subsequent experiments, experience with the device demonstrated that it was not necessary to rely on the position sensitive information to distinguish antihydrogen production from antiproton loss [25, 8, 27]. The trigger rate signal from the annihilation detector exhibits a time structure that, in concert with evidence of antiproton cooling, can be interpreted as a signature for antihydrogen production. Mixing with heated positrons (known as hot-mixing) leads to inefficient cooling of the antiprotons and inhibits antihydrogen production, and thus can serve as the null experiment. The heating is achieved by exciting the axial dipole mode of the positron plasma with a rotating electric field applied via a segmented electrode. Figure 3.12 shows the time evolution of triggers in the ATHENA annihilation detector. Of particular interest is figure 3.12(c). It clearly shows an increasing annihilation event signal, that peaks at around 100 ms and then tails off, and that is not present during hot-mixing. A similar time structure during mixing in the reduced solenoidal field, combined with evidence of antiproton cooling on positrons, would constitute sufficient evidence of antihydrogen formation.

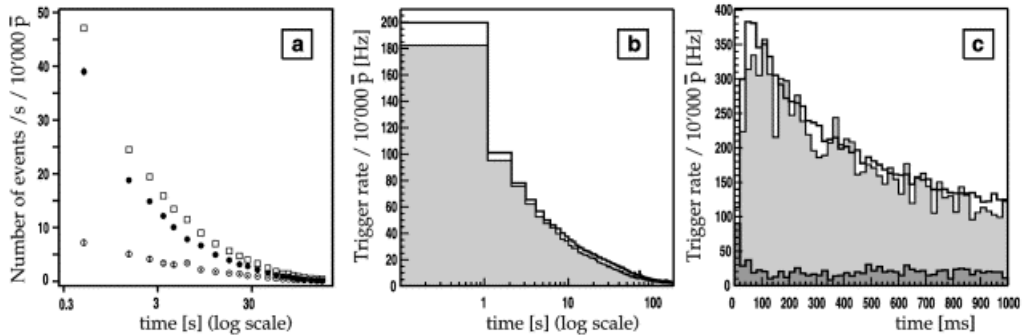


Figure 3.12: (a) Time evolution of events with reconstructed vertices for cold mixing data. The empty squares are the data, the full circles the contribution from anti-hydrogen annihilation, the empty circles the background (hot mixing) component; (b) time evolution of all triggers (full line) and of the detection efficiency-corrected events with reconstructed vertices (light shaded area) for cold mixing; (c) the first second of the same distributions; the dark shaded area is the trigger rate for hot mixing. Figure from [8].

The mixing sequence used for the following measurements involved stacking three antiproton shots, e-kicking and transferring to the pre-injection well (discussed in section 2.5.8) as optimised previously. Before antiproton transfer was completed, positrons were loaded into the nested potential and allowed to cool so that the nested potential was ready to receive antiprotons for mixing. The antiprotons would then be injected into the positrons. Typically around 7000 antiprotons would be injected into around 30 million positrons. The antiprotons were injected with a relative energy of around 12 eV and cooled through Coulomb interactions with the positrons (as previously observed in ATHENA [25] and ATRAP [80]).

The result of cooling can be observed by ramping down the trapping potential to determine at what energy the antiprotons are released. The confining potential upstream of the left well is ramped down, thus gradually dumping antiprotons onto the degrader. As the ramp proceeds, antiprotons with an energy greater than the confining potential are released and annihilate on the degrader and the products of these annihilations are detected by the external scintillators. Figure 3.13 shows the result of several such dumps, taken from mixing cycles in the 1 T solenoidal field. In plot (b) (mixing without positrons\*), antiprotons remain at their injection energy. In plot (c) (standard mixing, with positrons), antiprotons can be seen to have cooled to approximately the same energy as the positron plasma. In plot (d) (hot-mixing), some antiproton cooling has occurred, but it is clearly inefficient.

\*Mixing without positrons refers to a measurement cycle identical to mixing with positrons, but with positron transfer from the accumulator inhibited by a closed valve.

In ATHENA, the rise in event rate measured by the annihilation detector (shown in figure 3.12(c)), was correlated with the antiprotons cooling to the same energy as the positrons (i.e. as they reach the level shown in 3.13(c)). Together these plots demonstrate antiproton cooling on positrons at 1 T in the ALPHA apparatus.

The time evolution of the annihilation event rate during mixing in ALPHA was observed using the APDs (described in section 2.5.7). This evolution is illustrated in figure 3.14. The figure shows the event rate for both standard mixing, and hot-mixing. During standard mixing, an initial rise in event rate similar to that seen in ATHENA (figure 3.12(c)) can clearly be seen, albeit with a much slower rise time (of around 1 s). This slower rate is a result of the antiprotons taking longer to cool to a similar energy as the positrons, likely due to a reduction in the cooling efficiency because of the decreased positron plasma density in the 1 T field. The positron number is also lower, by a factor of 2 to 3, than in [8]. It can also be seen that mixing with heated positrons effectively suppresses this signal, thus demonstrating that the signal is not merely due to antiproton loss. The events in the first time bin in each case come from hot antiproton losses caused by the rapid potential manipulations used during the injection step (described in section 2.5.8).

The annihilation event rate shown in figure 3.14, coupled with the evidence for cooling shown in figure 3.13, can thus be interpreted as due to time-varying antihydrogen production, with a largely flat background (due to cosmic rays and slow and small antiproton losses). By comparing the number of antiprotons injected into mixing with the total number in the final antiproton dumps, we estimate that around 15% of the antiprotons could have produced antihydrogen. This number is consistent with the total number of events observed, given the estimated efficiency of the APDs, and it is comparable to that observed under typical conditions in ATHENA [8].

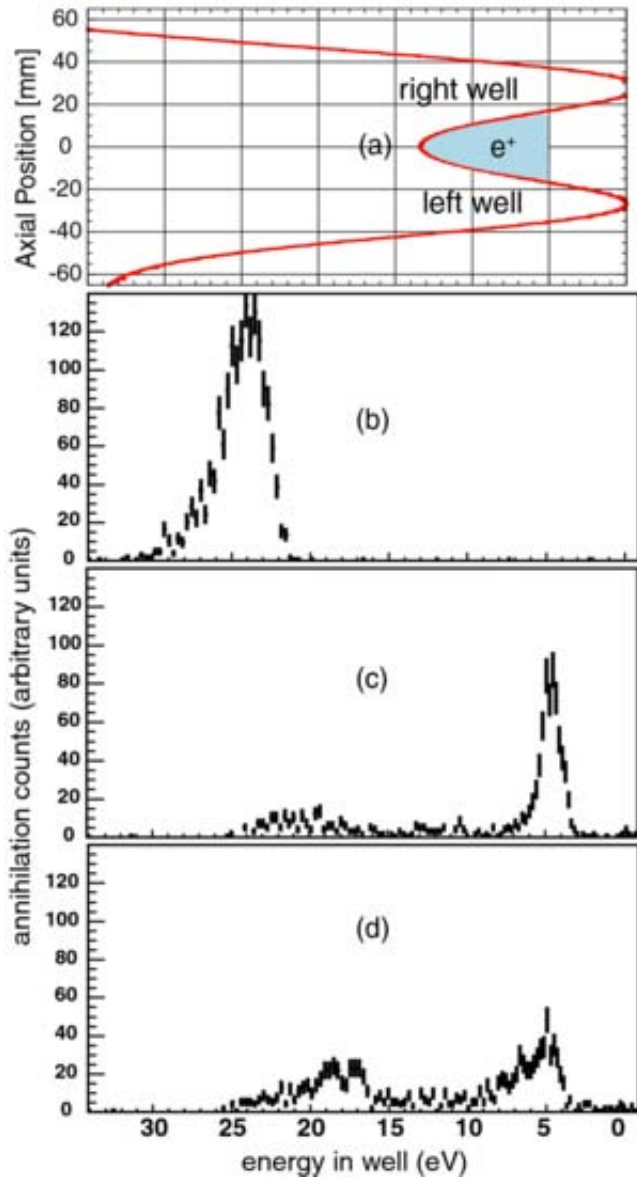


Figure 3.13: Antiproton cooling on positrons at 1 T in the ALPHA apparatus. Plot (a) shows the on-axis potential in the nested trap. Plots (b) to (d) show antiproton energy distributions in the nested trap, after 50 s of mixing, as measured by the external scintillators during the left well dump. In each case, the relative number of released antiprotons is plotted versus energy. Plot (b) is a mixing cycle without positrons (i.e. antiprotons only), plot (c) is a standard mixing cycle (i.e. with positrons), plot (d) is a hot-mixing cycle (i.e. with heated positrons). The horizontal axis scale is common to all four figures. The uncertainties reflect counting statistics only (1 standard deviation). Figure from [9].

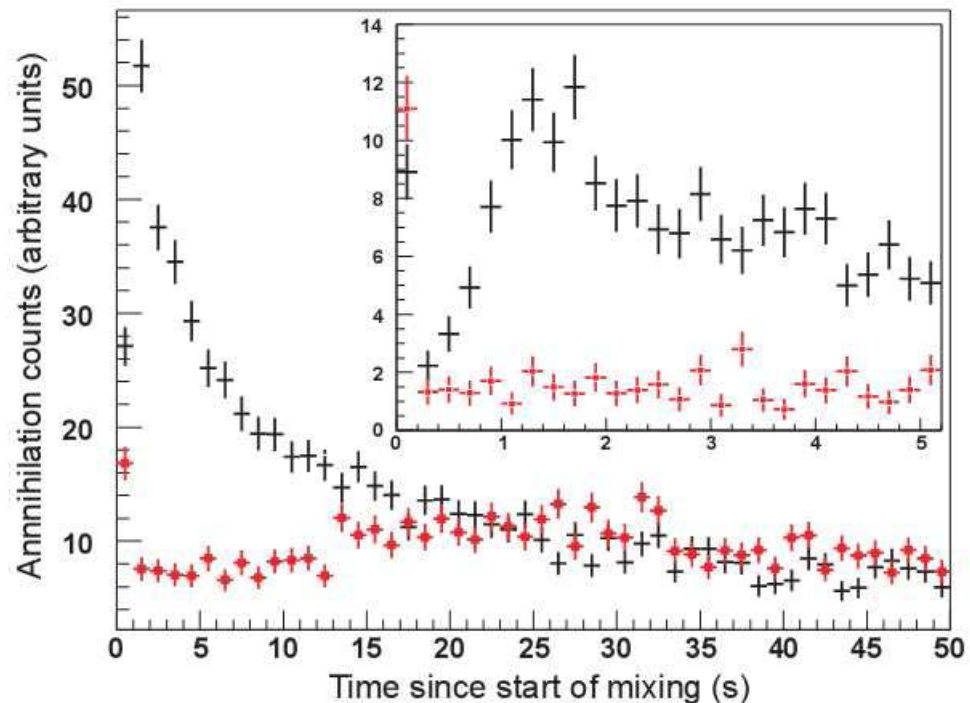


Figure 3.14: Annihilation events, as measured by the APDs, as a function of time after the start of mixing, for standard mixing (black) and hot-mixing (red). The time bins are 1 s long. The data are for 10 mixing cycles, normalized to one cycle. The inset is a plot of the first 5 s of the same data, re-binned into 200 ms bins to illustrate the rise time of the antihydrogen production. The uncertainties reflect counting statistics only (1 standard deviation). Figure from [9].

## Chapter 4

---

# Antiparticle Storage and Mixing in an Octupole Field

---

As discussed in section 2.5.4, the azimuthally asymmetric multipole fields of a neutral trap can sharply degrade the confinement of the charged particle plasmas used to synthesise antihydrogen. Experiments with a quadrupole magnet of similar construction to the octupole in the ALPHA apparatus indicated that quadrupole fields were not suitable for an antihydrogen trap because, for realistic field strengths, the quadrupole field leads to rapid loss of charged particles [68]. It is thus necessary to demonstrate that any losses caused by the octupole field do not prohibit the storage and manipulation of the charged particles or the formation of antihydrogen.

Two mechanisms were identified as responsible for loss when particles were injected into the asymmetric field. The first is an essentially immediate loss that occurs if a particle follows a field line that leads it to the Penning trap wall [68]. This “ballistic” loss should be much reduced for an octupole as compared to a quadrupole [81] because, for similar trap depths, the particles encounter a smaller field with the octupole. The ALPHA experiment is the first to attempt to observe this effect with antimatter plasmas. The second loss mechanism is through diffusive growth of the plasma due to the cylindrical asymmetry of the magnetic field [82]. This loss occurs over a much longer timescale than the ballistic loss.

The net magnetic field for ALPHA’s system of magnets is given in cylindrical coordinates  $(r, \theta, z)$  by

$$\mathbf{B} = B_z \hat{\mathbf{z}} + B_w \left( \frac{r}{R_w} \right)^3 \left[ \hat{\mathbf{r}} \cos(4\theta) - \hat{\theta} \sin(4\theta) \right] + \mathbf{B}_M(r, \theta, z)$$

where  $B_z$  is the solenoidal field,  $B_w$  is the octupole field at the trap wall,  $R_w$

is the trap wall radius, and  $\mathbf{B}_M(r, z)$  is the field from the mirror coils. For the following series of measurements the mirror coils were not energised; so we set  $\mathbf{B}_M = 0$ .

This net field means that the field lines originating from a circular locus of points in the plane transverse to  $\hat{\mathbf{z}}$  form four-fluted cylindrical surfaces; the flutes at each end are rotated by  $45^\circ$  with respect to each other. Figure 4.1 is an example of one such surface.

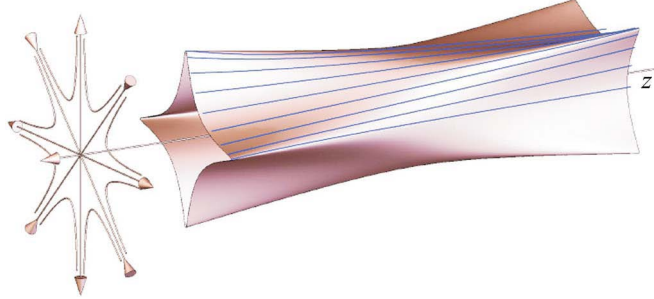


Figure 4.1: Net magnetic field from the octupole and main solenoid. The vectors on the left represent the directions of the axially invariant field from these coils. The surface is created by following the field lines from a radially centred circular locus; the lines shown within the surface are field lines.

It can be seen from figure 4.1 that the ballistic loss comes about because the magnetic field lines propagate outwards towards the trap walls. Particles following field lines that intersect the trap wall will annihilate. This loss is characterised by a critical radius  $r_c$ . For a given path length, field lines lying outside the critical radius at the trap centre will hit the wall, whilst those inside the critical radius will not. The field lines that propagate outwards most rapidly lie at certain azimuthal angles ( $\theta = 0, \pi/4, \pi/2, 3\pi/4$  etc.), and propagate outward like

$$r(z) = \frac{r_0}{\sqrt{1 - 2\frac{B_w}{B_z} \frac{r_0^2}{R_w^2} \frac{z}{R_w}}},$$

where  $r_0$  is the initial radius at  $z = 0$ . Thus the critical radius can be found from this equation by setting  $r_0 = r_c$ ,  $z = L_{eff}$  and  $r = R_w$ , where  $L_{eff}$  is the effective length of the trap. This relationship was investigated by several members of the ALPHA collaboration [83], who give the normalised critical radius as

$$\frac{r_c}{R_w} = \frac{1}{\sqrt{1 + \frac{B_w}{B_z} \frac{L}{R_w}}},$$

where  $L$  is the length of the trap. This is depicted in figure 4.2. It is clear that the longer the trap, and the stronger the octupole field, the smaller the critical radius. Note that the normalised critical radius does not get very small. This is because the octupole field, which scales as  $r^3/R_w^3$ , is very weak near the trap axis relative to its strength at the wall. For comparison, a quadrupole field would scale as  $r/R_w$  and consequently leads to a much smaller critical radius.

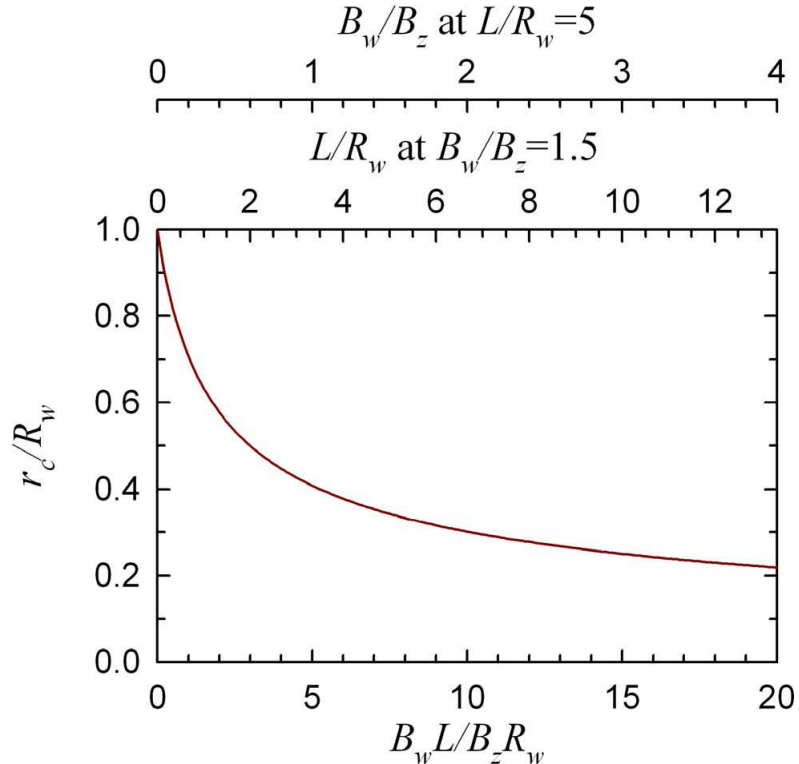


Figure 4.2: The normalised critical radius as a function of the octupole strength  $B_w$  and orbit length  $L$ . The alternate axes shown at the top isolate the dependance on each parameter while holding the other fixed at a typical value. Figure from [10].

The theoretical work by Fajans et al. [83] also demonstrated that, for an octupole, particle clouds would be subject to smaller deformation and have more uniform density when the particles were subject to a ramping field rather than when injected into a pre-existing field (although the particle loss would be similar). For this reason it was decided to operate by transferring particles to the mixing region before ramping the octupole. Thus the measurement sequence involved collecting particles (positrons or antiprotons) transferring them to the centre of the octupole (centre of the mixing region), ramping the octupole, holding the octupole at constant current for varying times, and then ramping down the octupole before dumping the remaining particles onto the final degrader.

Unfortunately, problems with the cryogenic system that was used to cool the neutral trap magnets and associated vapour-cooled leads meant that the octupole magnet could not be operated at its intended current (1100 A). Attempting to ramp faster than around  $30 \text{ As}^{-1}$ , or to a higher current than around 800 A, would trigger the quench protection system (before an actual quench could occur). In order to ensure the safe operation of the magnets, it was decided not to ramp the octupole at greater than  $20 \text{ As}^{-1}$ , and to limit the maximum operating current to 700 A.

## 4.1 Positron Storage

In order to investigate the effect of the octupole field on a stored positron plasma, positrons would be accumulated (using the same 300 s cycle as used during standard mixing), and then transferred to the centre of the mixing trap (i.e. the centre of the octupole). They were stored in a two electrode trap with an on-axis depth of around 49 eV. This potential was similar to the central well of the nested potential used in a standard mixing cycle. They were allowed to cool (by emission of cyclotron radiation) for around 30 s. The octupole was then ramped to 700 A (at  $20 \text{ As}^{-1}$ ), which produces a field of 1.2 T at the trap wall. It was held at constant current for varying times, and then ramped down at the same rate. After the ramp the positrons would be dumped onto the Faraday cup (final degrader) to determine the remaining charge. Two CsI detectors were placed near the apparatus at the degrader end and measured the gamma rays produced in the positron annihilations during the dump (giving an independent check of the relative number of positrons in the dump). Typically around  $3 \times 10^7$  positrons were loaded into the trap, with shot-to-shot variations of around 10%.

Measurement cycles with the octupole were alternated with identical cycles where the octupole was not ramped. Pairs of cycles could then be used to determine the fractional survival rate of particles when the octupole is energised. These data are plotted in figure 4.3. The times quoted in this figure include the time that the octupole is ramping, i.e. a time of 100 s in the plot represents 35 s ramping up, 30 s at maximum current, and 35 s ramping down. Each data point is the average of at least three identical pairs of field-on or field-off measurements. Within the shot-to-shot variations, no loss of positrons was observed without the octupole field, even at the longest times measured here. Note that, in the presence of the octupole field, little or no loss occurs on timescales relevant for antihydrogen production (of order 100 s), and loss does not exceed 40% at the longest times shown.

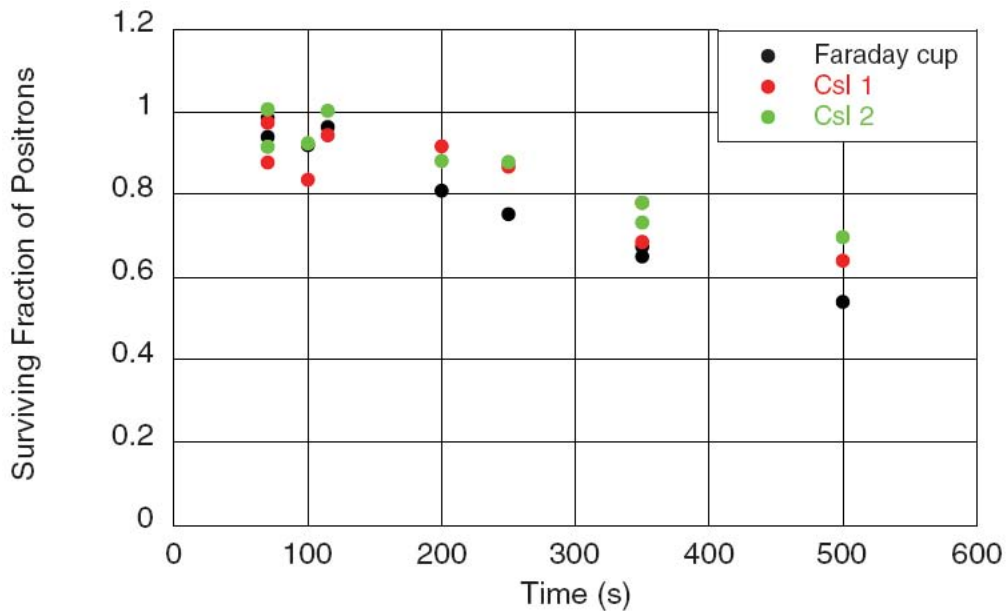


Figure 4.3: The ratio of the number of positrons stored in the octupole field to the number stored without the field is plotted versus holding time. Values were measured with the Faraday Cup and two CsI detectors. Error bars (typically  $\pm 10\%$ ) are omitted for clarity. Figure from [11].

## 4.2 Antiproton Storage

Antiprotons were caught, cooled and transferred to the mixing region as discussed in section 2.5.5, and optimised in section 3.2. At the end of the transfer, typically around 7000 antiprotons were stored in a single electrode trap with an on-axis depth of 43 eV. This well is similar to the pre-injection well discussed in section 2.5.8. This trapping potential, taken together with that of the positrons described in section 4.1, effectively simulates the situation immediately before particle mixing begins in a standard mixing cycle (as described in section 2.5.8).

The effect of the octupole field on the stored antiprotons was measured using a similar sequence to that used to investigate storage of positrons. The antiprotons were transferred to their storage well. The octupole was ramped up, held for varying times, and then ramped down again, using identical ramp parameters to the positron measurement. At the end of the ramp the antiprotons were dumped onto the degrader and the resulting annihilations were counted using the external scintillators (PMTs 1-4, described in section 2.5.7).

Figure 4.4 shows the measurement results. Once again, measurement cycles with the octupole were alternated with cycles without the octupole. Again, in the presence of the octupole field, little or no loss is observed at timescales

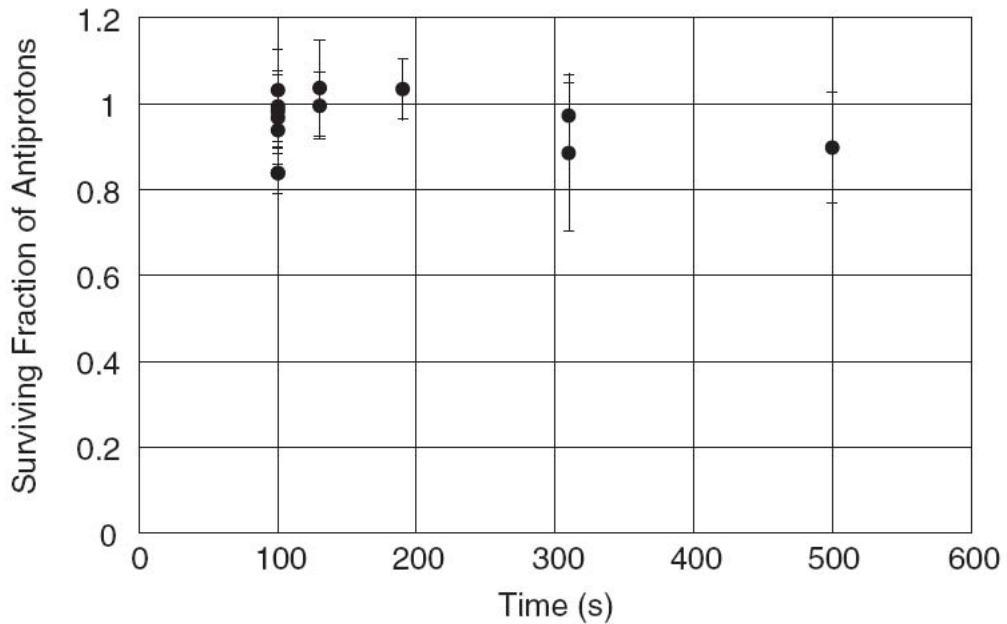


Figure 4.4: The ratio of the number of antiprotons stored in the octupole field to the number stored without the field is plotted versus holding time. Error bars are standard deviations for one set of measurements. Figure from [11].

relevant to antihydrogen formation. Losses at longer timescales were smaller than that of positrons, not exceeding  $\sim 20\%$ .

### 4.3 Antihydrogen Formation in the Octupole Field

In order to establish antihydrogen formation in the presence of an octupole field, it was necessary to attempt to provide similar evidence as that shown in section 3.7. Specifically, with an applied octupole field, demonstrate antiproton cooling in the presence of positrons that does not occur in their absence, then demonstrate an antiproton annihilation event signal that can be suppressed by mixing with heated positrons (similar to that shown in figure 3.14). However, this process was complicated by the addition of the octupole field. In the presence of the octupole field, the initial injection of antiprotons into the nested potential resulted in an immediate loss of particles. This loss increased with increasing octupole field, and was also found to be influenced by electron loading conditions (varying conditions of the electron plasma used to cool the caught antiprotons lead to a varying antiproton cloud radius). After optimisation of the nested potential and electron loading, the loss was minimised but remained substantial (shown in figure 4.5).

It can be seen in figure 4.5, that, at high octupole fields (high current), mixing cycles without positrons are subject to greater  $\bar{p}$  losses than cycles

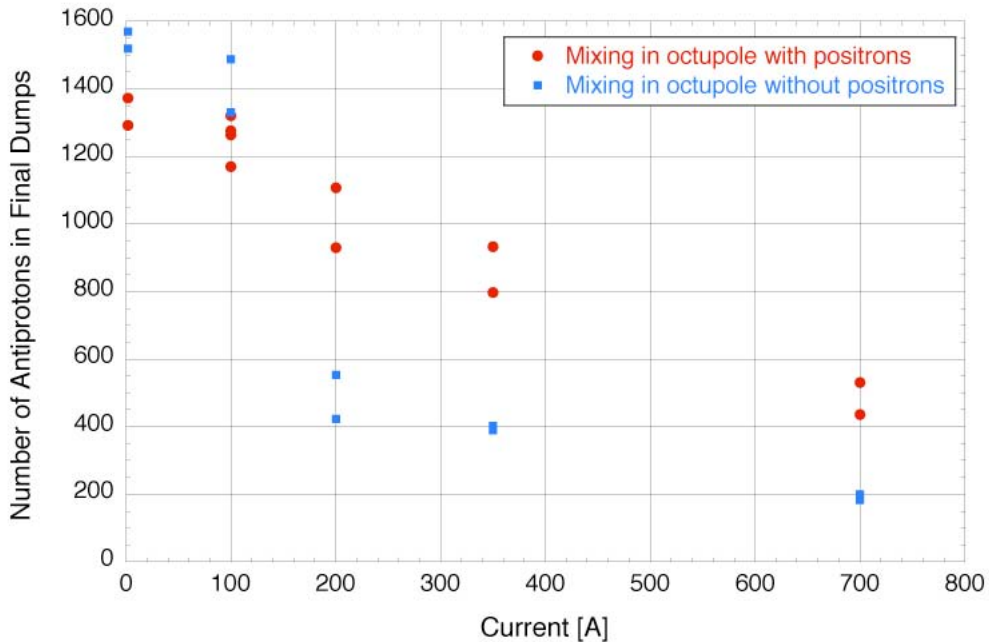


Figure 4.5: Antiproton survival during mixing in the octupole field. The ordinate represents the sum of the left and right dumps after mixing, normalised to the signal from HPD2, the abscissa represents the current in the octupole during mixing. The different data points in each series represent data collected during different runs, the variation seen is a symptom of unstable electron loading conditions.

with positrons. This is likely a result of the diffusive growth of the  $\bar{p}$  cloud to outside the critical radius (discussed earlier in this chapter) being slowed due to interaction with the positrons. At low octupole fields (low current) the critical radius is larger so this process has less of an impact. Instead  $\bar{p}$  loss due to antihydrogen formation dominates. Fluctuations in the number of surviving antiprotons shown in the figure are due to unstable electron loading conditions.

Figure 4.6 demonstrates positron cooling of antiprotons in the presence of the octupole field. Left and right dumps for two measurement cycles are shown. In each case mixing occurred with a current of 700 A in the octupole (equivalent to a field of 1.2 T at the trap wall). The histograms plotted in red correspond to the external scintillator signals during antiproton dumps for a mixing cycle without positrons (run number 2271), whilst those in black are for signals during dumps for a cycle with positrons (run number 2255). It can clearly be seen that in the case of mixing without positrons, antiprotons leave the left well early in the dump, and are not present in the right dump, i.e. they have not cooled from their injection energy. However, in the case of

mixing with positrons, antiprotons leave the left well later in the dump, and also appear in the right well dump. Thus cooling has occurred.

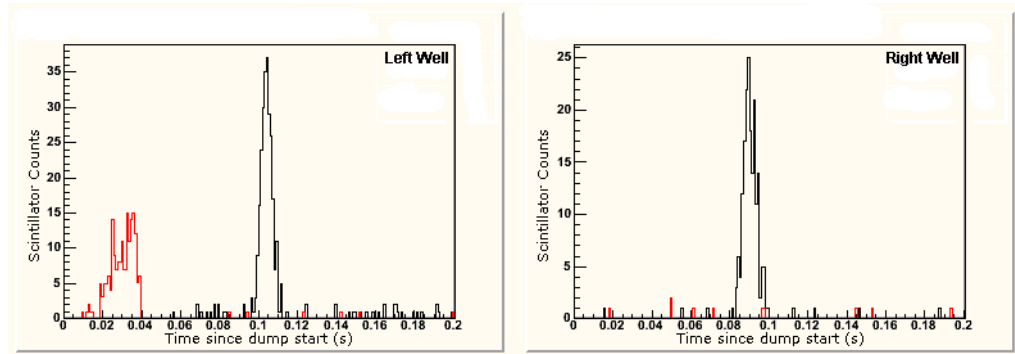


Figure 4.6: Positron cooling of antiprotons in the presence of the octupole field. Histograms show left and right well dumps for mixing cycles with positrons (run 2255 - black line) and without (run 2271 - red line). Plots show external scintillator (PMT) response over time (in seconds) during the dump integration window. The octupole was operating at a current of 700 A in each case. See text for details.

Figure 4.7 shows the signal, as measured by the APDs, during the mixing stage of each of the cycles used for figure 4.6 (runs 2255 and 2271). A large loss is evident in the first bin in each histogram, which corresponds to the immediate loss caused by the octupole field. A clear peak can be seen in the case of mixing with positrons (black line), that is not present when mixing without positrons (red line). However, this cannot be taken as evidence for antihydrogen formation, as opposed to merely antiproton loss, unless the signal can be suppressed by mixing with heated positrons.

Hot mixing in the octupole field was problematic. Positron heating at the level typically used during mixing without the octupole quickly led to the loss of virtually all stored antiprotons. During the period covered by this thesis, this could only be overcome by operating the octupole at a lower current. Consequently the series of measurements represented by figure 4.8 were taken with the octupole operating at a current of 100 A, for a field strength at the trap wall of around 0.17 T. However, it can be seen that the large loss resulting from the antiproton injection is still evident in the first bin of the plot. It can also clearly be seen that an annihilation signal starting at around 1 s in the case of cold mixing, is effectively suppressed during hot mixing. Combined with the evidence for antiproton cooling with positrons, this can be taken as evidence of antihydrogen formation.

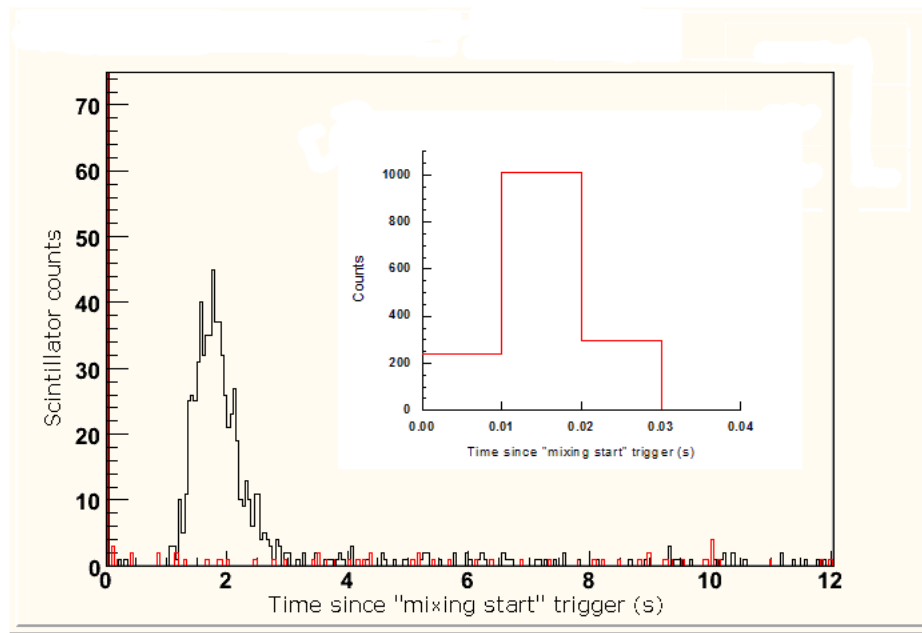


Figure 4.7: Mixing in the presence of the octupole field. The first 12 s of mixing for two different measurement cycles are shown, one with positrons (run 2255 - black line) and one without (run 2271 - red line). Plots show internal scintillator (APD) response over time (in seconds), beginning at the start of mixing. The octupole was operating at a current of 700 A in each case. The inset plot shows the first 0.04 s of the run 2271 data, it illustrates the large loss contained within the first time bin of the main plot (run 2255 has a similar though slightly reduced loss).

#### 4.4 A First Attempt to Trap Antihydrogen

The development of the apparatus during the period covered by this thesis did not reach the point where an antihydrogen trapping experiment could be considered until near the end of the 2006 AD beam time. Consequently, there was limited time available to collect antihydrogen trapping data. Further, the anticipated event rate for trapped antihydrogen was only marginally higher than the expected background rate. Hence a great number of mixing cycles would have been necessary to identify a statistically significant signal. However, a trapping experiment was developed and attempted.

The sequence used involved collecting positrons and antiprotons, and transferring them to the nested potential as in a standard mixing sequence. The octupole would then be ramped to 700 A and the mirror coils to 530 A. The mirrors operated at the reduced current of 530 A (as opposed to their design current of 750 A) so that they undergo an equivalent reduction in field as that imposed upon the octupole due to the problems in the cryogenic system (referred to earlier). The antiprotons would then be injected into the nested

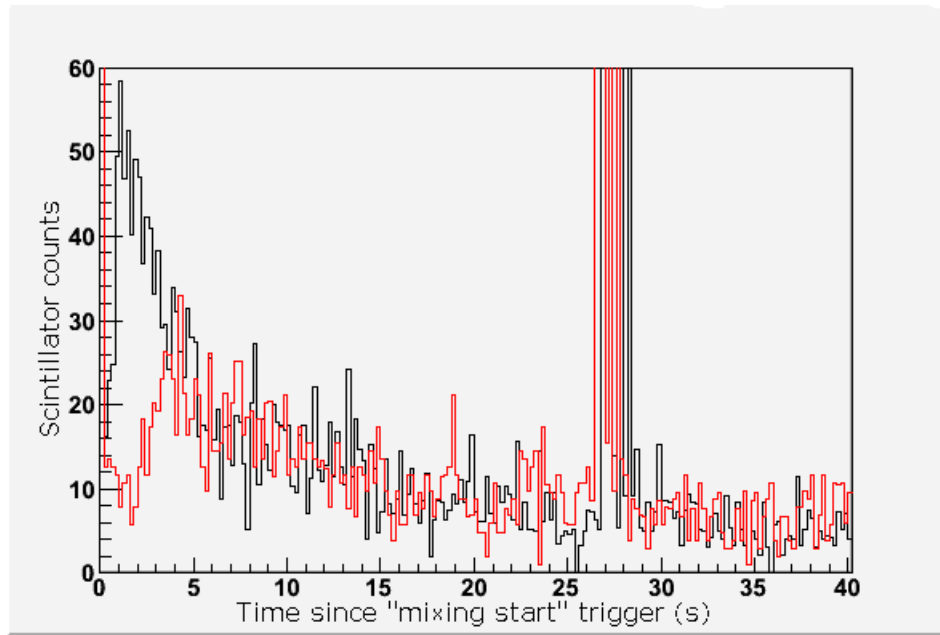


Figure 4.8: Evidence for antihydrogen formation in the presence of the octupole field. Antiproton annihilation event rate is plotted over time (in seconds) during mixing as measured by the internal scintillators (APDs). The black line represents the normalised sum of 5 cold mixing results over 4 runs, the red line represents the normalised sum of 5 hot mixing results over 4 runs. The large peak at around 27 seconds is the result of the high energy collision of protons with the iridium target at AD injection. The shower of particles created in this collision causes a response in every scintillator in the AD hall. In later years a system was implemented to remove this feature from acquired data by inhibiting the injection phase of the AD cycle.

potential and allowed to mix for varying times. In order to maximise the number of repetitions possible, this mixing time was typically restricted to between 2-6 s. This is acceptable as it can be seen in other mixing cycles that antihydrogen formation in the ALPHA apparatus typically peaks between 1 and 3 seconds after the start of mixing, and drops to near background after around 6 seconds. However, a few longer mixings were undertaken as a test. Once mixing was complete, the nested trap would be emptied of charged particles by dumping to the degrader and grounding the trap electrodes. After this, any remaining particles could only be confined by the magnetic trap. The octupole would then be induced to quench. The current in the octupole would be reduced by one half after 10 ms, so the APD signal for 20 ms after the quench was taken as the “quench dump” integration window.

In all 30 trapping cycles were attempted. The APD background during this series of measurements was about 2.6 Hz, so we expect to see  $2.6 \text{ Hz} \times$

$30 \text{ mixings} \times 20 \text{ ms} = 1.64 \text{ counts}$ . Only 2 counts were observed, which is compatible with background.



## Chapter 5

---

# Conclusions and Prospects

---

This thesis has detailed the development and commissioning of the ALPHA antihydrogen trapping apparatus. It began by discussing the history of antimatter physics that led to and enabled the design of the apparatus. It has discussed the importance of antihydrogen trapping in testing one of the basic assumptions of the Standard Model of particle physics. It has gone on to discuss the design and construction of the apparatus. Finally, it has presented results that demonstrate antihydrogen formation in the new magnetic field configurations that together constitute a magnetic minimum trap for neutral antihydrogen. This is an important preliminary result for any antihydrogen trapping apparatus, and confirms that the ALPHA apparatus does present a potential route towards laser spectroscopy of antihydrogen.

Another conclusion that can be drawn from the 2006 beam time is that limiting the loss of particles that occurs on antiproton injection at the start of mixing, is vital to any attempt to trap antihydrogen. This loss was the subject of a great deal of investigation, eventually leading to a novel radial diagnostic where the outer radial profile of the antiproton cloud could be studied by observing the time structure of the loss as the octupole field was increased [10]. Ultimately, the only way to reduce the loss was to reduce the radius of the antiproton cloud before injection. However, control of the radial profile of the trapped antiproton cloud was difficult, and was not achieved during the 2006 beam time. Indeed, much of the 2007 antiproton beam time was devoted to investigating how such control could be achieved. That work is not within the scope of this thesis, however a short discussion is included here.

In order to investigate radial control of the antiproton cloud, it was first necessary to be able to observe the radial profile. The diagnostic developed using the octupole was useful for measuring the outer profile, but clearly could not measure the profile within the critical radius at the maximum operating

current of the octupole. However, this requirement to accurately measure the radial profile was anticipated. The same movable armature (described in section 2.5.5) that carried the electron gun and positron transfer electrode also included a microchannel plate (MCP) and phosphor screen assembly. The MCP is a device consisting of two plates of highly resistive material. Each plate has a regular array of microscopic tubes (or channels) connecting one side to the other. The channels are at an angle of  $45^\circ$  to the plate surface, and the plates are rotated and placed together so that the channels meet at right angles (as in figure 5.1). This means that any particle entering a channel is guaranteed to hit the channel wall at some point. The plates are biased to a high voltage so that when a particle hits the wall of a channel electrons are released via secondary emission. These go on to release more electrons as in figure 5.1. Eventually a large number of electrons exit the second plate and are accelerated towards the positively biased phosphor screen. When the shower of electrons hits the phosphor screen they cause the screen to fluoresce photons. These are emitted both in front of and behind the screen. The photons that are emitted to the rear of the screen strike a mirror which reflects them out of the apparatus via a vacuum window (a crystal window mounted in a vacuum flange). The response of the phosphor screen was then measured by taking an image with a CCD camera (this camera was not available during the 2006 beam time).

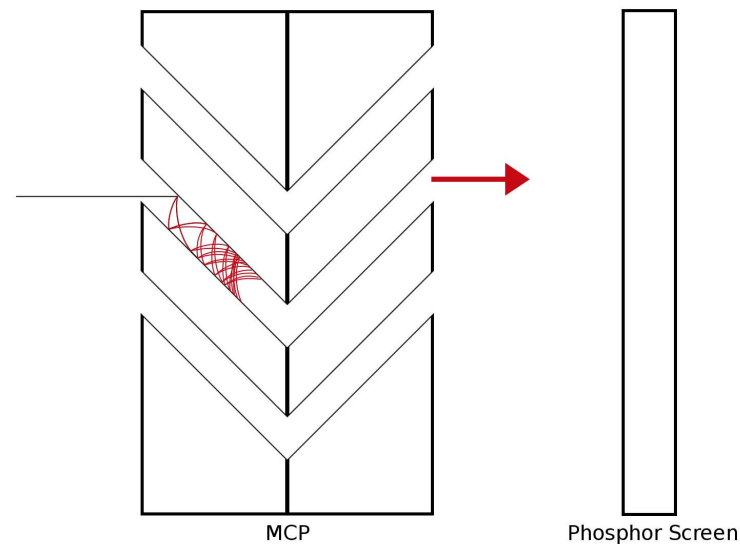


Figure 5.1: Schematic representation of the MCP and phosphor screen. Particles entering the MCP on the left produce a shower of electrons (shown in red) which exit the right of the MCP and are accelerated towards the phosphor screen.

The MCP assembly made it possible to observe the inner radial profile of

the antiproton cloud (the area that could not be observed by the octupole diagnostic). Particles dumped onto the MCP would produce images such as those shown in figure 5.2. The hard edges visible in the images are present because the solenoidal field drops from 3 T in the trapping region, to only 0.024 T at the position of the MCP (shown in figure 5.3). Thus the field lines, and hence the particles, expand by a factor of  $\sqrt{3/0.024} = 11.2$ . The particles must pass through several apertures in the apparatus on their way to the MCP, thus only particles that follow field lines that do not intersect with material surrounding the apertures can proceed to the MCP. The significant apertures in this iteration of the apparatus (used during the 2007 AD beam time) are indicated in figure 5.3. One was a small cylinder, upon the end of which was mounted a remotely movable flap that could be closed to prevent electromagnetic radiation entering (and heating) the trapping volume. This cylinder was located at approximately 800 mm from the centre of the octupole. The other was the end of the transfer electrode closest to the MCP.

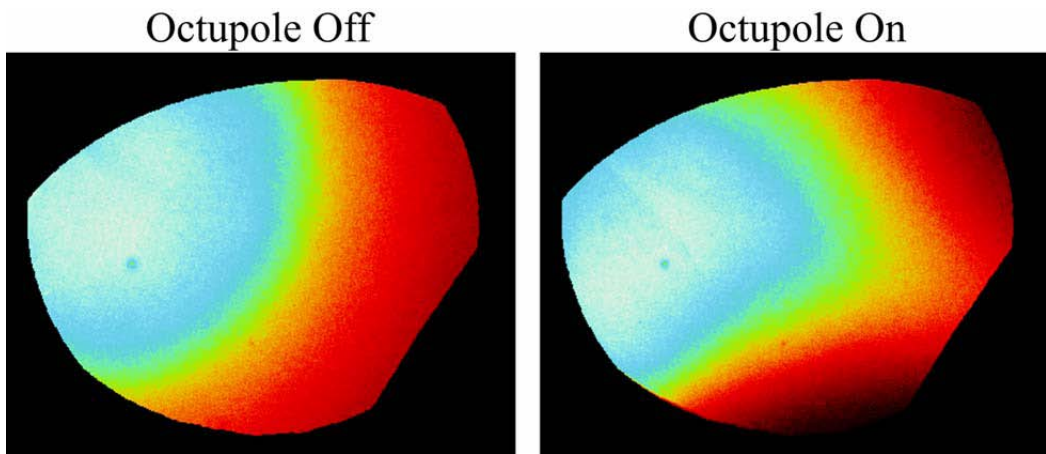


Figure 5.2: Two typical images acquired with the MCP/phosphor screen assembly. These images were generated by passing a circular electron plasma through the octupole, with the octupole off and on. Apertures (discussed in the text) form the image boundaries and limit the image to one quadrant of the octupole field map. The distortion evident in the right-hand image corresponds to one flute of the magnetic surface shown in figure 4.1.

The images from the MCP assembly were used to investigate radial compression of particle plasmas using a rotating wall technique similar to that used in the positron accumulator (section 2.4.2). First, electron plasmas similar to those used to cool antiprotons after catching, were loaded into the catching region and subjected to rotating wall fields of varying amplitudes and for varying times. The electrons would then be dumped onto the MCP and an image acquired. This procedure was tuned until settings that provided

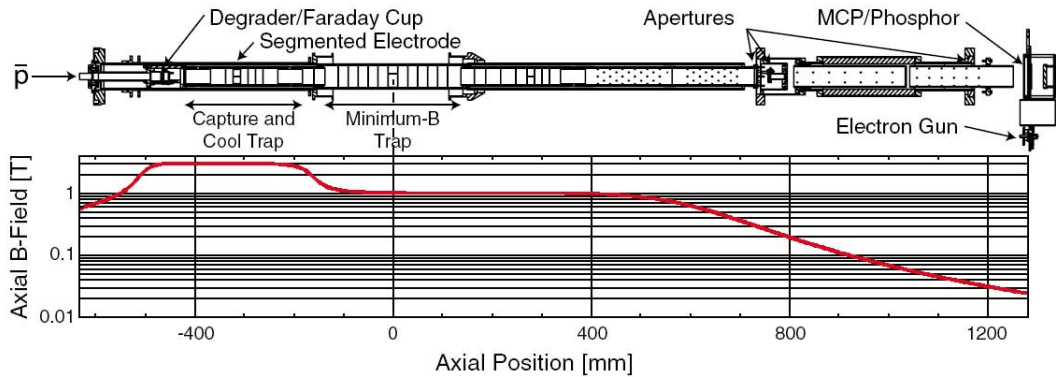


Figure 5.3: Schematic diagram of the ALPHA apparatus that shows the position of the MCP/phosphor assembly, and also the positions of the apertures apparent in the generated images (see text for details). The graph below the schematic plots the axial magnetic field. Figure from [12].

clear evidence of compression was obtained. Antiprotons however, were not present in large enough quantities to produce a significant radial electric field such that the rotating wall technique could be applied directly. Instead, antiprotons were caught and cooled as in a standard mixing cycle. The rotating wall was then applied to the electron plasma that had been used to cool the antiprotons. After the application of the rotating wall, the electrons would be removed with a standard e-kicking procedure, and the antiprotons would be dumped onto the MCP and an image acquired.

Figure 5.4 shows the result of compression of both electron plasmas and antiproton clouds as described earlier. The difference between the images of electrons and antiprotons come about because the two particle species are affected by the changing magnetic field in different ways. The electrons are tightly bound to the field lines and follow them closely, however the heavier antiprotons do not follow the field lines, but rotate around the magnetic axis due to centrifugal drift [84]. Because of this drift, and the fact that the traps magnetic and mechanical axes are not perfectly aligned, the apertures are imaged differently for the two particle species. Hence the image centres for positrons and antiprotons are not coincident, and the apertures limit the image areas differently.

The image brightness was calibrated by independently measuring the charge with the Faraday cup (for electrons) and the response of the external scintillators (for antiprotons). The calibrations are accurate to about 20%. Analysis of the scintillator response during e-kicking and application of the rotating wall verifies that no antiprotons were lost at those times. This technique was used to produce antiproton density increases of as much as a factor of 10 and clouds of radii as small as 0.29 mm. It should lead to a considerable increase

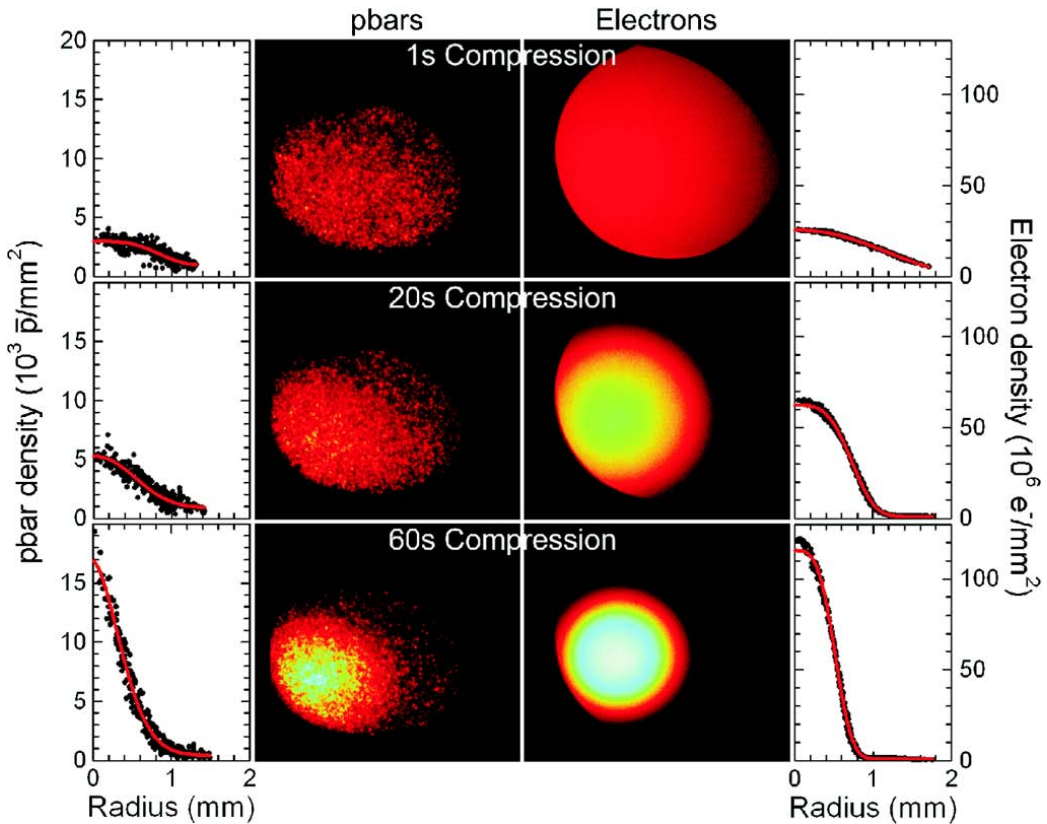


Figure 5.4: Antiproton and electron images showing the effects of the rotating wall, and the resulting radial profiles. Figure from [12].

in the number of antiprotons that survive injection into the nested potential, and hence an increased number of antihydrogen atoms available for trapping. This work is currently still ongoing.

The ALPHA collaboration continues to work towards antihydrogen trapping and spectroscopy. The 2008 AD beam time has seen the installation and commissioning of the custom built position-sensitive annihilation detector. The work presented in this thesis, and the techniques perfected during that time, were a necessary part of the development of the apparatus and form the basis for the continuing experiments.



---

# Bibliography

---

- [1] C. D. Anderson. The Positive Electron. *Phys. Rev.*, **43**:491, (1933). [cited at p. iv, 2, 3]
- [2] G. Baur, G. Boero, A. Brauksiepe, A. Buzzo, W. Eyrich, R. Geyer, D. Grzonka, J. Hauffe, K. Kilian, M. LoVetere, M. Macri, M. Moosburger, R. Nellen, W. Oelert, S. Passaggio, A. Pozzo, K. Rhrich, K. Sachs, G. Schepers, T. Sefzick, R. S. Simon, R. Stratmann, F. Stinzing and M. Wolke. Production of Antihydrogen. *Phys. Lett. B*, **368**:251, (1996). [cited at p. iv, 3, 4]
- [3] D. P. van der Werf, L. V. Jørgensen, T. L. Watson, M. Charlton, M. J. T. Collier, M. Doser, and R. Funakoshi. The ATHENA positron accumulator. *Applied Surface Science*, **194**:312, (2002). [cited at p. iv, 19]
- [4] M. Amoretti, C. Amsler, G. Bonomi, A. Bouchta, P. Bowe, C. Carraro, C. L. Cesar, M. Charlton, M. J. T. Collier, M. Doser, V. Filippini, K. S. Fine, A. Fontana, M. C. Fujiwara, R. Funakoshi, P. Genova, J. S. Hangst, R. S. Hayano, M. H. Holzscheiter, L. V. Jørgensen, V. Lagomarsino, R. Landua, and D. Lindelöf Production and Detection of Cold Antihydrogen Atoms. [cited at p. iv, v, 5, 7, 23, 24, 25]
- [5] M. H. Holzscheiter, M. Charlton, and M. M. Nieto. The route to ultra-low energy antihydrogen. *Phys. Rep.*, **402**:1, (2004). [cited at p. v, 25, 27]
- [6] Supercon, Inc., 830 Boston Turnpike, Shrewsbury, MA 01545. [cited at p. v, 30]
- [7] W. Bertsche, A. Boston, P.D. Bowe, C.L. Cesar, S. Chapman, M. Charlton, M. Chartier, A. Deutsch, J. Fajans, M.C. Fujiwara, R. Funakoshi, K. Gomberoff, J.S. Hangst, R.S. Hayano, M.J. Jenkins, L.V. Jørgensen, P. Ko, N. Madsen, P. Nolan, R.D. Page, L.G.C. Posada, A. Povilus, E. Sarid, D.M. Silveira, D.P. van der Werf, Y. Yamazaki, B. Parker, J. Escallier, and A. Ghosh. A magnetic trap for antihydrogen confinement. *Nucl. Inst. Meth. A*, **566**:746, (2006). [cited at p. v, 30, 31, 34, 35]
- [8] M. Amoretti, C. Amsler, G. Bazzano, G. Bonomi, A. Bouchta, P. Bowe, C. Carraro, C. L. Cesar, M. Charlton, M. Doser, V. Filippini, A. Fontana, M. C. Fujiwara, R. Funakoshi, P. Genova, J. S. Hangst, R. S. Hayano, L. V. Jørgensen, V. Lagomarsino, R. Landua, D. Lindelöf, E. Lodi Rizzini, M. Macri, N. Madsen, G. Manuzio, M. Marchesotti, P. Montagna, H. Pruys, C. Regenfus, P. Riedler, A. Rotondi, G. Rouleau, G. Testera, A. Variola, and D. P. van der Werf. High rate production of antihydrogen. *Phys. Lett. B*, **578**:23, (2004). [cited at p. viii, 7, 76, 77, 78]
- [9] G. B. Andresen, W. Bertsche, A. Boston, P. D. Bowe, C. L. Cesar, S. Chapman, M. Charlton, M. Chartier, A. Deutsch, J. Fajans, M. C. Fujiwara, R. Funakoshi, D. R.

Gill, K. Gomberoff, J. S. Hangst, R. S. Hayano, R. Hydomako, M. J. Jenkins, L. V. Jørgensen, L. Kurchaninov, N. Madsen, P. Nolan, K. Olchanski, A. Olin, R. D. Page, A. Povilus, F. Robicheaux, E. Sarid, D. M. Silveira, J. W. Storey, R. I. Thompson, D. P. van der Werf, J. S. Wurtele, and Y. Yamazaki. Production of antihydrogen at reduced magnetic field for anti-atom trapping. *J. Phys. B*, **41**:011001, (2008). [cited at p. viii, ix, 79, 80]

[10] G. B. Andresen, W. Bertsche, P. D. Bowe, C. C. Bray, E. Butler, C. L. Cesar, S. Chapman, M. Charlton, J. Fajans, M. C. Fujiwara, R. Funakoshi, D. R. Gill, J. S. Hangst, W. N. Hardy, R. S. Hayano, M. E. Hayden, A. J. Humphries, R. Hydomako, M. J. Jenkins, L. V. Jørgensen, L. Kurchaninov, R. Lambo, N. Madsen, P. Nolan, K. Olchanski, A. Olin, R. D. Page, A. Povilus, P. Pusa, F. Robicheaux, E. Sarid, S. Seif El Nasr, D. M. Silveira, J. W. Storey, R. I. Thompson, D. P. van der Werf, J. S. Wurtele, and Y. Yamazaki. A novel antiproton radial diagnostic based on octupole induced ballistic loss. *Phys. Plasmas*, **15**:032107, (2008). [cited at p. ix, 83, 93]

[11] G. Andresen, W. Bertsche, A. Boston, P. D. Bowe, C. L. Cesar, S. Chapman, M. Charlton, M. Chartier, A. Deutsch, J. Fajans, M. C. Fujiwara, R. Funakoshi, D. R. Gill, K. Gomberoff, J. S. Hangst, R. S. Hayano, R. Hydomako, M. J. Jenkins, L. V. Jørgensen, L. Kurchaninov, N. Madsen, P. Nolan, K. Olchanski, A. Olin, A. Povilus, F. Robicheaux, E. Sarid, D. M. Silveira, J. W. Storey, H. H. Telle, R. I. Thompson, D. P. van der Werf, J. S. Wurtele, and Y. Yamazaki. Antimatter Plasmas in a Multipole Trap for Antihydrogen. *Phys. Rev. Lett.*, **98**:023402, (2007). [cited at p. ix, 85, 86]

[12] G. B. Andresen, W. Bertsche, P. D. Bowe, C. C. Bray, E. Butler, C. L. Cesar, S. Chapman, M. Charlton, J. Fajans, M. C. Fujiwara, R. Funakoshi, D. R. Gill, J. S. Hangst, W. N. Hardy, R. S. Hayano, M. E. Hayden, R. Hydomako, M. J. Jenkins, L. V. Jørgensen, L. Kurchaninov, R. Lambo, N. Madsen, P. Nolan, K. Olchanski, A. Olin, A. Povilus, P. Pusa, F. Robicheaux, E. Sarid, S. Seif El Nasr, D. M. Silveira, J. W. Storey, R. I. Thompson, D. P. van der Werf, J. S. Wurtele, and Y. Yamazaki. Compression of Antiproton Clouds for Antihydrogen Trapping. *Phys. Rev. Lett.*, **100**:203401, (2008). [cited at p. x, 96, 97]

[13] A. Einstein. Über einen die Erzeugung und Verwandlung des Lichtes betreffenden heuristischen Gesichtspunkt. - On a Heuristic Viewpoint Concerning the Production and Transformation of Light. (1905). [cited at p. 1]

[14] A. Einstein. Zur Elektrodynamik bewegter Körper. - On the Electrodynamics of Moving Bodies. *Annalen der Physik*, **17**:891, (1905). [cited at p. 1]

[15] P. A. M. Dirac. The Quantum Theory of the Electron. *Proceedings of the Royal Society of London. Series A*, **117**:610, (1928). [cited at p. 1]

[16] P. A. M. Dirac. The Quantum Theory of the Electron. Part II. *Proceedings of the Royal Society of London. Series A*, **118**:351, (1928). [cited at p. 1]

[17] P. A. M. Dirac. A Theory of Electrons and Protons. *Proceedings of the Royal Society of London. Series A*, **126**:360, (1930). [cited at p. 2]

[18] J. R. Oppenheimer. On the Theory of Electrons and Protons. *Phys. Rev.*, **35**:562, (1930). [cited at p. 2]

- [19] O. Chamberlain, E. Segrè, C. Wiegand and T. Ypsilantis. Observation of Antiprotons. *Phys. Rev.*, **100**:947, (1955). [cited at p. 3]
- [20] B. Cork, G. R. Lambertson, O. Piccioni and W. A. Wenzel. Antineutrons Produced from Antiprotons in Charge-Exchange Collisions. *Phys. Rev.*, **104**:1193, (1956). [cited at p. 3]
- [21] G. Blanford, D. C. Christian, K. Gollwitzer, M. Mandelkern, C. T. Munger, J. Schultz, and G. Zioulas. Observation of Atomic Antihydrogen. *Phys. Rev. Lett.*, **80**:3037, (1998). [cited at p. 4]
- [22] G. Gabrielse, N. S. Bowden, P. Oxley, A. Speck, C. H. Storry, J. N. Tan, M. Wessels, D. Grzonka, W. Oelert, G. Schepers, T. Sefzick, J. Walz, H. Pittner, T. W. Hänsch, and E. A. Hessels. Background-Free Observation of Cold Antihydrogen with Field-Ionization Analysis of its States. *Phys. Rev. Lett.*, **89**:213401, (2002). [cited at p. 5]
- [23] G. Gabrielse, N. S. Bowden, P. Oxley, A. Speck, C. H. Storry, J. N. Tan, M. Wessels, D. Grzonka, W. Oelert, G. Schepers, T. Sefzick, J. Walz, H. Pittner, T. W. Hänsch, and E. A. Hessels. Driven Production of Cold Antihydrogen and the First Measured Distribution of Antihydrogen States. *Phys. Rev. Lett.*, **89**:233401, (2002). [cited at p. 5]
- [24] M. Amoretti, C. Amsler, G. Bonomi, P. D. Bowe, C. Canali, C. Carraro, C. L. Cesar, M. Charlton, A. M. Ejsing, A. Fontana, M. C. Fujiwara, R. Funakoshi, P. Genova, J. S. Hangst, R. S. Hayano, L. V. Jørgensen, A. Kellerbauer, V. Lagomarsino, E. Lodi Rizzini, M. Macri, N. Madsen, G. Manuzio, D. Mitchard, P. Montagna, L. G. C. Posada, H. Pruys, C. Regenfus, A. Rotondi, H. H. Telle, G. Testera, D. P. Van der Werf, A. Variola, L. Venturelli, Y. Yamazaki, and N. Zurlo. Search for Laser-Induced Formation of Antihydrogen Atoms. *Phys. Rev. Lett.*, **97**:213401, (2006). [cited at p. 7]
- [25] M. Amoretti, C. Amsler, G. Bonomi, A. Bouchta, P. D. Bowe, C. Carraro, C. L. Cesar, M. Charlton, M. Doser, V. Filippini, A. Fontana, M. C. Fujiwara, R. Funakoshi, P. Genova, J. S. Hangst, R. S. Hayano, L. V. Jørgensen, A. Kellerbauer, V. Lagomarsino, R. Landua, D. Lindelof, E. Lodi Rizzini, M. Macri, N. Madsen, G. Manuzio, P. Montagna, H. Pruys, C. Regenfus, A. Rotondi, G. Testera, A. Variola, L. Venturelli, D. P. van der Werf, and Y. Yamazaki. Dynamics of antiproton cooling in a positron plasma during antihydrogen formation. *Phys. Lett. B*, **590**:133, (2004). [cited at p. 7, 76, 77]
- [26] N. Madsen, M. Amoretti, C. Amsler, G. Bonomi, P. D. Bowe, C. Carraro, C. L. Cesar, M. Charlton, M. Doser, A. Fontana, M. C. Fujiwara, R. Funakoshi, P. Genova, J. S. Hangst, R. S. Hayano, L. V. Jørgensen, A. Kellerbauer, V. Lagomarsino, R. Landua, E. Lodi-Rizzini, M. Macri, D. Mitchard, P. Montagna, H. Pruys, C. Regenfus, A. Rotondi, G. Testera, A. Variola, L. Venturelli, D. P. van der Werf, Y. Yamazaki, and N. Zurlo. Spatial Distribution of Cold Antihydrogen Formation. *Phys. Rev. Lett.*, **94**:033403, (2005). [cited at p. 7]
- [27] M. Amoretti, C. Amsler, G. Bazzano, G. Bonomi, A. Bouchta, P. D. Bowe, C. Canali, C. Carraro, C. L. Cesar, M. Charlton, M. Doser, A. Fontana, M. C. Fujiwara, R. Funakoshi, P. Genova, J. S. Hangst, R. S. Hayano, I. Johnson, L. V. Jørgensen, A. Kellerbauer, V. Lagomarsino, R. Landua, E. Lodi Rizzini, M. Macri, N. Madsen, G. Manuzio, M. Marchesotti, D. Mitchard, F. Ottone, H. Pruys, C. Regenfus, P. Riedler, A. Rotondi, G. Testera, A. Variola, L. Venturelli, Y. Yamazaki, D. P. van der Werf, and

N. Zurlo. Antihydrogen Production Temperature Dependence. *Phys. Lett. B*, **583**:59, (2004). [cited at p. 7, 76]

[28] T. D. Lee and C. N. Yang. Question of Parity Conservation in Weak Interactions. *Phys. Rev.*, **104**:254, (1956). [cited at p. 8]

[29] C. S. Wu, E. Ambler, R. W. Hayward, D. D. Hoppes, and R. P. Hudson. Experimental Test of Parity Conservation in Beta Decay. *Phys. Rev.*, **105**:1413, (1957). [cited at p. 8]

[30] J. H. Christenson, J. W. Cronin, V. L. Fitch, and R. Turlay. Evidence for the  $2\pi$  decay of the  $K_2^0$  meson. *Phys. Rev. Lett.*, **13**:138, (1964). [cited at p. 8]

[31] G. Gabrielse, A. Khabbaz, D. S. Hall, C. Heimann, H. Kalinowsky, and W. Jhe. Precision Mass Spectroscopy of the Antiproton and Proton Using Simultaneously Trapped Particles. *Phys. Rev. Lett.*, **82**:3198, (1999). [cited at p. 8]

[32] R. Carosi, P. Clarke, D. Coward, D. Cundy, N. Doble, L. Gatignon, V. Gibson, P. Grafstrom, R. Hagelberg, G. Kesseler, J. van der Lans, H. N. Nelson, H. Wahl, R. Black, D. J. Candelier, J. Muir, K. J. Peach, H. Blmer, R. Heinz, M. Kasemann, K. Kleinknecht, P. Mayer, B. Panzer, B. Renk, S. Roehn, H. Rohrer, E. Aug, R. L. Chase, D. Fournier, P. Heusse, L. Iconomidou-Fayard, I. Harrus, A. M. Lutz, A. C. Schaffer, L. Bertanza, A. Bigi, P. Calafiura, M. Calvetti, R. Casali, C. Cerri, R. Fantechi, G. Gargani, I. Manzelli, A. Nappi, G. M. Pierazzini, C. Becker, H. Burkhardt, M. Holder, G. Quast, M. Rost, H. G. Sander, W. Weihs, and G. Zech. A measurement of the phases of the CP-violating amplitudes in  $K^0 \rightarrow 2\pi$  decays and a test of CPT invariance. *Phys. Lett. B*, **237**:303, (1990). [cited at p. 9]

[33] M. Niering, R. Holzwarth, J. Reichert, P. Pokasov, Th. Udem, M. Weitz, T. W. Hänsch, P. Lemonde, G. Santarelli, M. Abgrall, P. Laurent, C. Salomon, and A. Clairon. Measurement of the Hydrogen 1S-2S Transition Frequency by Phase Coherent Comparison with a Microwave Cesium Fountain Clock. *Phys. Rev. Lett.*, **84**:5496, (2000). [cited at p. 9]

[34] C. L. Cesar, D. G. Fried, T. C. Killian, A. D. Polcyn, J. C. Sandberg, I. A. Yu, T. J. Greytak, D. Kleppner, and J. M. Doyle. Two-Photon Spectroscopy of Trapped Atomic Hydrogen. *Phys. Rev. Lett.*, **77**:255, (1996). [cited at p. 9]

[35] R. Bluhm, V. A. Kostelecký, and N. Russell. CPT and Lorentz Tests in Hydrogen and Antihydrogen. *Phys. Rev. Lett.*, **82**:2254, (1999). [cited at p. 9]

[36] D. F. Phillips, M. A. Humphrey, E. M. Mattison, R. E. Stoner, R. F. C. Vessot, and R. L. Walsworth. Limit on Lorentz and CPT violation of the proton using a hydrogen maser. *Phys. Rev. D*, **63**:111101, (2001). [cited at p. 9]

[37] R. S. Hayano. Ground-state hyperfine splitting of antihydrogen. *Hyperfine Interactions*, **172**:53, (2006). [cited at p. 9]

[38] A. Coc, R. Le Gac, M. de Saint-Simon, C. Thibault, F. Touchard, E. Haebel, H. Herr, R. Klapisch, G. Lebee, G. Petrucci, G. Stefani, A. Schempp, H. Deitinghoff, and F. Botlo-Pilat. In *Low Energy Antiproton Physics*. LEAP'90, 431. World Scientific, Singapore, (1991). [cited at p. 9]

[39] G. Gabrielse, X. Fei, K. Helmerson, S. L. Rolston, R. Tjoelker, T. A. Trainor, H. Kalinowsky, J. Haas, and W. Kells. First Capture of Antiprotons in a Penning Trap: A Kiloelectronvolt Source. *Phys. Rev. Lett.*, **57**:2504, (1986). [cited at p. 9]

[40] G. Gabrielse, X. Fei, L. A. Orozco, R. L. Tjoelker, J. Haas, H. Kalinowsky, T. A. Trainor, and W. Kells. Cooling and slowing of trapped antiprotons below 100 meV. *Phys. Rev. Lett.*, **63**:1360, (1989). [cited at p. 9]

[41] X. Feng, M. H. Holzscheiter, R. A. Lewis, R. Newton, and M. M. Schauer. Extraction of ultra-low energy antiprotons from Penning traps. *Hyperfine Interactions*, **100**:103, (1996). [cited at p. 9]

[42] M. H. Holzscheiter, X. Feng, T. Goldman, N. S. P. King, R. A. Lewis, M. M. Nieto, and G. A. Smith. Are antiprotons forever? *Phys. Lett. A*, **214**:279, (1996). [cited at p. 9]

[43] M. Hori, J. Eades, R. S. Hayano, T. Ishikawa, W. Pirkl, E. Widmann, H. Yamaguchi, H. A. Torii, B. Juhász, D. Horváth, and T. Yamazaki. Direct Measurement of Transition Frequencies in Isolated  $\bar{p}$  He<sup>+</sup> Atoms, and New CPT-Violation Limits on the Antiproton Charge and Mass. *Phys. Rev. Lett.*, **91**:123401, (2003). [cited at p. 12]

[44] M. Hori, A. Dax, J. Eades, K. Gomikawa, R. S. Hayano, N. Ono, W. Pirkl, E. Widmann, H. A. Torii, B. Juhász, D. Barna, and D. Horvath. Determination of the Antiproton-to-Electron Mass Ratio by Precision Laser Spectroscopy of  $\bar{p}$  He<sup>+</sup>. *Phys. Rev. Lett.*, **96**:243401, (2006). [cited at p. 12]

[45] T. J. Murphy and C. M. Surko. Positron trapping in an electrostatic well by inelastic collisions with nitrogen molecules. *Phys. Rev. A*, **46**:5696, (1992). [cited at p. 12]

[46] R. G. Greaves, M. D. Tinkle, and C. M. Surko. Creation and uses of positron plasmas. *Phys. Plasmas*, **1**:1439, (1994). [cited at p. 12]

[47] R. Khatri, M. Charlton, P. Sferlazzo, K. G. Lynn, A. P. Mills Jr., and L. O. Roellig. Improvement of rare-gas solid moderators by using conical geometry. *Appl. Phys. Lett.*, **57**:2374, (1990). [cited at p. 14]

[48] L. Madansky and F. Rasetti. An Attempt to Detect Thermal Energy Positrons. *Phys. Rev.*, **79**:397, (1950). [cited at p. 14]

[49] W. Cherry. *Secondary Electron Emission Produced from Surface by Positron Bombardment*. PhD thesis, Princeton University, (1958). [cited at p. 14]

[50] A. P. Mills Jr. and E. M. Gullikson. Solid neon moderator for producing slow positrons. *Appl. Phys. Lett.*, **49**:1121, (1986). [cited at p. 14]

[51] J. P. Merrison, M. Charlton, B. I. Deutch, and L. V. Jørgensen. Field assisted positron moderation by surface charging of rare gas solids. *J. Phys.: Condensed Matter*, **4**:L207, (1992). [cited at p. 14]

[52] L. V. Jørgensen, J. P. Merrison, B. I. Deutch, M. Charlton, and G. O. Jones. Positron dynamics in surface-charged solid argon. *Phys. Rev. B*, **52**:12402, (1995). [cited at p. 14]

[53] C. M. Surko, A. Passner, M. Leventhal, and F. J. Wysocki. Bound states of positrons and large molecules. *Phys. Rev. Lett.*, **61**:1831, (1988). [cited at p. 15]

[54] K. Iwata, R. G. Greaves, T. J. Murphy, M. D. Tinkle, and C. M. Surko. Measurements of positron-annihilation rates on molecules. *Phys. Rev. A*, **51**:473, (1995). [cited at p. 15]

[55] W.M. Itano and D.J. Wineland. Laser cooling of ions stored in harmonic and Penning traps. *Phys. Rev. A*, **25**:35, 1982. [cited at p. 16]

- [56] X.-P. Huang, F. Anderegg, E. M. Hollmann, C. F. Driscoll, and T. M. O'Neil. Steady-State Confinement of Non-neutral Plasmas by Rotating Electric Fields. *Phys. Rev. Lett.*, **78**:875, (1997). [cited at p. 19]
- [57] R. G. Greaves and C. M. Surko. Inward Transport and Compression of a Positron Plasma by a Rotating Electric Field. *Phys. Rev. Lett.*, **85**:1883–1886, (2000). [cited at p. 19]
- [58] R. G. Greaves and C. M. Surko. Radial compression and inward transport of positron plasmas using a rotating electric field. *Phys. Plasmas*, **8**:1879, (2001). [cited at p. 19]
- [59] J. Stevefelt, J. Boulmer, and J F. Delpach. Collisional-radiative recombination in cold plasmas. *Phys. Rev. A*, **12**:1246, (1975). [cited at p. 26]
- [60] A. Müller and A. Wolf. Production of antihydrogen by recombination of  $\bar{p}$  with  $e^+$ : What can we learn from electron–ion collision studies? *Hyperfine Interactions*, **109**:233, (1997). [cited at p. 26]
- [61] P. Mansbach and J. Keck. Monte Carlo Trajectory Calculations of Atomic Excitation and Ionization by Thermal Electrons. *Phys. Rev.*, **181**:275–289, (1969). [cited at p. 26]
- [62] Michael E. Glinsky and Thomas M. O'Neil. Guiding center atoms: Three-body recombination in a strongly magnetized plasma. *Phys. Fluids B*, **3**:1279, (1991). [cited at p. 26]
- [63] Y.V. Gott, M.S. Ioffe, and V.G. Tel'kovskii. *Nucl. Fusion*, Pt. **3**:1045, (1962). [cited at p. 28]
- [64] D. E. Pritchard. Cooling Neutral Atoms in a Magnetic Trap for Precision Spectroscopy. *Phys. Rev. Lett.*, **51**:1336, (1983). [cited at p. 28]
- [65] T. M. O'Neil. A confinement theorem for nonneutral plasmas. *Phys. Fluids*, **23**:2216, (1980). [cited at p. 29]
- [66] T. M. Squires, P. Yesley, and G. Gabrielse. Stability of a Charged Particle in a Combined Penning-Ioffe Trap. *Phys. Rev. Lett.*, **86**:5266, (2001). [cited at p. 29]
- [67] J. Fajans and A. Schmidt. Malmberg-Penning and Minimum-B trap compatibility: the advantages of higher-order multipole traps. *Nucl. Inst. Meth. A*, **521**:318, (2004). [cited at p. 29, 30]
- [68] J. Fajans, W. Bertsche, K. Burke, S. F. Chapman, and D. P. van der Werf. Effects of Extreme Magnetic Quadrupole Fields on Penning Traps and the Consequences for Antihydrogen Trapping. *Phys. Rev. Lett.*, **95**:155001, (2005). [cited at p. 29, 81]
- [69] <http://doc.cern.ch/archive/electronic/cern/preprints/spsc/public/spsc-2005-006.pdf>. [cited at p. 29]
- [70] <http://www.bnl.gov/magnets/bepcii/bepcii.asp>. [cited at p. 33]
- [71] M. H. Holzscheiter. Slowing down and trapping of MeV antiprotons. *Physica Scripta*, **46**:272, (1992). [cited at p. 40, 41]
- [72] National Instruments. <http://www.ni.com/labview/>. [cited at p. 45]
- [73] LEMO Connectors. <http://www.lemo.com/index.jsp>. [cited at p. 48]
- [74] <http://midas.phi.ch>, <http://midas.triumf.ca>. [cited at p. 54]

- [75] Paul Scherrer Institut. <http://www.psi.ch>. [cited at p. 54]
- [76] TRI University Meson Facility. <http://www.triumf.ca>. [cited at p. 54]
- [77] M. Moretti, G. Bonomi, A. Bouchta, P. D. Bowe, C. Carraro, C. L. Cesar, M. Charlton, M. Doser, A. Fontana, M. C. Fujiwara, R. Funakoshi, P. Genova, J. S. Hangst, R. S. Hayano, L. V. Jørgensen, V. Lagomarsino, R. Landua, E. Lodi Rizzini, M. Macrì, N. Madsen, G. Manuzio, G. Testera, A. Variola, and D. P. van der Werf. Complete nondestructive diagnostic of nonneutral plasmas based on the detection of electrostatic modes. *Phys. Plasmas*, **10**:3056, (2003). [cited at p. 60]
- [78] J. F. Ziegler. <http://www.srim.org>. SRIM-2003 Software. [cited at p. 65]
- [79] J. F. Ziegler. Stopping of energetic light ions in elemental matter. *J. Appl. Phys.*, **85**:1249, (1999). [cited at p. 65]
- [80] G. Gabrielse, J. Estrada, J.N. Tan, P. Yesley, N.S. Bowden, P. Oxley, T. Roach, C.H. Storry, M. Wessels, J. Tan, D. Grzonka, W. Oelert, G. Schepers, T. Sefzick, W.H. Breunlich, M. Cargnelli, H. Fuhrmann, R. King, R. Ursin, J. Zmeskal, H. Kalinowsky, C. Wesdorp, J. Walz, K.S.E. Eikema, and Hänsch T W. First positron cooling of antiprotons. *Phys. Lett. B*, **507**:1, (2001). [cited at p. 77]
- [81] J. Fajans, W. Bertsche, K. Burke, A. Deutscher, S. F. Chapman, K. Gomberoff, D. P. van der Werf, and J. S. Wurtele. Simple loss scaling laws for quadrupoles and higher-order multipoles used in antihydrogen traps. In *Non-Neutral Plasma Physics VI: Workshop on Non-Neutral Plasmas 2006*. **862**, 176. AIP, (2006). [cited at p. 81]
- [82] D. L. Eggleston and T. M. O'Neil. Theory of asymmetry-induced transport in a non-neutral plasma. *Phys. Plasmas*, **6**:2699, (1999). [cited at p. 81]
- [83] J. Fajans, N. Madsen, and F. Robicheaux. Critical loss radius in a Penning trap subject to multipole fields. *Phys. Plasmas*, **15**:032108, (2008). [cited at p. 82, 83]
- [84] F. Chen. *Introduction to Plasma Physics and Controlled Fusion*. Springer, (1984). [cited at p. 96]
- [85] BEHLKE Electronic GMBH. <http://www.behlke.de>. [cited at p. 109]
- [86] Ross Engineering Corp. <http://www.rossengineeringcorp.com>. [cited at p. 110]
- [87] Glassman High Voltage Inc. <http://www.glassmanhv.com>. [cited at p. 110]



# Appendices



## Appendix A

---

# The High Voltage System

---

In order to catch antiprotons, a high voltage must be applied to an electrode in an ultra high vacuum in a very short time. Wires and vacuum feedthroughs suitable for the ultra high vacuum conditions and limited space available in the ALPHA apparatus are somewhat restricted in scope. In order to keep costs down by using fairly widely available components, the decision was made to design the high voltage system to operate at 5 kV.

The velocity of an antiproton at a kinetic energy of 5 keV is around  $9.8 \times 10^5$  ms<sup>-1</sup>. The distance from the centre of electrode 1 (HVA) to the centre of electrode 9 (HVB) is 186 mm. This means that the time for antiprotons at 5 keV to enter the trap (pass the centre of HVA), be reflected from HVB and leave the trap again is around 380 ns. If the length of the antiproton bunch is 200 ns (assumed to be true although the actual bunch length is typically shorter) then in order to catch the entire bunch the high voltage must be able to switch on in 180 ns or less. Thus we aimed to build a system capable of switching in  $\sim 120$  ns.

Switches capable of safely applying 5 kV on a timescale of order 100 ns are not widely available. A high voltage MOSFET manufactured by BELKHE [85] was chosen. The exact choice of switch was driven by the need to safely handle the power requirements.

The power required to supply 5 kV in 120 ns depends on the capacitance of the system being charged. The choice of HV wire and vacuum feedthrough used in the ALPHA apparatus and the route chosen to connect the wires to outside the trap vacuum (i.e. the length of the wires) led to the system having a capacitance of around 1.1 nF.

The energy stored in a charged capacitor  $E$  is given by

$$E = \frac{CV^2}{2},$$

where  $C$  is the capacitance and  $V$  is the total charge (voltage). The peak power in charging a capacitance is then given by

$$P_{\text{peak}} = \frac{E}{t},$$

where  $t$  is the time taken to apply the energy  $E$ . Peak current is given by

$$I_{\text{peak}} = \frac{P_{\text{peak}}}{V}.$$

For the ALPHA apparatus,  $P_{\text{peak}} = 1.042 \times 10^5$  W, and  $I_{\text{peak}} = 20.83$  A.

To meet these power requirements, as well as the requirement to be able to operate above 5 kV the switch chosen was the BELKHE HTS 161-03-LC. This switch can operate up to 16 kV and at a peak instantaneous current of 30 A. This was considered to give some room for higher voltages in future iterations of the apparatus.

As well as fast switching of high voltage, it was also necessary for the high voltage system to be able to switch to lower voltage supplies for operations that required fine control of electrode potentials (for example antiproton transfer). This was achieved using reed relays manufactured by Ross engineering [86]. The relays were rated to 15 kV and were operated by applying 6 V, at approximately 170 mA, across a switching coil. Due to the magnetic nature of the relay switching, and the fact that they were necessarily placed fairly close to the main solenoid so that the high voltage cable lengths could be kept as short as possible, the relays and their associated driver circuits were surrounded by several layers of mu-metal shielding. Mu-metal is a nickel-iron alloy that has a very high magnetic permeability, making it very effective at screening static magnetic fields.

The high voltage was provided by two MK60P1.2 supplies manufactured by Glassman High Voltage [87]. These supplies were rated to 60 kV at 1.2 mA, however they were limited at the supply to a maximum of 10 kV. The 1.2 mA current limit of the supply is clearly not compatible with the 20.8 A required during the fast switching of HVA. However, the supplies were the same ones as had been used for the fast high voltage switching in the ATHENA apparatus and were thus presumed to be suitable for the ALPHA apparatus. Testing of the high voltage system demonstrated that the supplies were in fact capable of supplying the required voltage, albeit with one unusual feature. Observation of the rising edge of the high voltage pulse, demonstrated that only around 80% of the set voltage would be applied fast (of order 100 ns), the rest would be applied considerably more slowly (of order 50 ms), and with

large voltage transients. Figure A.1 shows oscilloscope traces illustrating this. Discussion with the manufacturer suggested that the speed of the demand was temporarily circumventing the built-in over-current protection such that the supply would keep up with the demand until this protection engaged. They did not consider this likely to be damaging to the supply, so the supplies were deemed suitable for ALPHA. In order to catch 5 kV antiprotons the fast supply was operated at approximately 6.4 kV. This resulted in 5 kV being applied to the electrode in approximately 125 ns. On opening the BEHLKE switch (in the case of HVA) or switching off the Glassman supply (in the case of HVB), the electrodes would discharge through a  $20\text{ M}\Omega$  high-voltage resistor in approximately half a second (shown in figure A.2).

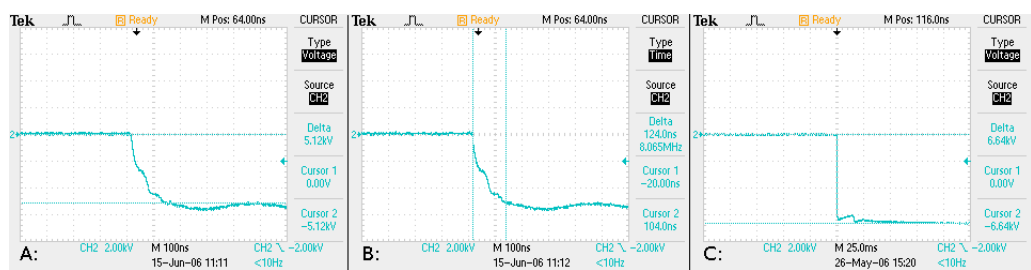


Figure A.1: Oscilloscope traces illustrating the charging characteristics during the fast high voltage switching. Figures A: and B: are taken from the same data acquisition cycle and show the initial fast voltage drop (5.12 kV in 124 ns). Figure C: is taken from a different data acquisition cycle (before several stages of optimisation), but illustrates the voltage transients typical during the approximately 50 ms after the initial drop (discussed in the text).



Figure A.2: Oscilloscope trace showing the discharging of HVB. This trace was taken during the 2007 beam time, but using an identical system to that used in 2006.

Control of the high voltage system was achieved through a custom LabVIEW program hosted on the electron gun control PC as described in section 2.5.6. A digital output channel from the sequencer would be set high to initiate high voltage mode. The control program monitored this line (via a digital IO board), and would send control signals (via the same IO board) to the high

voltage system that would safely switch between high voltage and low voltage modes (ensuring the high voltage supplies were off before switching the relays). In the case of HVB, the high voltage would be applied to the electrode once the control program enabled the power supply. For HVA, the control program would switch to high voltage mode and enable the power supply such that the supply to the electrode was then only interrupted by the open BEHLKE switch. The fast switching was then accomplished via a system of NIM\*logic and delay modules as shown in figure A.3. The control program would arm the coincidence module. A signal sent from the AD control system at a pre-set time before the antiproton ejection occurs (known as the AD pre-trigger) would then trigger the coincidence module. This signal had a time jitter of around 12 ns and was also used to trigger the detector systems, so first passed through a linear fan-out and a discriminator module. The coincidence then activated a gate module via a variable delay module. The variable delay was used to adjust the timing of the HV activation in order to optimise antiproton catching (as discussed in section 3.2.2). The gate module then sent the signal which closed the BEHLKE switch thus supplying high voltage to HVA. Once the HV ON line from the sequencer went low (to signify that high voltage was to be switched off) the control program would disarm the coincidence, and deactivate the gate module, thus opening the BEHLKE switch and interrupting the supply to the electrode. The control program would then safely switch the system over to low voltage operation.

---

\*Nuclear Instrumentation Module. A system of electronics modules with standardised mechanical and electrical specifications. The modules are interchangeable within a larger chassis (known as a NIM bin or NIM crate).

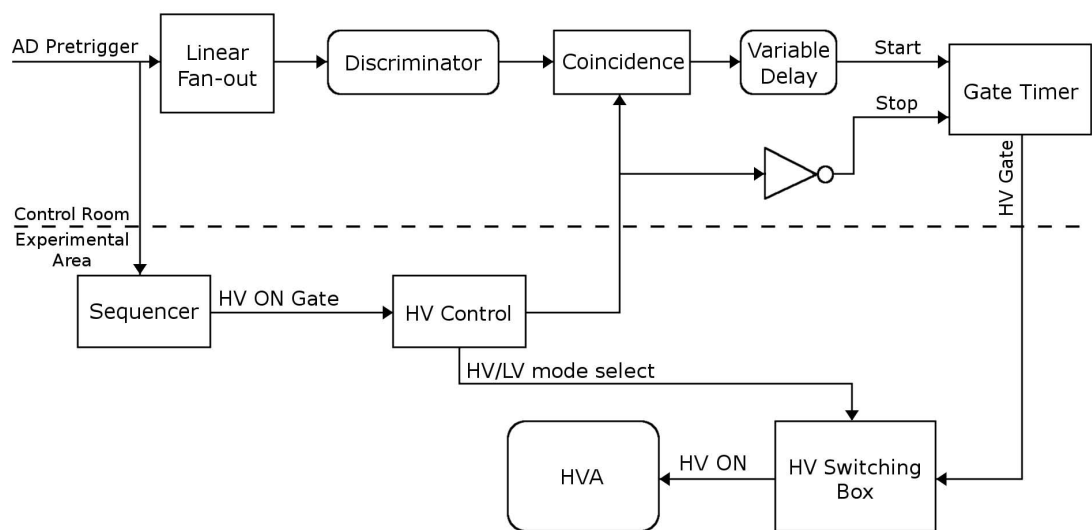


Figure A.3: Schematic representation of the control and timing system for the fast high voltage switching. See text for details.

